

CHALMERS



Investigation and Evaluation of the Volvo Aero Tool Volvane for Outlet Guide Vane Design

Master's Thesis in Applied Mechanics

JULIA ANTONIADES SKOOG

Department of Applied Mechanics
Division of Fluid Dynamics
CHALMERS UNIVERSITY OF TECHNOLOGY
Gothenburg, Sweden 2012
Master's Thesis 2012:18

MASTER'S THESIS IN APPLIED MECHANICS

Investigation and Evaluation of the Volvo Aero Tool Volvane for Outlet
Guide Vane Design

JULIA ANTONIADES SKOOG

Department of Applied Mechanics
Division of Fluid Dynamics
CHALMERS UNIVERSITY OF TECHNOLOGY
Gothenburg, Sweden 2012

Investigation and Evaluation of the Volvo Aero Tool Volvane for Outlet Guide Vane Design
JULIA ANTONIADES SKOOG

© JULIA ANTONIADES SKOOG, 2012

Master's Thesis 2012:18
ISSN 1652-8557
Department of Applied Mechanics
Division of Fluid Dynamics
Chalmers University of Technology
SE-412 96 Gothenburg
Sweden
Telephone: +46 (0)31-772 1000

Cover:

A characteristic jet engine[Cor10]. The outlet guide vanes are located in the aft part of the engine. Please see section 1 for further details.

Chalmers Reproservice
Gothenburg, Sweden 2012

Investigation and Evaluation of the Volvo Aero Tool *Volvane* for Outlet Guide Vane Design
Master's Thesis in Applied Mechanics
JULIA ANTONIADES SKOOG
Department of Applied Mechanics
Division of Fluid Dynamics
Chalmers University of Technology

ABSTRACT

One of the main functions of the turbine rear frame, located in the aft part of the engine, is to remove the angular component of the outgoing flow from the low pressure turbine. The angular component in the outgoing flow is due to load on the low pressure turbine. The most interesting part of the turbine rear frame from an aerodynamic point of view is the gas channel consisting of outlet guide vanes, a hub, and a shroud. *Volvane* is a powerful in-house design tool used to create guide vanes and includes a *2D panel* which is a potential flow solver and a *G3D Euler* solver. Minimizing the number of design parameters is a main issue and may result in a significant improvement in the outlet guide vane design process with *Volvane*. Initially a reference design of an outlet guide vane is created in *Volvane*. The design is simulated in *Volvane* and with different RANS-solvers and computational grids. After analysis of the flow results, a RANS-solver is selected for further use in the investigation. In Part 1, the design tool validation is the target to reduce the number of design parameters. Three different design of experiments (DoEs) are created. Design parameters and boundary conditions were varied to investigate how the flow behaves around the outlet guide vanes for different geometries and operating conditions. The same changes were simulated in RANS-solvers and the results compared with those of the *Volvane* program. Analysis in Part 1 resulted in updates of new *Volvane* versions. The *Volvane G3D Euler* solver has more difficulties in predicting changes in lean compared to changes in sweep and is more able to predict an increased than a decreased sweep angle. If the boundary condition of the swirl is increased, the *Volvane G3D Euler* solver has difficulties in predicting the diffusion factor. Simulations with wall function mesh in the selected RANS-solver showed a 2% outlet swirl angle difference from the low Reynolds mesh. This aspect should be taken into account when analyzing results from flow simulations. The loss estimations from the *Volvane G3D Euler* solver are approximately 35% of the loss estimations from the RANS-solver. Generally the *Volvane G3D Euler* solver and the RANS-solver are in good agreement.

In Part 2, the design process rationalization, response surface methodology (RSM) is created to find correlations between design and output parameters. A statistical software is the main tool used. The correlations measure the relations between different design and output parameters. Two additional DoEs are constructed. The analysis suggests the maximum thickness location of the vane can be shifted without affecting the axial position of maximum velocity. The correlations are unaffected when the parameter bounds are increased.

Keywords: Outlet Guide Vanes, *Volvane*, Computational Fluid Dynamics, Design of Experiments, Response Surface Methodology, Design tool validation, Design process rationalization.

ACKNOWLEDGEMENTS

First of all I would like to express my sincere gratitude to my supervisors Martin Nilsson and Fredrik Wallin at Volvo Aero Corporation and professor Lars-Erik Eriksson at Chalmers University of Technology. Thank you for all the help and support through this thesis work. Niklas Andersson, Mattias Billson and Anant Patwari thank you for all the help with the softwares. I would also like to thank all the colleagues and other master's thesis students at the Volvo Aero Corporation.

NOMENCLATURE

Latin letters

- a [m/s] Speed of sound
- C_p [-] Static pressure coefficient, definition in 3.3
- DF [-] Diffusion factor, definition in 3.3
- D [N] Drag force
- e [-] Specific internal energy
- F [N] Aerodynamic force
- h_0 [J] Specific total enthalpy
- L [m] Traveled length of fluid
- LF [N] Lift force
- Ma [-] Mach number, definition in 3.3
- P [Pa] Mean static pressure
- P_0 [Pa] Total pressure
- P_s [Pa] Static pressure
- Pr [-] Prandtl number, definition in 3.3
- q_j [-] Fourier's heat flux vector
- q_j^t [-] Turbulent heat flux vector
- q_{Lj} [-] Laminar heat flux vector
- Re [-] Reynolds number, definition in 3.3
- R [J/mol K] Molar gas constant
- s_{ij} [-] Instantaneous strain-rate tensor
- S_{ij} [-] Mean strain-rate tensor
- T [K] Temperature
- T_0 [Pa] Total temperature
- t [s] Time
- t_{ij} [s] Instantaneous viscous stress tensor
- U [-] Internal energy
- u_i [m/s] Instantaneous velocity in tensor notation
- u_j [m/s] Instantaneous velocity in tensor notation
- u'_{ij} [m/s] Fluctuating velocity in tensor notation
- u''_{ij} [m/s] Favre fluctuating velocity in tensor notation
- \tilde{u}_{ij} [m/s] Favre-averaged velocity in tensor notation
- u_*^2 [m²/s²] Friction velocity

u [m/s] Velocity in x-direction

v [m/s] Velocity in y-direction

w [m/s] Velocity in z-direction

V [m/s] Fluid flow velocity

y^+ [-] Defines the position in the near-wall layer

Greek letters

α [m^2/s] Thermal diffusion

δ_{ij} [-] Kronecker delta in tensor notation

ϵ [m^2/s^3] Turbulent dissipation rate

ζ [-] Second viscosity coefficient

η [m] Kolmogorov length scale

Θ [°] Total angle

κ [-] Thermal conductivity

μ [$kg/(m \cdot s)$] Molecular viscosity

μ_T [$kg/(m \cdot s)$] Turbulent viscosity

ν [m^2/s] Viscosity

ρ [kg/m^3] Density

τ [Pa] Shear Stress

τ_{ij} [Pa] Reynolds stress tensor

ϕ [-] Velocity potential

φ [-] Stream function

DEFINITIONS

Static pressure coefficient

$$C_p = \frac{P_s - P_{sref}}{P_{0ref} - P_{sref}} \quad (0.0.1)$$

Loss coefficient

$$\frac{P_{0in} - P_{0out}}{P_{0in} - P_{sin}} \quad (0.0.2)$$

Diffusion factor

$$DF = \frac{V_{max} - V_{out}}{V_{max}} \quad (0.0.3)$$

Mach number

$$Ma = \frac{V}{a} \quad (0.0.4)$$

Prandtl number

$$Pr = \frac{\nu}{\alpha} \quad (0.0.5)$$

Reynolds number

$$Re = \frac{\rho V L}{\mu} = \frac{\rho L}{\nu} \quad (0.0.6)$$

Maximum velocity

$$V_{max} \quad (0.0.7)$$

Axial position of maximum velocity

$$XV_{max} \quad (0.0.8)$$

ABBREVIATIONS

APG	<i>Adverse Pressure Gradient</i>
CCD	<i>Central Composite Design</i>
CDF	<i>Cumulative Distribution Function</i>
CFD	<i>Computational Fluid Dynamics</i>
DoE	<i>Design Of Experiments</i>
FCCD	<i>Face Centered Composite Design</i>
LE	<i>Leading Edge</i>
LPT	<i>Low Pressure Turbine</i>
NACA	<i>National Advisory Committee for Aeronautics</i>
OGV	<i>Outlet Guide Vane</i>
PDF	<i>Probability Density Function</i>
RANS	<i>Reynolds Average Navier Stokes</i>
RSM	<i>Response Surface Methodology</i>
TE	<i>Trailing Edge</i>
Tmax	<i>Maximum Thickness</i>
TRF	<i>Turbine Rear Frame</i>
VAC	<i>Volvo Aero Corporation</i>

CONTENTS

Abstract	i
Acknowledgements	i
Nomenclature	iii
Definitions	v
Abbreviations	vi
Contents	vii
1 Introduction	1
1.1 Jet engines	1
1.2 Turbine Rear Frame	1
1.3 Outlet guide vane aerodynamics	2
2 Objectives	4
3 Approach	5
4 Technical background	6
4.1 Design of Experiments	6
4.2 Response Surface Methodology	7
4.3 Potential flow solver	8
4.4 Inviscid flow solver	8
4.5 Viscous flow solver	9
4.6 Boundary layers	11
4.7 Turbulence modeling	12
5 Volvane - aerodesign tool for vanes and ducts	14
5.1 Volvane output parameters	17
6 Analysis tools	19
7 Reference design	20
7.1 Computational domains	21
7.2 Boundary conditions	22
7.3 Results for the reference design.	24
7.4 Summary & Conclusions for the Reference design.	31
8 Contents of the DoEs	32
9 Part 1. Design tool validation	32
9.1 DoE-A, lean and sweep	34
9.2 DoE-B, robustness regarding inlet conditions	37
9.3 DoE-C, camber line modifications	39
9.4 Part 1. Summary & Conclusions	42
10 Part 2. Design process rationalization	43
10.1 DoE-A	43
10.2 DoE-C	44
10.3 DoE-D	46
10.4 DoE-E	48
10.5 Part 2. Summary & Conclusions	50
11 Future work	51
12 Appendix A	52
12.1 Variance and standard deviation	52
12.2 Probability Density and Cumulative Distribution Functions	52
13 Appendix B, CDF charts DoE-A	55
14 Appendix C, CDF charts DoE-C	56
15 Appendix D, CDF charts DoE-D	56
16 Appendix E, CDF charts DoE-E	60

1 Introduction

1.1 Jet engines

The jet engine is essentially a gas-turbine and follow the Brayton cycle. A fan located in the front of the low-pressure compressor draws air into the engine. Part of the incoming airflow enters the low-pressure compressor and the remainder bypasses the core of the engine and flows through the fan. The high- and low-pressure compressors compresses the in-coming air and then the air enters the combustion chamber. In the combustion chamber the air is mixed with fuel and a combustion takes place. The combustion pressure level in a jet engine is approximately 20-40 bar (at sea level), compared with typical pressure levels of about 10-15 bar in stationary gas turbines [Eri10]. After leaving the combustion chamber the heated gas first enters a high pressure turbine and then a low pressure turbine, where a gas expansion occurs and a thrust is generated. The backward directed thrust forces the engine to move in a forward direction. The low pressure turbine also powers the fan through the low pressure shaft. The shaft is rotating and links the compressor with the turbine. In the jet engine there exist both high and low pressure shafts.

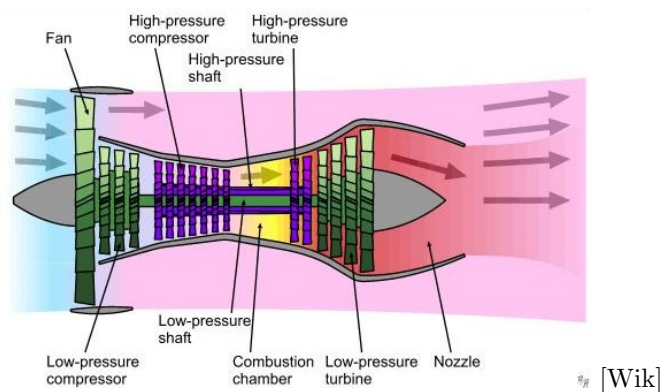
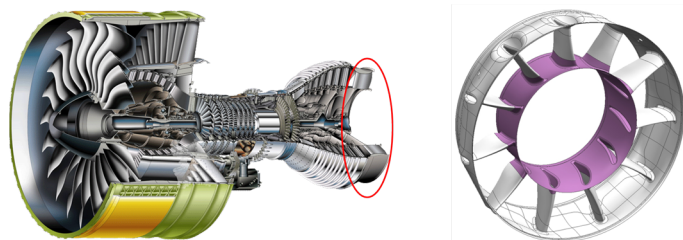


Figure 1.1: A schematic jet engine.

1.2 Turbine Rear Frame

The main functions of the turbine rear frame (TRF), located in the aft part of the engine, are to provide a structural support for the aircraft installation, to provide a support for the bearing that supports the low pressure shaft, and to remove the angular component of the outgoing flow from the low pressure turbine. The angular component is due to aerodynamic load on the low pressure turbine. The most interesting part of the turbine rear frame from an aerodynamic point of view is the gas channel consisting of outlet guide vanes, an inner wall (hub) and an outer wall (shroud).



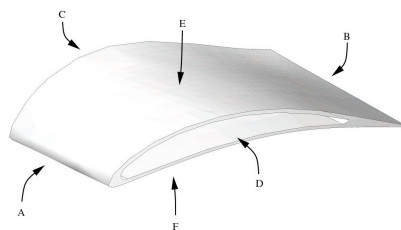
[Cor10]

Figure 1.2: A typical jet engine is shown at the left, the turbine rear frame is located in the aft part of the engine, indicated by the red circle. At the right, the gas channel section of the turbine rear frame is shown with the outlet guide vanes between the hub and the shroud.

Volvo Aero Corporation (VAC), specializes in the manufacturing of components for both military and commercial engines, rockets and industrial gas turbines [Cor10]. As a supplier to all of the main aero engine companies of the world, Volvo Aero is continually seeking to make improvements in the design and production of the components. Fuel saving is one important environmental issue to develop improvements in the design of the components. One of the specializes of the company is the turbine rear frame. Development of appropriate technologies is required in order to maintain a leading position in the manufacturing of turbine rear frames. Integrated analysis and design tools in the concept of computational fluid dynamics (CFD), are some of the appropriate technologies [Cor10]. This thesis discusses an investigation of the in-house CFD-based design tool, initially used for aero design of the outlet guide vanes, located in the turbine rear frame.

1.3 Outlet guide vane aerodynamics

As noted above, one of the primary purposes of the outlet guide vane (OGV), is to eliminate the tangential component of the air flow in the turbine rear frame. This is accomplished by giving the frame struts an airfoil shape, as illustrated in the following figure. The struts thus are denoted vanes.

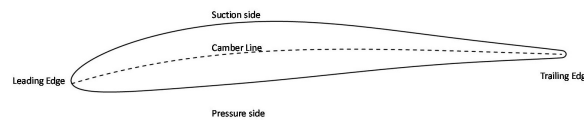


[Ips10]

Figure 1.3: Sketch of an outlet guide vane indicating the important areas: A=leading edge, B=trailing edge, C=shroud side, D=hub side, E=suction side, and F=pressure side.

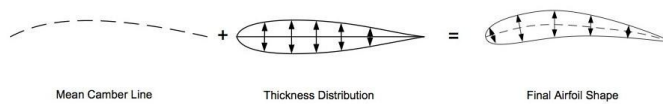
The geometry of an outlet guide vane is shown in 2D in Figure 1.4. The leading and trailing edges have a radius of curvature and are connected by a chord. (Note that the radius of curvature at the trailing edge is not shown in the figure). The mean camber line defines the airfoil curvature and is the median between the suction side and the pressure side. The thickness distribution is symmetrical and correspond to half the distance between the suction side and the pressure side measured along the mean camber line. The mean camber line together with the thickness distribution generates the final airfoil shape of a blade profile, Figure 1.5. The coordinates for the airfoil are found by superimposing the coordinate of the camber line with the coordinate of the thickness distribution.

The airfoil geometry is described by several different parameters, including the maximum thickness (T_{max}), the location of T_{max} (along the chord), the maximum camber and the maximum camber location as well as the leading edge radius.



[Rob10]

Figure 1.4: Geometry of an outlet guide vane.



[Rob10]

Figure 1.5: A camber line together with a thickness distribution generate a final airfoil shape.

The aerodynamic forces acting on an airfoil surface (in a free stream V_∞) can be divided into surface pressure p normal to the surface, associated with lifting force, and shear stress τ tangential to the surface, associated with drag force, as indicated on small surface element dS in Figure 1.6.

The element force dF acting on dS is defined:

$$dF = -p\mathbf{n}dS + \boldsymbol{\tau}m dS \quad (1.1)$$

The total aerodynamic force \mathbf{F} acting on the airfoil is the sum of all the elemental forces. The lift force is generated by the pressure distribution while the drag force is generated by both pressure distribution and shear stress [Rob10].

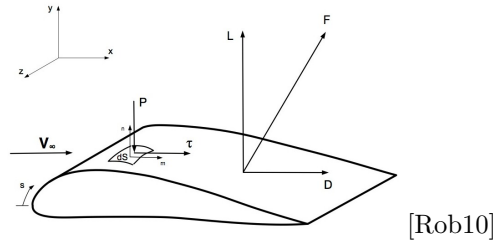


Figure 1.6: *Aerodynamic forces on an airfoil.*

The pressure distribution of an airfoil gives useful information about the vane characteristics. C_p is a non-dimensional coefficient commonly used to present the pressure distribution. The stagnation point is located where the local flow velocity is zero, typically near the leading edge. For incompressible flows, $C_p = 1$ at the stagnation point. This value is larger in compressible flows. The flow velocity is slowest at the pressure side, where C_p and the pressure level have maximum values and is largest where C_p has a minimum value, the so-called suction peak. If shock waves are present, they occur just aft of the suction peak. The pressure distribution depends on the airfoil shape and thickness and is a determining factor in the extent of the pressure recovery area. This area occurs in the region aft of the suction peak, where $\frac{\partial p}{\partial x} > 0$. Separation or transition is most likely to occur in this region. The trailing edge pressure depends on the airfoil characteristic near the trailing edge. As a consequence, great positive C_p values at the trailing edge leads to a larger pressure recovery area.

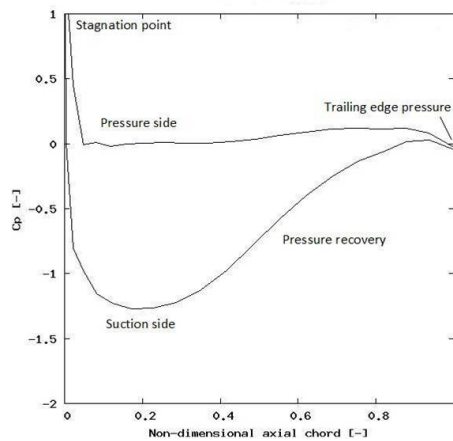


Figure 1.7: *Pressure distribution on an airfoil.*

2 Objectives

There are two major objectives of this thesis work:

- Design tool validation.

A reference design of an outlet guide vane is initially created in *Volvane*. The dimensions of the outlet guide vane are based on realistic assumptions of a middle sized jet engine. The design is simulated with the *Volvane 2D panel* solver, *G3D Euler* solver and with several turbulence models and two different mesh sizes in RANS-solvers. After analyzing the solver results the mesh size, turbulence model and RANS-solver is selected and used for further investigations in the thesis. Then the aim is to evaluate the design tools and to find general prediction trends for the *Volvane* solvers. Five different design of experiments (DoEs) are set up. Design parameters and boundary conditions in the DoEs are varied to investigate how the flow behaves around the outlet guide vanes for different geometries and operating conditions. The same changes are simulated in the selected RANS-solver and the results compared with those of the *Volvane* program. This objective is the focus of Part 1 of the thesis.

- Efficient design process.

Minimizing the number of design parameters may result in efficient design process in *Volvane*. Response surface methodology (RSM) is employed in a statistical analysis and optimization tool to investigate correlations between design and output parameters. The variables in the previous DoEs are used as a base for the RSMs. The strength of the correlations is analyzed in order to reduce the number of design parameters. This objective is covered in Part 2.

3 Approach

- Part 1

Volvane is an Excel-based in-house design tool used to create guide vanes. The tool contains a *2D panel* solver and an inviscid *G3D Euler* solver. Further details about *Volvane* are explained in section 5. Initially, a reference design of a guide vane (located in the turbine rear frame of a jet engine) is created in *Volvane*. The dimensions of the vane are based on realistic assumptions of a middle sized jet engine and a total number of 10 vanes is used in this turbine rear frame.

In the first part of this project, the reference design is created in *Volvane* and simulated with the *Volvane 2D panel* solver and the *G3D Euler* solver. The objective is to evaluate *Volvane* as a design tool and to compare the *G3D Euler* solver with RANS-solvers. To create grids for the RANS-solvers, the geometry of the reference design is exported from *Volvane* to a *G3D* mesh script. A wall function mesh and a low Reynolds mesh is created. *Volvol ++* and *Fluent 12.1* are the two different RANS-solvers used. The reference design is simulated in *Volvol ++* with the following turbulence models: *rk - ε* model using the wall function mesh and the low Reynolds mesh is solved with the *k - ε Chien* model, *k - ω* model and finally the *k - ω SST* model. In *Fluent 12.1*, the low Reynolds mesh is computed by the *rk - ε* model. After analyzing the solver results, the mesh size and turbulence model used for further investigations of the thesis are selected. In the analysis, different parameters are investigated such as outlet swirl angle, the pressure distribution, diffusion factor etc. The reference design is described in section 7.

Design tool validation is described in section 9. Five different design of experiments, (DoEs) are created. DoE-A contain changes in lean and sweep, while robustness regarding inlet conditions are analyzed in DoE-B. Camber line and thickness modifications are the bases for DoE-C and DoE-D respectively. DoE-E is similar to DoE-C but some parameter bounds are doubled. Different design parameters are selected for the investigation and the DoEs are simulated with the *Volvane G3D Euler* solver and the chosen RANS-solver. The following selected output parameters are in focus: XVmax, diffusion factor, loss coefficient and the outlet swirl angle.

- Part 2

Design process rationalization is described in section 10. Response surface methodology, (RSM) is employed in *modeFRONTIER*, which is a commercial optimization and statistical analysis tool used to perform design parameter investigations. The DoEs from Part 1 are used as the base for the response surface methodology, to create response surfaces. For all the selected output parameters, second order polynomial response surfaces are used. A Monte Carlo-like simulation approach is used for the statistical analysis. In *modeFRONTIER*, the data from the created RSMs produce information of possible correlations between design parameters. The strength of the correlations is analyzed in order to reduce the number of design parameters used, and the correlations are used as measures of how different parameters are related.

4 Technical background

This section reviews some essential technical concepts underlying the analysis performed in the thesis work.

4.1 Design of Experiments

Design of experiments is a systematic way to investigate a process by a series of designed tests. Planned changes are made to input variables of the tests and the effects of those changes are investigated [The]. It is desirable to plan the experiment in such a way as to keep the required number of tests at a minimum, while at the same time assuring that reliable results are obtained. In creating a design of experiment (DoE), a number of design parameters are selected for the purpose of creating the design space. Upper and lower bounds are chosen for each design parameter, defining the boundary of the DoE and the bounds is then normalized to values of $+1$ and -1 , respectively [Wal08].

There are several different designs of the DoE models to choose from. Central composite design (CCD) is a family of designs containing different 2nd order models, including face centered composite design (FCCD) the model used in this thesis. The CCD is illustrated in Figure 4.1 and consist of a 2^k -factorial with a total of D design points, where $D = 2^k + 2k + n_c$, k is the number of design points and n_c is the number of center points. The main idea behind the CCD model is a 2^k -factorial, which is usually used in order to fit a second order model [Ore06]. The FCCD model has the axial points located in the center of the faces of the DoE, as illustrated in Figure 4.2. A drawback of this model is that it is non-rotatable. The economic advantage of the model is that it requires fewer center points than the CCD model [Ore06]. This model was chosen for the work in this thesis because it has been found to provide good results and is commonly used at the Aerothermodynamics department at Volvo Aero.

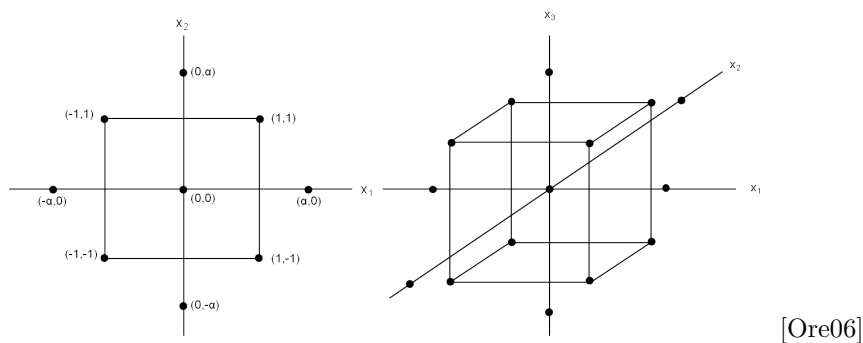


Figure 4.1: An illustration over the CCD model in 2 and 3 dimensions.

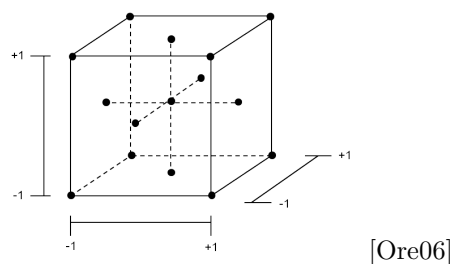


Figure 4.2: An illustration over the FCCD model in 3 dimensions.

4.2 Response Surface Methodology

Response Surface Methodology is a statistical method used to analyze problems where several variables are involved and the aim is to find relations between design variables and response variables. DoE theory is used to find an optimal response surface. The output parameters of the candidate design in the DoEs are used to create a suitable regression model [Wal08].

There exist various types of regression models. Of the ones available, a second order polynomial response surface is used in Part 2 of the thesis. If \bar{x} is the design parameter vector itself and $y(\bar{x})$ is the true objective function, then, According to [Wal08], the regression model can be defined:

$$y = \beta_0 + \sum_{i=1}^k \beta_i x_i + \sum_{i=1}^k \beta_{ii} x_i^2 + \sum_{i < j=2}^k \sum_{i < j=2}^k \beta_{ij} x_i x_j + \epsilon \quad (4.1)$$

where y is the objective function, β is the regression coefficient, ϵ is the error, k is the number of design parameters and x_i denotes the i^{th} design parameter. The fitted regression model is then defined in the following way [Wal08]:

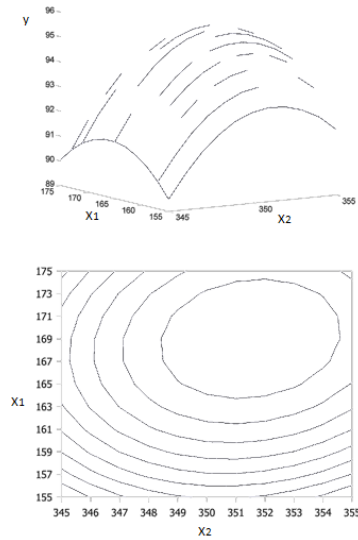
$$\hat{y} = b_0 + \sum_{i=1}^k b_i x_i + \sum_{i=1}^k b_{ii} x_i^2 + \sum_{i < j=2}^k \sum_{i < j=2}^k b_{ij} x_i x_j \quad (4.2)$$

where \hat{y} is an approximation of the true response y generated by a least-squares fit of a second order polynomial and the b 's are least-squares estimates of the regression coefficients.

An example of a response surface and contour plot is shown in Figure 4.3. If x_1 and x_2 are considered independent input parameters and y is the output. Then, according to Eqn (4.1) and (4.2):

$$y = b_0 + b_1 x_1 + b_2 x_2 + b_{11} x_1^2 + b_{22} x_2^2 + b_{12} x_1 x_2 \quad (4.3)$$

is generated by a least square linear regression.



[Rsm]

Figure 4.3: A schematic response surface with a contour plot.

4.3 Potential flow solver

Potential flow is characterized by an irrotational velocity field. To make the equation suitable for panel computations, the Laplace equation for potential flow must be transformed into integral form. In order to solve the equation system in a panel solver, the geometry in this case airfoils must be discretized. That is, divided into panels located around the airfoil. The panel solver computations result in a numerical solution for inviscid flow. In potential flows viscous and compressible effects are omitted. Simulation of a potential flow with a 2D panel solver results in a relatively fast solution process, compared with a 3D solver, but important aspects of the flow are omitted, for example 3D effects, of course. The following set of equations describes potential flows according to [Car03]:

The continuity equation for incompressible flow is

$$\frac{\partial u}{\partial x} + \frac{\partial v}{\partial y} = 0 \quad (4.4)$$

and the vorticity equation is

$$\frac{\partial v}{\partial x} - \frac{\partial u}{\partial y} = \zeta. \quad (4.5)$$

The stream function describing a 2D continuous flow is

$$u = \frac{\partial \psi}{\partial y} \quad v = \frac{\partial \psi}{\partial x} \quad (4.6)$$

The velocity potential describing a 2D irrotational flow is

$$u = \frac{\partial \phi}{\partial x} \quad v = \frac{\partial \phi}{\partial y} \quad (4.7)$$

Substitution results in the Laplace equation:

$$\frac{\partial^2 \phi}{\partial x^2} + \frac{\partial^2 \phi}{\partial y^2} = 0 = \frac{\partial^2 \psi}{\partial x^2} + \frac{\partial^2 \psi}{\partial y^2} \quad (4.8)$$

4.4 Inviscid flow solver

Simulations based on the inviscid Euler equations provide an approximation to real fluid problems. For flows around airfoils, the equations provide reasonable estimates but viscous effects are excluded. The equations can only be solved numerically. If irrotational flows are considered, the Euler equations reduce to the Laplace equation, Eqn (4.8) [Car03].

The following equations define the conservative form of the 3D Euler relationships governing inviscid flow:

$$\frac{\partial \rho}{\partial t} + \frac{\partial(\rho u)}{\partial x} + \frac{\partial(\rho v)}{\partial y} + \frac{\partial(\rho w)}{\partial z} = 0 \quad (4.9)$$

$$\frac{\partial(\rho u)}{\partial t} + \frac{\partial(\rho u^2 + p)}{\partial x} + \frac{\partial(\rho uv)}{\partial y} + \frac{\partial(\rho uw)}{\partial z} = 0 \quad (4.10)$$

$$\frac{\partial(\rho v)}{\partial t} + \frac{\partial(\rho uv)}{\partial x} + \frac{\partial(\rho v^2 + p)}{\partial y} + \frac{\partial(\rho vw)}{\partial z} = 0 \quad (4.11)$$

$$\frac{\partial(\rho w)}{\partial t} + \frac{\partial(\rho uw)}{\partial x} + \frac{\partial(\rho vw)}{\partial y} + \frac{\partial(\rho w^2 + p)}{\partial z} = 0 \quad (4.12)$$

$$\frac{\partial(\rho h_0)}{\partial t} + \frac{\partial(\rho h_0 u)}{\partial x} + \frac{\partial(\rho h_0 v)}{\partial y} + \frac{\partial(\rho h_0 w)}{\partial z} = 0 \quad (4.13)$$

4.5 Viscous flow solver

In viscous flows, 3D effects of the fluid flow around objects are taken into account. The fluid flow is continuous and steady and can exist in both laminar and turbulent manners. To understand this 3D effect of the motion around objects in viscous flows, one must solve the governing equations.

The following instantaneous Favre-Averaged Navier-Stokes equations describe the motion and are derived according to Wilcox [Wil93]:

for mass conservation:

$$\frac{\partial \rho}{\partial t} + \frac{\partial(\rho u_i)}{\partial x_i} = 0 \quad (4.14)$$

for momentum:

$$\frac{\partial(\rho u_i)}{\partial t} + \frac{\partial(\rho u_i u_j)}{\partial x_j} = -\frac{\partial p}{\partial x_i} + \frac{\partial t_{ij}}{\partial x_j} \quad (4.15)$$

for energy:

$$\frac{\partial}{\partial t} [\rho(e + \frac{1}{2}u_i u_i)] + \frac{\partial}{\partial x_j} [\rho u_j (h + \frac{1}{2}u_i u_i)] = \frac{\partial u_i t_{ij}}{\partial x_j} - \frac{\partial q_j}{\partial x_j} \quad (4.16)$$

For a Newtonian fluid the relation between stress and strain rate is defined in the following way:

$$t_{ij} = 2\mu s_{ij} + \zeta \frac{\partial u_k}{\partial x_k} \delta_{ij}, \quad (4.17)$$

where the instantaneous stress tensor is

$$s_{ij} = \frac{1}{2} \left(\frac{\partial u_i}{\partial x_j} + \frac{\partial u_j}{\partial x_i} \right) \quad (4.18)$$

and δ_{ij} is the Kronecker delta.

The second viscosity ζ is related to the first molecular viscosity μ in the following way:

$$\zeta = -\frac{2}{3}\mu \quad (4.19)$$

This assumption is commonly used for all gases in CFD simulations.

The heat-flux vector q_j origins from Fourier's law for heat conduction and can be expressed as follows:

$$q_j = -\kappa \frac{\partial T}{\partial x_j} \quad (4.20)$$

The ideal gas law relates pressure, density and temperature in the following way

$$p = \rho RT \quad (4.21)$$

Applying the Reynolds decomposition for instantaneous turbulent flow, the instantaneous velocity is separated into two parts in order to obtain mass averaged mean conservation equations:

$$u_i(t) = (\tilde{u}_i + u_i''(t)), \quad (4.22)$$

where

$$\tilde{u}_i = \frac{\overline{\rho u_i}}{\bar{\rho}} \quad (4.23)$$

is the average of the instantaneous velocity, and u_i'' is the fluctuation. Turbulent flow can be represented with one time independent velocity. The same argument is used for decomposition of the other flow property terms:

$$\begin{aligned}
 p &= (P + p') \\
 \rho &= (\bar{\rho} + \rho') \\
 h &= (\tilde{h} + h'') \\
 e &= (\tilde{e} + e'') \\
 T &= (\tilde{T} + T'') \\
 q_j &= (q_{Lj} + q'_j)
 \end{aligned} \tag{4.24}$$

Substitution of Eqn 4.22 and 4.24 into Eqn 4.14 to 4.16 and Eqn 4.21, followed by carrying out mass-averaging operations results in the Favre-mass averaged mean conservation equations [Wil93]:

$$\frac{\partial \bar{\rho}}{\partial t} + \frac{\partial(\bar{\rho} \tilde{u}_j)}{\partial x_j} = 0 \tag{4.25}$$

and

$$\frac{\partial(\bar{\rho} \tilde{u}_i)}{\partial t} + \frac{\partial(\bar{\rho} \tilde{u}_i \tilde{u}_j)}{\partial x_j} = -\frac{\partial \bar{P}}{\partial x_i} + \frac{\partial}{\partial x_j} [\bar{t}_{ij} + \tau_{ij}] \tag{4.26}$$

$$\frac{\partial}{\partial t} [\bar{\rho}(\tilde{e} + \frac{\tilde{u}_i \tilde{u}_i k}{2})] + \frac{\partial}{\partial x_j} [\bar{\rho} \tilde{u}_j (\tilde{h} + \frac{\tilde{u}_i \tilde{u}_i k}{2})] = \frac{\partial}{\partial x_j} [\tilde{u}_i (\bar{t}_{ij} + \tau_{ij})] - \frac{\partial}{\partial x_j} (q_j + q_j^t) \tag{4.27}$$

where q_j^t is the turbulent heat conduction approximated as

$$q_j^t \approx -\frac{C_p \mu_t}{Pr_t} \frac{\partial T}{\partial x_j} \tag{4.28}$$

The Reynolds stress tensor in the Favre-mass averaged mean conservation equations is usually obtained in the following way:

$$\tau_{ij} = \overline{-\rho u_i'' u_j''} \approx 2\mu_T (S_{ij} - \frac{1}{3} \frac{\partial \tilde{u}_k}{\partial x_k} \delta_{ij}) - \frac{2}{3} \bar{\rho} k \delta_{ij} \tag{4.29}$$

where the set of terms on the right hand side represent the Boussinesq assumption and includes μ_T , which is the eddy (or turbulent) viscosity. The Boussinesq assumption holds that the Reynolds stress tensor τ_{ij} is proportional to the mean strain rate tensor S_{ij} [CFD10].

4.6 Boundary layers

Constant stress layers usually occur near the wall regions in turbulent flows. The boundary layers are divided into inner and outer layers and different sub-layers. The outer boundary layers create shear stresses near the wall. The following boundary layer equations are from [Geo08].

Friction velocity is defined as:

$$u_*^2 = \frac{\tau_\omega}{\rho}, \quad (4.30)$$

where τ_ω is the wall shear stress. The flow close to the wall can be described in the following way:

$$\frac{\tau_\omega}{\rho} = -\langle uv \rangle + \nu \frac{\partial U}{\partial y}, \quad (4.31)$$

and the friction velocity equation can be rewritten

$$u_*^2 = -\langle uv \rangle + \nu \frac{\partial U}{\partial y}. \quad (4.32)$$

y^+ is a dimensionless coordinate defining the position in the near-wall layer:

$$y^+ \equiv \frac{y}{\eta} = \frac{yu_*}{\nu}. \quad (4.33)$$

The different sub-layers are divided as follows in Table 4.1. The linear sub-layer is located close to the wall. The Reynolds stress term negligible and the mean velocity profile is linear at the wall.

The viscous sub-layer is also called the buffer layer. In this region the viscous stresses dominate but both the viscous and the Reynolds stresses are important.

The meso-layer is part of the inertial sub-layer. Here the Reynolds stress is important even though the energy of the turbulence is influenced by the viscosity. The outer boundary layer is located above the inertial sub-layer. Free stream flow exists above the outer boundary layer [Geo08].

Sub-layer	y^+
Linear	$y^+ < 3$
Viscous	$3 < y^+ < 30$
Meso-layer	$30 < y^+ < 300$
Inertial	$30 < y^+ < 3000$

Table 4.1: The dimensions of the reference design.

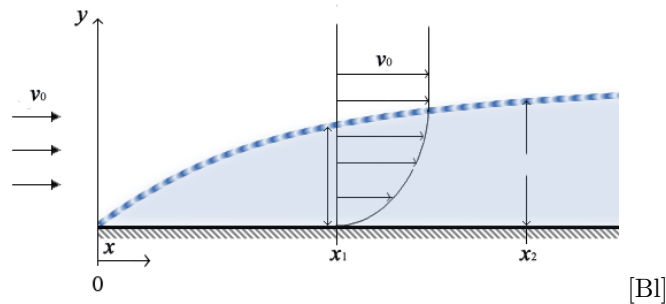


Figure 4.4: *Boundary layer development over a plate where v_0 is the free stream velocity. No-slip condition yields at the wall. The linear sub-layer is located closest to the wall.*

To predict separation of viscous flows, it is important to know how accurate the turbulence solvers predict the flow close to the wall of the object.

4.7 Turbulence modeling

Turbulence can be described as a state of fluid motion consisting of three dimensional vortices. Turbulent flow is both time and space dependent and behaves in a chaotic manner when the disturbances of the flow are not damped by the flow itself. Turbulence increases with Reynolds number, with energy taken from the original laminar flow [Geo08].

Reynolds Average Navies Stokes (RANS) models are commonly used to represent turbulent flow problems. They can be separated into different categories according Davidson [Dav03]:

Boussinesq based turbulence models

According to Boussinesq, momentum transfer by eddies may be modeled with an eddy (or turbulent) viscosity.

- *Linear eddy viscosity models*

These are algebraic models based on the assumption that the Reynolds stress tensor is related to the turbulent viscosity and the velocity gradients by the Boussinesq assumption.

- *Nonlinear eddy viscosity models*

The relationship between the mean turbulence and the mean velocity fields is represented by a nonlinear equation in these models.

- *One-equation models*

In the one-equation model the transport equation is solved for the turbulent kinetic energy and the turbulent length scale. The length scale is obtained from an algebraic expression.

- *Two-equation models*

These are very commonly used eddy viscosity models. Two transport equations are used and history effects of the flow can be taken into account.

Reynolds stress models

The model contains a transport equation derived for the Reynolds tensor. In order to determine the turbulent length scale, a transport equation for the dissipation is added.

Large eddy simulations

In large eddy simulations, large eddies of the flow are dependent on the geometry and the smaller scales are considered as universal. Larger scales are explicitly solved during simulations and the small scales are implicitly solved using the sub-grid scale model.

Direct numerical simulations

Navier-Stokes equations are numerically solved without a turbulence model, requiring that the entire range of scales be resolved. This model is mostly useful for numerical experiments in turbulence research, due to the requirement of extremely large computational sources [Dav03].

Among the categories above, the Boussinesq based *two-equation models* are the most common ones used in the industry, as they are relatively economical and provide sufficiently accurate results. The following models are used in this thesis work:

Standard $k - \epsilon$ model

This Boussinesq based eddy viscosity model consists of two transport equations. The turbulent kinetic energy k is used to describe the energy in the flow. The dissipation ϵ is the other transport parameter [CFD10]. One advantage of the $k - \epsilon$ model is that it provides accurate predictions for fully turbulent flows. A disadvantage of the model resides in the viscous sub-layer, close the wall where viscous effects dominate. In this area, accurate predictions of the flow require fine grid mesh. Grid points should be located just outside the viscous sub-layer. From that location, one can assume the computational results of the model to be valid at the wall too, although in reality this can be inaccurate. The the $k - \epsilon$ model is commonly used for wall function grids in industrial applications, since it provides accurate results for fully developed flow while at the same time being reasonably economical.

rk - ϵ model

The $k - \epsilon$ *realizable model* is a version of the standard $k - \epsilon$ model. The model contains a realizable term satisfying mathematical constraints on the Reynolds stress tensor. The $rk - \epsilon$ model is often used at Volvo Aero for aero-design of turbine rear frames.

k - ϵ Chien model

Other forms of the $k - \epsilon$ model provide better predictions of viscous effects, for example the $k - \epsilon$ *Chien*. This model is considered a low Reynolds model and contains damping functions to better predict viscous effects by the wall, compared with the standard $k - \epsilon$ model.

Standard k - ω model

This is a two-equation model used for computations of low Reynolds meshes, k describes the energy in the flow while ω is the specific dissipation rate. Regarding flows in the adverse pressure gradient, the $k - \omega$ model provides better predictions than the standard $k - \epsilon$ model, since the model predict smaller amounts of shear stress [Dav03]. The main disadvantage with this model is the sensitivity to free stream flows.

k - ω SST model

This branch of the $k - \omega$ model is a commonly used turbulence model within turbo-machinery. The model is suitable for a wide variety of flows since it consists of a combination of the $k - \omega$ model for the inner boundary layer and the $k - \epsilon$ model for the outer boundary layer and beyond. There is no need for extra damping functions. The SST application switches to $k - \epsilon$ behavior in the free-stream flow. A general $k - \omega$ model is usually too sensitive to the turbulence properties of the inlet free-stream. One of the disadvantages with this turbulence model is the over-prediction of turbulence levels in regions with stagnation or large acceleration, although this result in better prediction than the standard $k - \epsilon$ model [CFD10]. This model is used for off-design analysis of the outlet guide vanes located in turbine rear frames, since the model is known to slightly over-predict separative tendency.

Wall treatment

High Reynolds turbulence models are wall functions, used to solve a wall function mesh. The flow near the wall is assumed to behave as a fully developed turbulent boundary layer. The wall functions relate the velocity to the surface shear stress. In the mesh, the first node is located outside the wall region. In reality the wall function assumptions lead to inaccurate results, especially for flow near solid boundaries and for separated flows. The models however, are economical since they do not require as much computational time as the low Reynolds models.

Low Reynolds turbulence models are used to solve a low Reynolds mesh, providing more accurate predictions for the turbulence closer to the wall. In the mesh, the first node is located at $y^+ < 3$. Viscous effects are dominant close to the wall. Low Reynolds models predict more accurate flow results than high Reynolds models, but require more computational time due to the large mesh size.

5 Volvane - aerodesign tool for vanes and ducts

Volvane is an in-house design tool used to create guide vanes and includes a 2D potential flow solver and a 3D Euler solver named *G3D Euler*. The *Volvane* program is built in Excel using Visual Basic scripting.

In the "Sections"-sheet you will find settings to define the camber line and the thickness distribution around the camber line. The types of camber lines implemented in *Volvane* are circular, exponential, 3rd and 5th order polynomial, NACA 2-digit and NACA 6-series. The implemented thickness distributions are NACA-4, 4M, 6 and MNp5p. NACA airfoils are commonly used for blade profile design. They are based on analytical equations describing the camber line, chord line, and the thickness distribution. There exist several different series of NACA airfoils. MNp5p is an in-house created thickness distribution based on a parabolic profile added to a 5th order polynomial.

As mentioned in Section 1.3, a camber line together with a thickness distribution defines a blade profile. A blade is completed when the blade profiles are stacked along an axis or a curve. Figure 5.1 shows how the profiles are stacked along a straight axis. This axis is not necessarily straight, as shown in the figure. The vane is generally stacked in the location of the maximum thickness.

To design a blade, initially you have to choose a camber line and thickness distribution. The blade sections located around a stacking line have to be created. Each blade section is placed radially in % of the span. 0% of the span represent the hub and 100% of the span represent the shroud. Prior to the panel solver computations, the blade sections have to be stacked along an axis. Before the computations in *G3D Euler* solver, a 3D mesh should be created. The solver solutions are visualized in the "Flow"-sheet of the program and the solver data is written to the "Sections"-sheet. The 3D geometry is written in an in-house data format for use with CAD and mesh-tools. Design settings can be imported and exported in XML-files.

The different "*Volvane*"-sheets contains several auxiliary tools. In the "*Endwalls*"-sheet you will find modifications and endwall contouring of the gaspath. On this sheet, graphs of the gaspath curvature, splines and area distribution are shown. In the "*Geometry*"-sheet the blade sections with the stacking line are visualized. Another tool is the airfoil curvature, shown in Figure 5.5. The curvature is useful to investigate when the blade design need corrections. The camber line angle and curvature as well as the axial chord are shown in the "*Camber*"-sheet. In the "Thickness"-sheet, the thickness distribution around the blade is visualized. The leading edge radius of curvature and trailing edge wedge angle are other useful tools.

The "*Flow*"-sheet contains plots of the velocity, C_p distribution, Stratford separation criterion, V_{max} and throat positions. The computational grid and graphs of the pressure and Mach number distributions at the vane and the end walls, generated by the *Volvane G3D Euler* solver are located on this sheet. By specifying data points in the "Own Thickness"-sheet, you can manually create a thickness distribution.

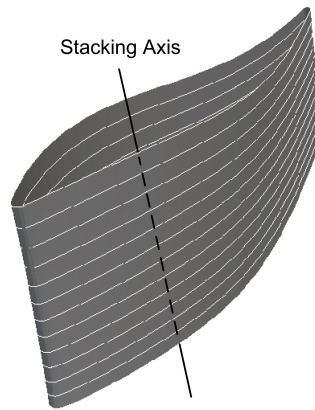
In the "*Stack*"-sheet you can modify settings for the stacking. For example where to position the stacking point on each section. The type of lean specification can be set to local or global. Local lean specifies the lean of the stacking line as the angle between the stacking line and the radial line to the current position. Local lean gives an exact control of the lean related to the endwalls, while the global lean specifies lean related to the y-axis which results in exact control of the overall shape of the stacking line [Vol].

The "*Setup*"-sheet contains all the settings for the computational domain and the solvers. The "*Gaspath*"-sheet contain settings for the gaspath, shroud and ridge computations for polygonal shroud. The number of input points used to specify the hub and the shroud in the gaspath can be set manually. If the number of points should be changed, it is important to change the graphs in the "Geometry"-sheet as well. The numbers of output points are set to re-spline an existing gaspath. The "*BC*"-sheet contain settings for the boundary conditions.

The "*Multi*"-sheet specifies the number of input design XML files. The multi functions spline the design parameters of two or more defined designs to generate other output designs. This optimization tool can be used to test several different designs in the series of interpolated and extrapolated designs or to work on several different designs in parallel. Another auxiliary tool in *Volvane* is the "*DoE*"-section where a DoE can be generated. Before generating a DoE matrix, the selected design and output is read into the program. Then candidate design sets can be created and exported as VTK files. In *Volvane* the following DoE models are implemented: Latin-Hypercube, Face-centered composite design, Circumscribed central composite design and Inscribed central composite design.

The contents of the "*Volvane*"-sheets are shown in Table 5.1.

Volvane sheet	Contents
Sections	Post solver results, computed geometrical and stacking properties
Endwalls	Modification and layout of gaspath
Geometry	Airfoil curvature and stacking plots
Camber line	Camber line angles and curvatures, Axial chord plot
Thickness	Thickness distribution, Min pressure location, LE radius of curvature
Flow	Plots of velocity, Cp distribution and separation, grid, pressure and Mach distribution
Own Thickness	Manual settings for camber length and thickness
Stack	Stack settings
Setup	Solver settings
Gaspath	Manual gaspath settings
BC	Boundary conditions settings
Multi	Optimize and test a design generated by spline the design parameters
DOE	Settings to create a design of experiment

Table 5.1: Contents of the *Volvane* Excel sheets.

[Rob10]

Figure 5.1: A typical guide vane with all the blade profiles stacked along an axis. (The stacking axis is not necessarily straight, as shown in the figure).

The shape of the camber line has a large effect on the pressure distribution of the vanes [Lew96]. To construct a camber line in *Volvane* (using the JL exp 2 type of camber), the following parameters can be adjusted:

- Type of camber line, (implemented in the program)
- Axial chord mm
- LE camber angle $^\circ$
- LE camber angle d/ds
- LE camber angle d^2/ds^2
- TE camber angle $^\circ$
- TE camber angle d/ds
- TE camber angle d^2/ds^2
- Desired axial position mm

When constructing a camber line, the adjustable parameters should be initiated. To investigate the design, plots with the camber line angle and curvature are useful tools. Since the camber line together with the thickness distribution generate the blade profile, *Volvane* provide plots where the airfoil sections with a stacking line around the origin, thickness distribution and airfoil curvature are shown. In the "Sections"-sheet, one can choose which spans should be activated during the design process. Only activated spans are shown in the plots.

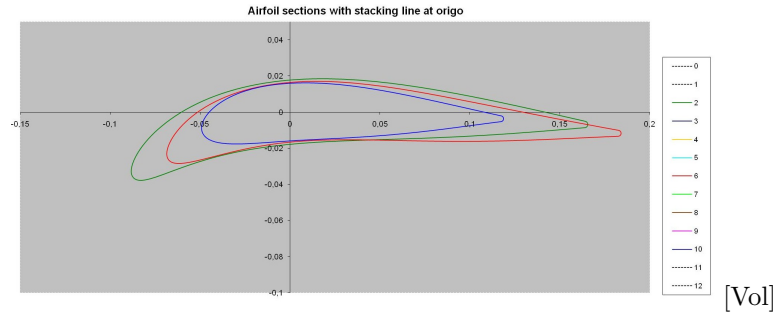


Figure 5.2: Activated spans in Volvane stacked along the origin. Only the hub, shroud and mid-span are activated. The numbers in the table to the right represents the spans. Number 2 in the table represents the hub (0%-span), number 6 represents the mid-span (50%-span) and the number 10 represents the shroud (100%-span).

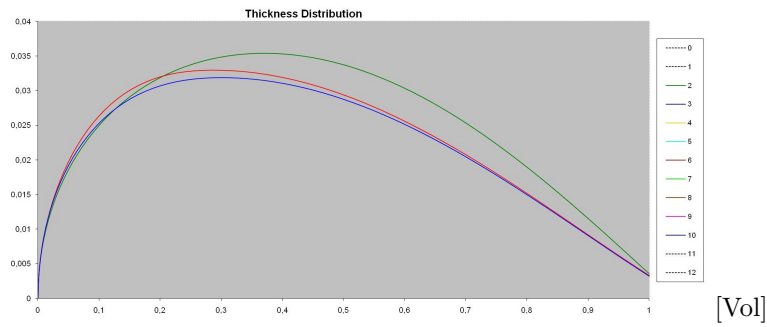


Figure 5.3: The thickness distribution in Volvane including hub, shroud and mid-span. The numbers in the table to the right represents the spans. Number 2 in the table represents the hub (0%-span), number 6 represents the mid-span (50%-span) and the number 10 represents the shroud (100%-span).

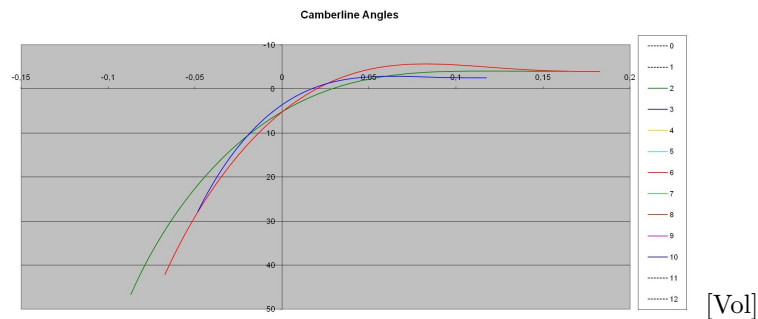


Figure 5.4: The camber line angle in Volvane including hub, shroud and mid-span. The numbers in the table to the right represents the spans. Number 2 in the table represents the hub (0%-span), number 6 represents the mid-span (50%-span) and the number 10 represents the shroud (100%-span).

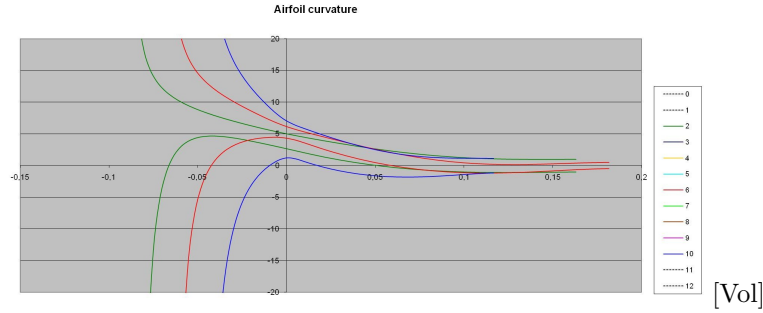


Figure 5.5: An airfoil curvature from Volvane including hub, shroud and mid-span sections. The numbers in the table to the right represents the spans. Number 2 in the table represents the hub (0%-span), number 6 represents the mid-span (50%-span) and the number 10 represents the shroud (100%-span).

A representation of the pressure distribution by the *Volvane G3D Euler* solver at the vane and at the end walls is shown in Figure 5.6. If the pressure gradient is severe, one could suspect separation to occur in the region of the adverse pressure gradient.

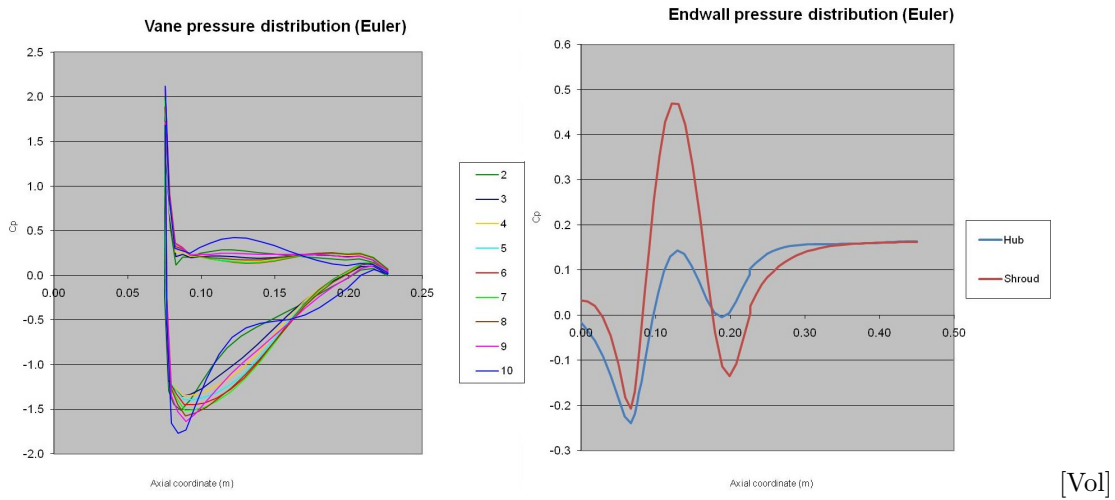


Figure 5.6: The pressure distribution by the *Volvane G3D Euler* solver is shown at the vane and around the end walls.

5.1 Volvane output parameters

The *Volvane 2D panel* solver is a potential flow solver. This solver is based on an estimation of a three dimensional flow. The governing flow equations are simplified and the geometry must be discretized. The solver consists of a superposition of a *2D* flow, when the flow follows a blade to blade sequence. The following parameters are evaluated from the solver [Vol]:

Outlet swirl angle.

The outlet swirl angle is defined as the angle between the tangential and axial velocity components. The main purpose of the outlet guide vane is to de-swirl the airflow, and the objective is to achieve a minimal outlet swirl angle. The targets are set to maximum $\pm 3^\circ$ from 0° swirl. In the *Volvane 2D panel* solver, the governing equations are simplified and the boundary layer development in the computations is omitted.

Deviation angle

The deviation angle is the difference between the camber line angle at the trailing edge and the outlet flow angle. As a rule of thumb, the angle should be below 3° . A larger deviation angle may result in an insufficient control of the outlet flow angle.

Maximum velocity (Vmax)

Vmax represents the suction peak. The depth of the peak is an important parameter for high Mach number flows, when the aim is to keep the velocity below supersonic. In the *Volvane 2D panel* solver Vmax is calculated without any effects of compressibility or varying gas channel heights.

Vmax axial position (XVmax)

The XVmax corresponds to the axial position of the maximum velocity, hence the suction peak.

Diffusion factor (DF)

The diffusion factor gives an initial indication of the load level of the vane. Generally a diffusion factor level above 0.4 is considered to indicate a heavy load. Increasing this level above 0.6, may result in separation and high losses.

Definition DF:

$$DF = \frac{V_{max} - V_{out}}{V_{max}} \quad (5.1)$$

Diffusion factor, 3D estimation

The Diffusion factor, 3D estimation indicates how the gas-channel height will affect the velocities predicted in the 2D panel solver.

Stratford separation coefficient

The Stratford separation coefficient gives an indication if the boundary layer of the flow is going to separate. A separation index is computed from the location of V_{max}/P_{min} towards the trailing edge. At a certain C_p value the index will stop. An index below zero results in separation. According to Stratford, the ideal airfoil profiles have an index equal to zero. This fact considers 2D flows only, but in reality separations occur in 3D flows. It is the secondary flow along the end-walls that interacts with the suction surface and result in separation. The Stratford separation criterion is conservative and can be used as an indicator of the margin to separation for a newly created design compared to previous created designs. This criterion can also be used as an indicator of the margin to separation at the different axial positions of the suction side of the vane.

The following parameters apart from those described in the section *Volvane 2D panel* solver, are evaluated from the *Volvane G3D Euler* solver [Vol]:

Inlet and outlet Mach number

Mass flow averaged Mach number at the inlet and the outlet of the domain.

Loss coefficient

The loss coefficient is estimated from the flow velocities computed by the solvers. The definition of the loss coefficient in the *Volvane G3D Euler* solver is based on Denton's boundary layer correlation. The definition also includes a simple wake loss estimate.

6 Analysis tools

The following analysis tools are used in this project:

Volsol++

Is an in-house RANS-solver and frequently used in this thesis. The solver equations are supported by the *G3DFLOW* series of codes, created by [Eri95]. The codes are based on cell-centered finite volume approach. The corresponding mesh contains multi blocks and is curved linear, non-orthogonal and boundary fitted. A third order upwind scheme is used for the convective flux and a second order accurate scheme is used for the diffusive flux [Wal08].

Fluent

Fluent is a commonly used commercial CFD software package. The software is suitable for different applications of CFD problems [Ans10]. *Fluent* exists in several updated versions. *Fluent* 12.1 is used for the reference design. The advantage with *Fluent* is the capability to apply several different settings, meshes and turbulence models [Ans10]. For the reference design the following conditions were set up: Pressure based, Second order discretization schemes, Green Gauss cell based gradient method. This is according to Volvo Aero best-practice.

modeFRONTIER

Is a commercial optimization and statistical analysis design tool. And contains different orders of integration, optimization and post-processing applications. Different settings of DoEs and RSM techniques can be applied.

7 Reference design

The reference design was created in *Volvane* and consists of a gaspath and outlet guide vanes. The design is based on the assumption of a medium sized jet engine, (25000lbs of thrust). A total number of 10 vanes are used in this turbine rear frame. The dimensions of the reference design are shown in Table 7.1 and shows realistic values for a medium sized turbine rear frame. Since the gaspath design is not included in the scope of this thesis, the endwall radii are constant. This is not a typical gaspath, but removes the gaspath influences of the study. Some area ruling is included, however, since all real gaspaths do to some extent, and it was believed that the simple gaspath with constant radii would be a little more representative if that was so.

Parameters	Dimensions (mm)
Total domain length	450
TRF gaspath length	225
Pitch	205
Axial chord	150
Tmax	25
TEthickness	3

Table 7.1: The dimensions of the reference design.

At the hub, XTmax is set to 35% of the camber line length.

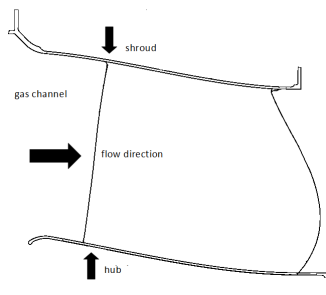


Figure 7.1: A schematic cross section of a gaspath.



Figure 7.2: The outlet guide vane of the reference design.

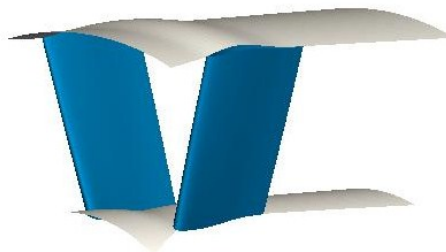


Figure 7.3: The outlet guide vane with the gaspath located in the turbine rear frame.

7.1 Computational domains

To create computational domains for the RANS-solvers, the data of the reference design were exported from *Volvane* and meshed by G3D mesh which is an in-house meshing tool. Both a wall function mesh and a low Reynolds mesh were created. To be able to transfer the mesh script into *Fluent* 12.1, the mesh was first exported into the Patran neutral file format.

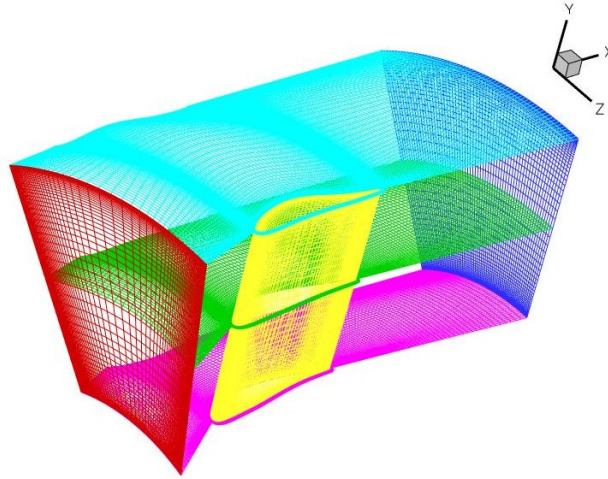


Figure 7.4: *The 3D mesh of the reference design.*

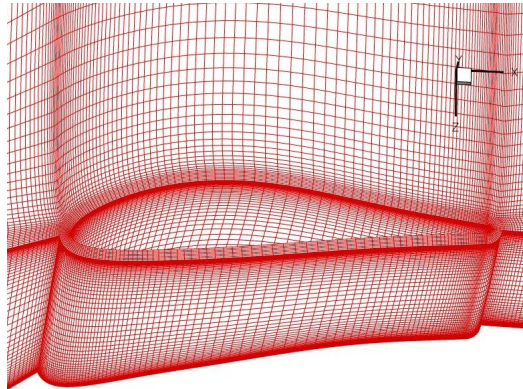


Figure 7.5: *Reference vane in detail with the refined grid around the vane.*

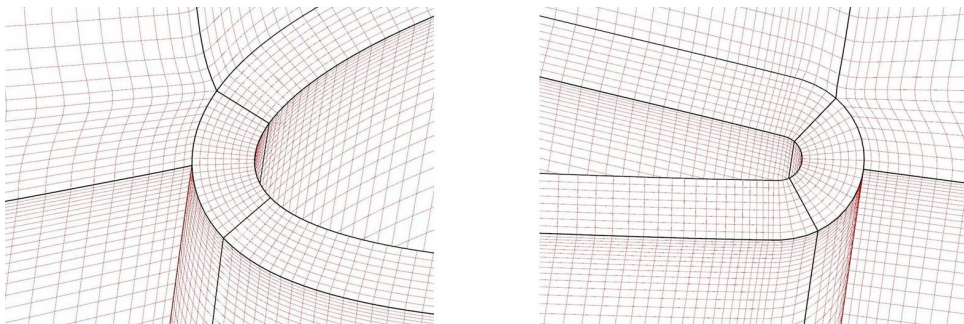


Figure 7.6: *The refined grid of the reference design with the leading and trailing edge zoomed.*

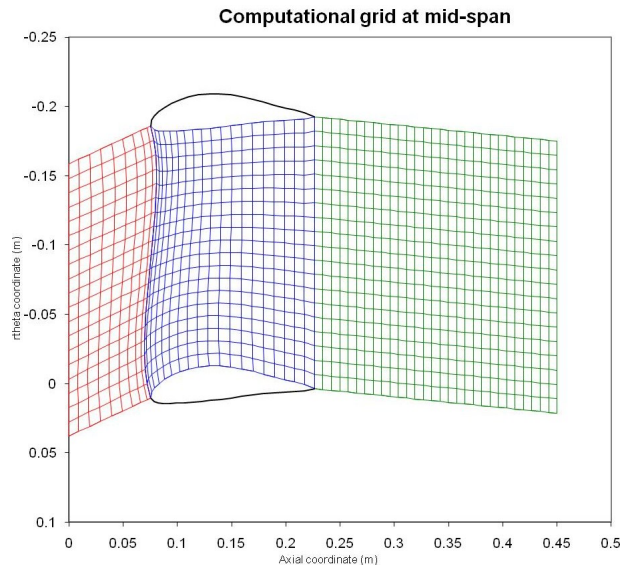


Figure 7.7: The Euler mesh of the reference design.

Table 7.2 shows the number of grid points around the vane for the Euler mesh, the wall function mesh and the low Reynolds mesh. The numbers of grid points are specified in chord-wise, pitch-wise and span-wise directions around the vane and in the O-grid. The O-grid consists of grid lines where the grid points are placed around the object. No O-grid exists in the Euler mesh. The numbers of grid points are specified at the trailing edge and at the leading edge. Near wall spacing indicate the closest distance to the wall where the solvers have predicted the flow. y^+ is the dimensionless coordinate defining the position in the near-wall boundary layer.

The discretization or mesh generation corresponds to the actual cell size in the mesh and allow the solver equations to be applied in a discrete form. In general, a minor cell size result in a better solver prediction than a major cell size. The discretization generated by the different grids and the total number of nodes are shown in Table 7.2. The grids used are compliant with Volvo Aero best-practice.

Region	Euler	Wf	Low Re
Chord-wise	20	91	91
Pitch-wise	20	51	51
Span-wise	17	61	101
O-grid	N/A	9	24
Near wall spacing	$9 \cdot 10^{-3}m$	$0.5 \cdot 10^{-3}m$	$1 \cdot 10^{-5}m$
y^+	N/A	$\approx 30 - 35$	≈ 1
LE	N/A	20	20
TE	N/A	20	20
Discretization	$7.5mm$	$1.65mm$	$1.65mm$
Total number of nodes	1.87×10^4	8.10×10^4	1.67×10^6

Table 7.2: Table of mesh characteristics.

7.2 Boundary conditions

The boundary conditions of the reference design are shown in Table 7.3. The boundary conditions used are based on simplified engine realistic conditions. For the inlet P_0 and the swirl angle, the parameters are averaged.

Parameter	Inlet	Outlet
T_0 (K)	650	
P_0 (Pa)	37546	
P (Pa)		33500
Massflow (kg/s)	1.49	
Swirl ($^\circ$)	-17	

Table 7.3: Boundary conditions of the reference design. The inlet of P_0 and the swirl are averaged values.

The turbulence solvers were provided with added boundary condition profiles. In the initial version of *Volvane 2.4.2*, the *G3D Euler* solver was not provided with specific P_0 and T_0 profiles. Simulations with the *G3D Euler* solver were not satisfactory since too many errors occurred in the flow results. This fact came to an updated version of *Volvane 2.5.0 beta*, which was provided with the ability to interpret boundary condition profiles in the *G3D Euler* solver. The different profiles are shown in Figures 7.8 and 7.9. The blue graph indicates the initial lack of boundary profiles in *Volvane 2.4.2*. The violet graph shows the boundary condition profiles from *Volvane 2.5.0 beta* while the green graph indicates the RANS-solver profiles. The final boundary condition setting used for the reference design are later applied to all CFD analysis.

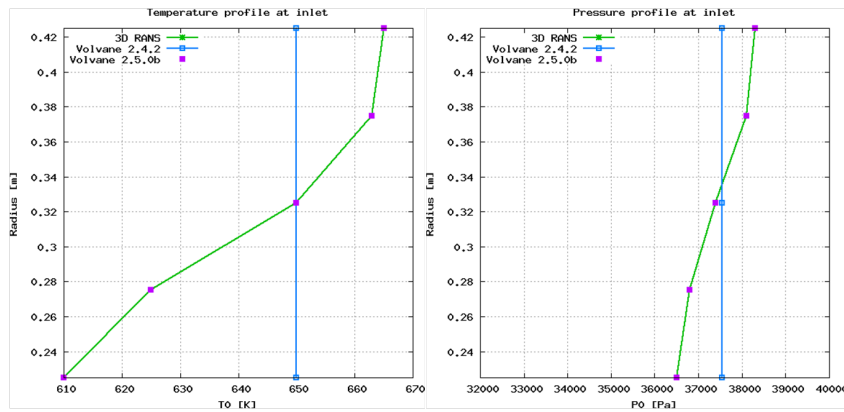


Figure 7.8: Boundary condition profiles for T_0 and P_0 . The blue graph indicates the lack of profiles in *Volvane 2.4.2*, while the other graphs show the profiles added in version *Volvane 2.5.0 beta* and the profiles for the *RANS-solver*.

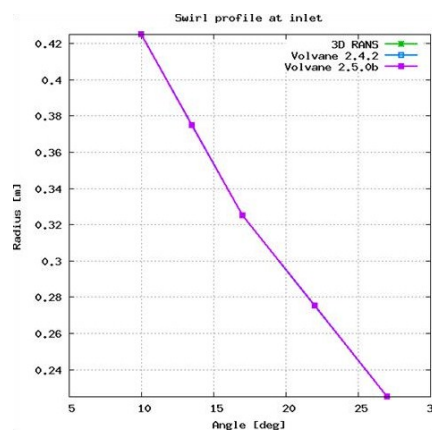


Figure 7.9: The swirl profile for all three solver versions. Only one graph is shown since all the graphs coincides with each other.

The ideal gas law is used to represent the conditions of the air and the Sutherland law for the viscosity is applied.

7.3 Results for the reference design.

The aim of the study is to analyze the predictability of the *Volvane G3D Euler* solver compared with RANS-solvers. Table 7.4 shows the output parameters from the *G3D Euler* solver in *Volvane 2.5.0 beta*, compared with the selected RANS-solvers. The output parameters are evaluated at 50%-span. Table 7.5 shows the loss coefficient and mass-flow, evaluated over all the spans.

The loss coefficient is evaluated by :

$$\frac{P_{0in} - P_{0out}}{P_{0in} - P_{sin}} \quad (7.1)$$

<i>Parameter, 50% – span</i>	<i>G3D Euler</i>	<i>wf, rκ – ϵ</i>	<i>Chien</i>	<i>κ – ω</i>	<i>SST</i>	<i>Fluent, rκ – ϵ</i>
Outlet swirl angle(°)	-0.33	-2.37	-0.65	-0.70	-1.12	-0.78
Vmax (m/s)	295	311	-	313	311	224
Vmax axial position (mm)	101	111	-	111	111	111
Diffusion factor (-)	0.33	0.38	0.36	0.36	0.35	0.33
Inlet Ma number (-)	0.42	0.41	0.42	0.41	0.41	0.42
Outlet Ma number (-)	0.40	0.40	0.40	0.40	0.40	0.40

Table 7.4: Output parameters from *Volvane G3D Euler* solver compared with parameters of different turbulence models. In *Volsol ++*, both the wall function mesh and the low Reynolds mesh are used. In *Fluent 12.1*, the $r\kappa - \epsilon$ model in the low Reynolds mesh is used. The output parameters are evaluated at 50%-span.

<i>Parameter, overall</i>	<i>G3D Euler</i>	<i>wf, rκ – ϵ</i>	<i>Chien</i>	<i>κ – ω</i>	<i>SST</i>	<i>Fluent, rκ – ϵ</i>
Loss coeff (%)	1.66	4.45	-	4.21	4.16	4.26
Mass flow (kg/s)	15.20	14.90	14.90	14.90	14.90	14.90

Table 7.5: Parameters from *Volvane G3D Euler* solver compared with parameters of different turbulence models. In *Volsol ++*, both the wall function mesh and the low Reynolds mesh are used. In *Fluent 12.1*, the $r\kappa - \epsilon$ model in the low Reynolds mesh is used. The output parameters are evaluated over all the spans.

Static pressure plots for the different turbulence solvers at different spans are represented in Figures 7.10 and 7.11. The differences in predicting the flow around the vane between the *Volvane G3D Euler* solver and the different RANS-solvers are visualized. This is clearly shown at the suction peak and on the pressure side near the trailing edge. The distinctions are expected since no viscous effects are considered in the *Volvane G3D Euler* solver.

At the trailing edge in Figures 7.10 and 7.11, RANS-simulations using wall functions indicates a "fishtail" shape. This is a un-physical phenomenon. Some known facts in the wall functions contribute to this phenomenon. The wall functions generate a swirl angle difference of 2.5° , compared with the low Reynolds. Figure 7.12 shows pressure plots at the trailing edge in the wall function mesh and the low Reynolds mesh. The wall function mesh is shown at the left side. The pressure level is higher at trailing edge and extremely low in a region at the pressure side of the trailing edge. The low pressure contributes to the "fishtail". The low Reynolds mesh is shown at the right side, where the pressure is smoothly distributed around the whole trailing edge.

Since the prediction by the different RANS-solvers generate similar results, (apart from the TE loading). For the continue of the survey, *Volsol ++* using the *wf r κ – ϵ* solver became the selected turbulence model. This choice saved large amounts of computational time and computer resources.

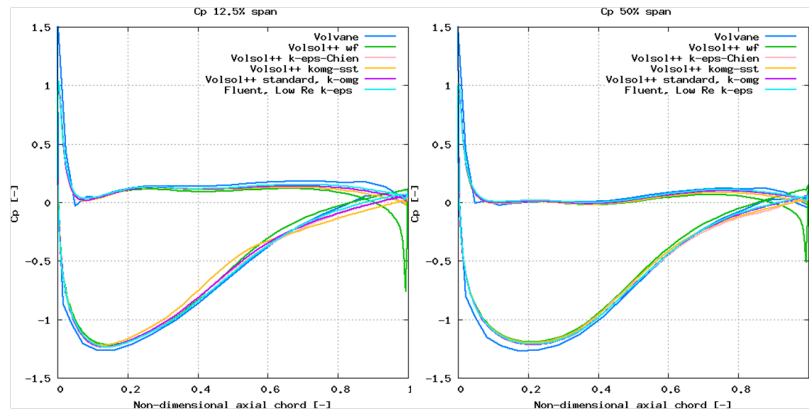


Figure 7.10: Static pressure plots at 12.5%-span and 50%-span for the different solvers.

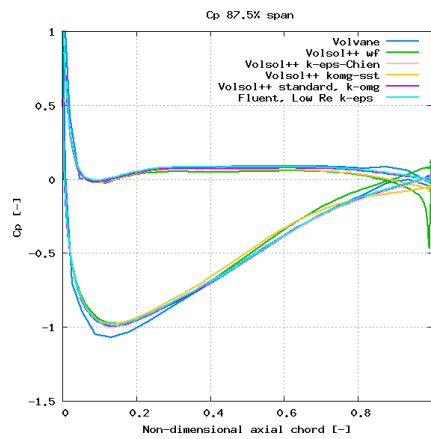


Figure 7.11: Static pressure plot at 87.5%-span for the different solvers.

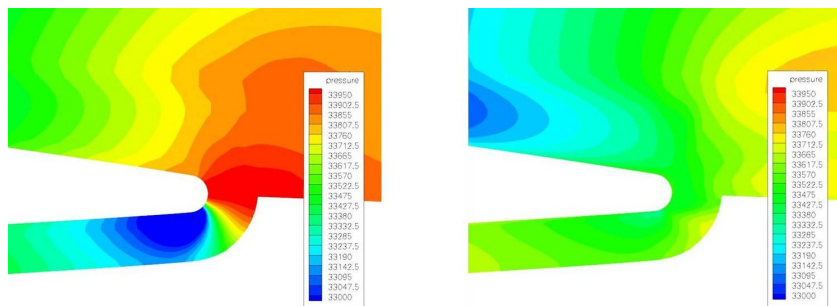


Figure 7.12: Pressure plots at the trailing edge. RANS-solver simulations using the wall function mesh is shown at the left and the low Reynolds mesh is shown at the right. In the wall function mesh, the "fishtail" is indicated by the lower pressure level at the pressure side of the trailing edge, compared to the low Reynolds mesh.

Outlet swirl angle

An important parameter to investigate is the outlet swirl angle, shown in Figures 7.13 and 7.14. The main purpose of the outlet guide vanes is to de-swirl the air flow and the objective is to achieve a minimal angle of the outlet swirl. When comparing the different turbulence solvers, some distinctions between the flow results of the outlet swirl angle were shown. The swirl angle is about 2.5° lower for the wall function solver than for the low Reynolds solvers. The reason can be explained by the "fishtail" phenomenon.

The simulation results using the $\kappa - \epsilon$ *Chien* and the $\kappa - \omega$ model are almost equivalent. The $\kappa - \epsilon$ *Chien* solver predicts a slightly higher swirl angle, especially in the region between the vanes. In *Volsol ++*, the $\kappa - \omega$ *SST* model predicts a lower swirl angle compared with the other low Reynolds solvers. *Fluent 12.1* predict a similar flow pattern, but the swirl angle is generally lower over the region. Simulations with the *Volvane G3D Euler* solver shows a higher swirl degree compared with the RANS-solvers, due to the inviscid character of the solver. Although in the region between the vanes, the swirl angle is slightly lower.

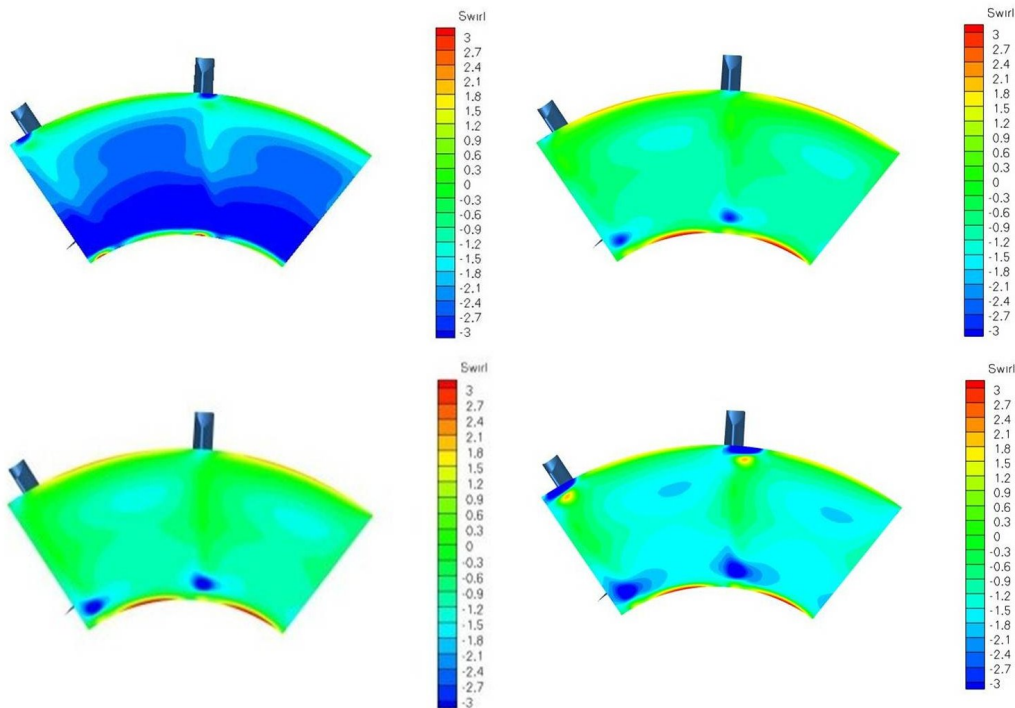


Figure 7.13: Outlet swirl angle simulated in *Volsol ++* using the wf $\kappa - \epsilon$ model to the upper left and using the low Reynolds mesh with the $\kappa - \epsilon$ *Chien* model to the upper right. Simulations with the $\kappa - \omega$ model is shown in the lower left and the $\kappa - \omega$ *SST* model is shown to the lower right.

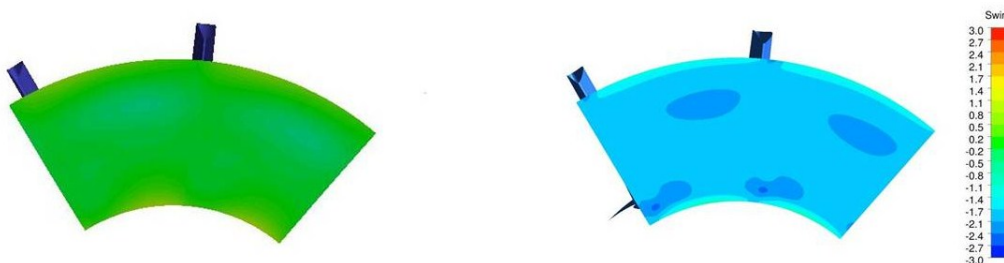


Figure 7.14: Outlet swirl angle simulated in *Volvane* using the *G3D Euler* solver to the left and with *Fluent 12.1*, using the low Reynolds mesh with the $\kappa - \epsilon$ model to the right.

Total pressure distribution

The total outlet pressure is shown in Figures 7.15 and 7.16 and compared between the different solvers. The first case with the $wf \kappa - \epsilon$ solver shows a sharper bend of the wake at the hub, due to the inaccurate predicted outlet angle. All models show similar behaviors. In the solver results between *Volsol ++* and *Fluent 12.1*, there are no major distinctions. All the RANS-solvers have similar wake thickness. The only visible difference between the $\kappa - \epsilon$ *Chien* and the $\kappa - \omega$ model is the shape of the wake located at the hub. A bend of the wake at the shroud is shown in the results for the $\kappa - \omega$ *SST* solver. Compared with the RANS-solvers, the wake of the *Volvane G3D Euler* is straight and expansive. The difference in shape is due to the lack of viscous effects of the solver. In the region between the vanes, there are minor distinctions between the *Volvane G3D Euler* solver and the RANS-solvers.

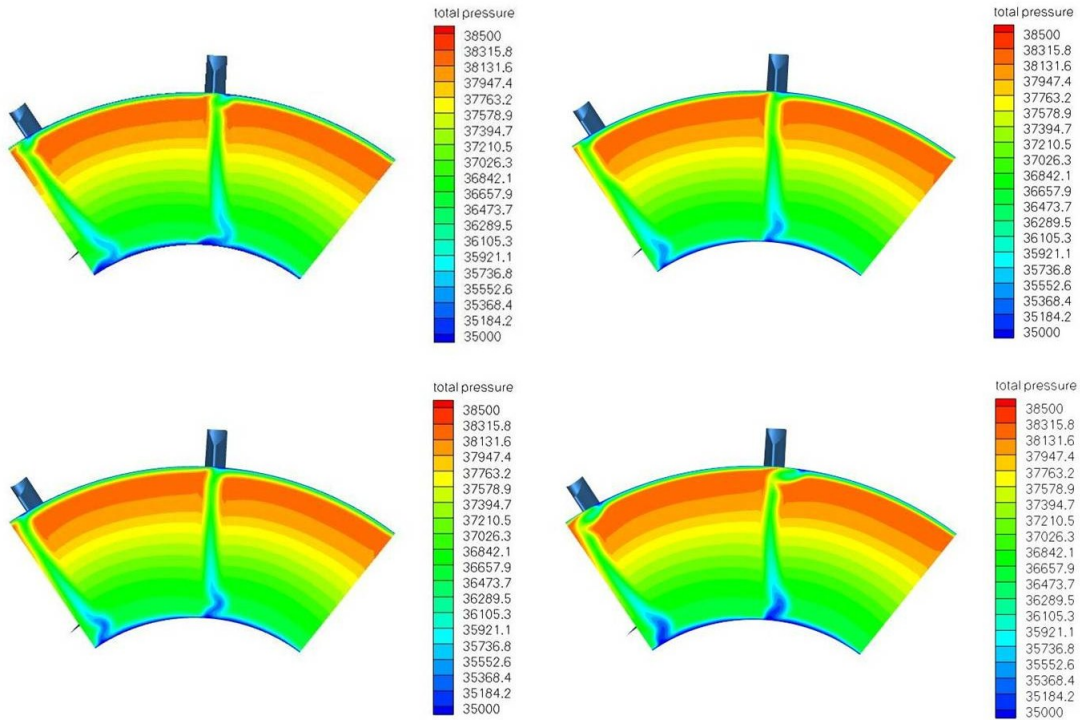


Figure 7.15: Total outlet pressure simulated in *Volsol ++* using the $wf \kappa - \epsilon$ model to the upper left and using the low Reynolds mesh with the $\kappa - \epsilon$ *Chien* model to the upper right. Simulations with the $\kappa - \omega$ model is shown in the lower left and the $\kappa - \omega$ *SST* model is shown to the lower right.

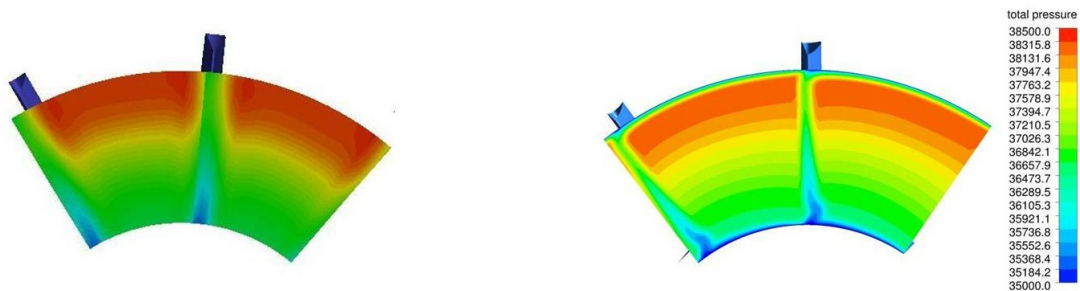


Figure 7.16: Total outlet pressure simulated in *Volvane* using the *G3D Euler* solver to the left and in *Fluent 12.1*, using the low Reynolds mesh with the $r \kappa - \epsilon$ model to the right.

Static pressure distribution

The static pressure on the hub and on the suction side is shown in Figures 7.17-7.19. The flow results between the solvers are similar. Compared with the RANS-solvers, the $\kappa - \epsilon$ Chien model has a slightly lower pressure level in the suction peak. At static pressure, the $wf \kappa - \epsilon$ model seems to predict similar flow results as the solvers using the low Reynolds mesh. In Figure 7.19, the *Volvane G3D Euler* solver predicts lower pressure levels in the suction peak compared with the RANS-solvers.

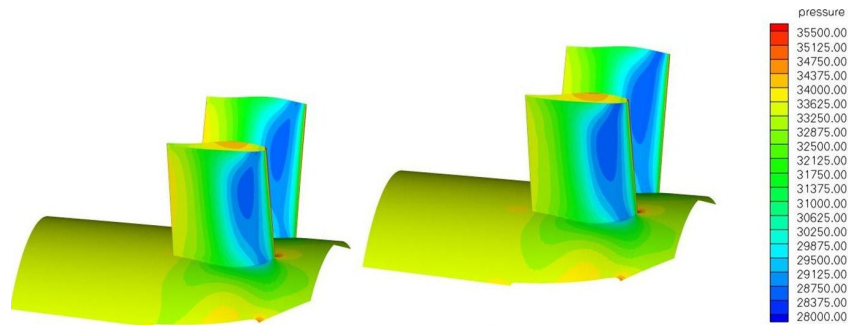


Figure 7.17: Static pressure on the hub simulated in *Volsol ++* with the $wf \kappa - \epsilon$ model to the left and using the low Reynolds mesh with the $\kappa - \epsilon$ Chien model to the right. The $\kappa - \epsilon$ Chien solver achieves lower pressure levels, in the suction peak.

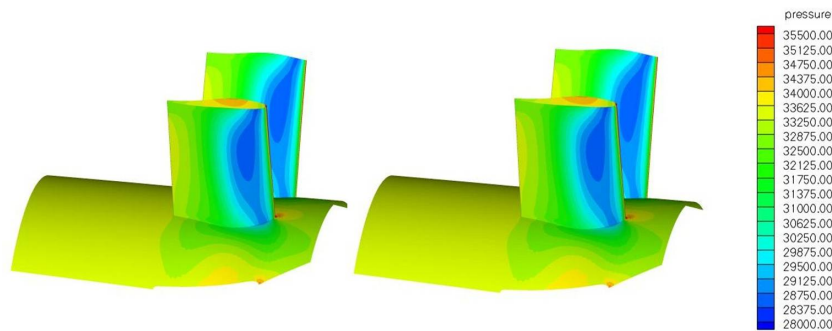


Figure 7.18: Static pressure on the hub simulated in *Volsol ++* using the low Reynolds mesh with the $\kappa - \omega$ model to the left and the $\kappa - \omega$ SST model to the right.

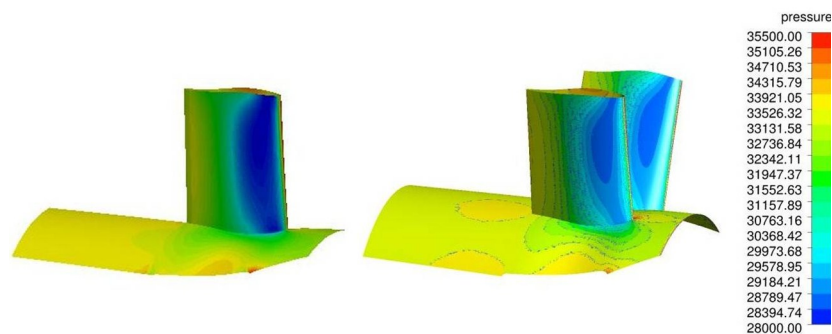


Figure 7.19: Static pressure on the hub simulated in *Volvane* using the *G3D Euler* solver to the left and in *Fluent 12.1*, using the low Reynolds mesh with the $r\kappa - \epsilon$ model to the right.

The static pressure on the shroud and the pressure side are visualized in Figures 7.20-7.22. The pressure side in the results for the $wf \kappa - \epsilon$ model shows a different pattern and achieves a slightly lower pressure level, compared with the other solvers. The flow results between the different low Reynolds solvers are analogous with each other. In Figure 7.22, simulations with the *Volvane G3D Euler* solver shows similarity with the RANS-solvers.

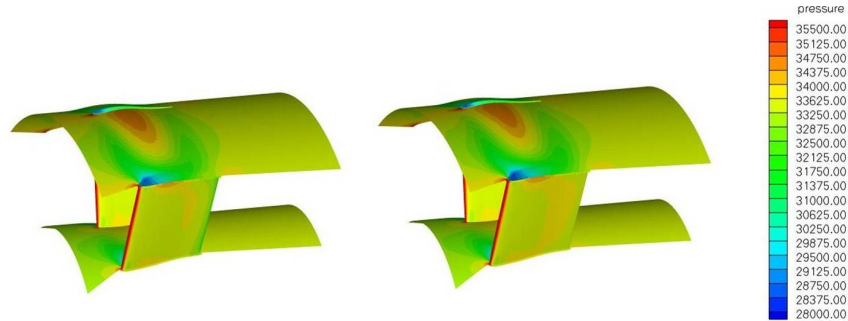


Figure 7.20: Static pressure on the shroud simulated in *Volsol ++* using $wf \kappa - \epsilon$ model to the left, and using the low Reynolds mesh with the $\kappa - \epsilon$ Chien model shown to the right.

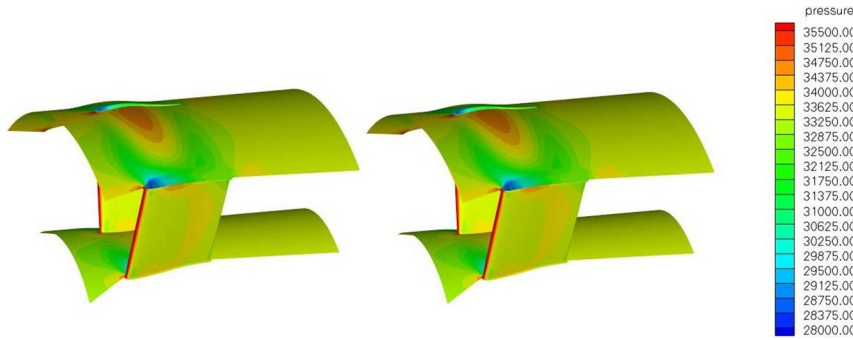


Figure 7.21: Static pressure on the shroud simulated in *Volsol ++*, using the low Reynolds mesh with the $\kappa - \omega$ model to the left and the $\kappa - \omega$ SST model to the right.

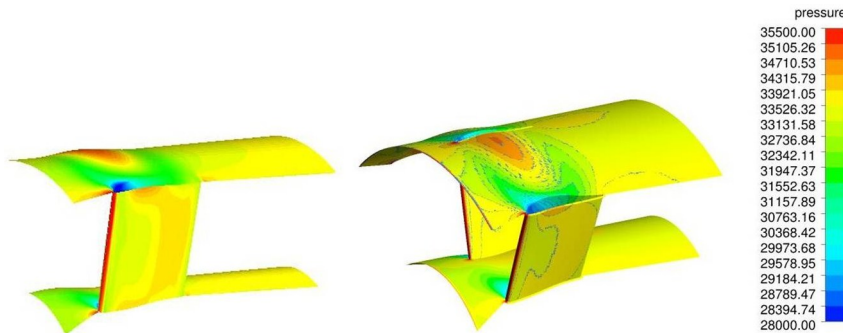


Figure 7.22: Static pressure on the shroud simulated in *Volvane* with the *G3D Euler* solver to the left and in *Fluent 12.1*, using the low Reynolds mesh with the $r\kappa - \epsilon$ solver to the right.

Mach number at mid-span

The Mach numbers on the mid-span indicate how the fluid flow behaves around the vane. In these cases the maximum Mach levels are around 0.2 at the leading edge and nearly zero in the wake at the trailing edge. The maximum Mach level is approximately 0.6 located in the region of the suction peak of the vane. Shown in Figures 7.23-7.25, the flow results from the different RANS-solvers are similar to each other. In Figure 7.25, the *Volvane G3D Euler* shows similarity with the RANS-solvers, apart from the higher Ma numbers at the leading edge and trailing edge. This is a natural effect due to the inviscid *G3D Euler* solver.

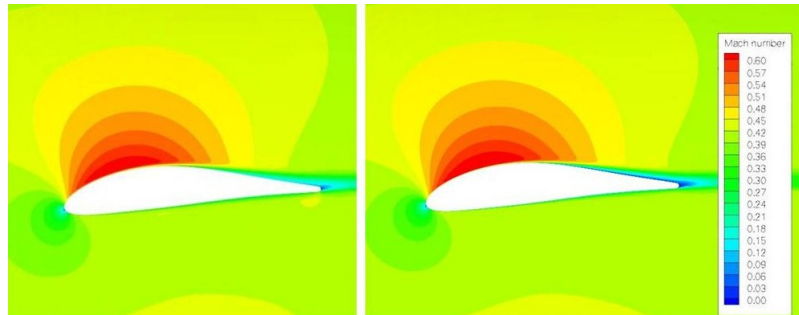


Figure 7.23: Mach number at mid-span simulated in *Volsol ++* with *wf κ-ε* solver to the left and using the low Reynolds mesh with the *κ-ε Chien* solver to the right.

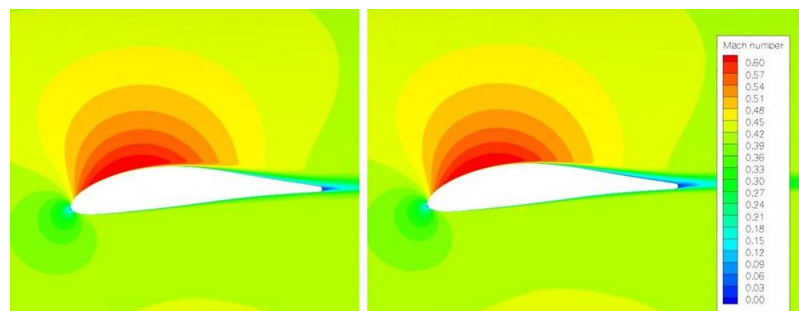


Figure 7.24: Mach number at mid-span simulated in *Volsol ++* using the low Reynolds mesh with the *κ-ω* model to the left and the *κ-ω SST* model model to the right.

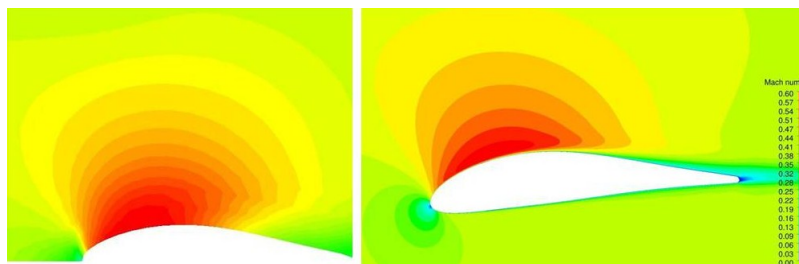


Figure 7.25: Mach number at mid-span simulated in *Volvane* with the *G3D Euler* solver to the left and in *Fluent 12.1*, using the low Reynolds mesh with the *rκ-ε* model to the right.

Near wall resolution

In the coarse wall function mesh, y^+ is located around 30 and reaches a maximum level of $y^+ = 50$. This region is called the meso-layer. In the low Reynolds mesh, the maximum level of y^+ is equal to 1. This location is in the linear sub-layer which is the region very close to the wall. There are some differences between the flow results from the low Reynolds solvers of *Volsol ++* and *Fluent* 12.1. The y^+ is generally located slightly lower in *Fluent* than in *Volsol ++*. A possible reason could be differences in the cell to wall distance calculations.

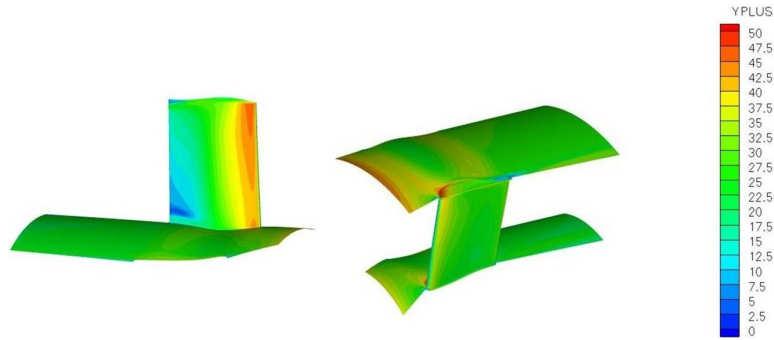


Figure 7.26: y^+ of the hub and the shroud simulated in *Volsol ++* with the wf $\kappa - \epsilon$ solver.

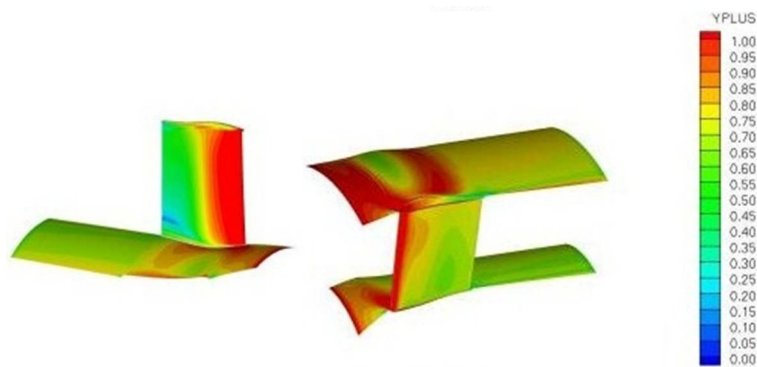


Figure 7.27: y^+ of the hub simulated in *Volsol ++* with the $\kappa - \omega$ model using the low Reynolds mesh.

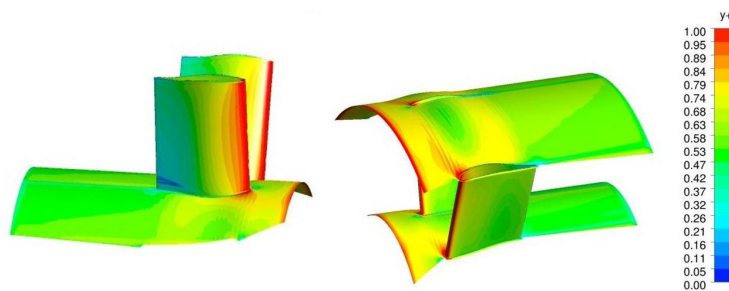


Figure 7.28: y^+ of the hub simulated in *Fluent* 12.1 with the $r\kappa - \epsilon$ model using the low Reynolds mesh.

7.4 Summary & Conclusions for the Reference design.

Volsol ++ using the wall functions mesh appears to predict a satisfactory flow result, keeping in mind the difference of 2.5° in the outlet swirl angle. In this project, *Volsol ++* with wf $r\kappa - \epsilon$ turbulence model was selected for further simulations with RANS. The turbulence model is economic compared with simulations of the low Reynolds mesh since computational time is saved.

8 Contents of the DoEs

The DoEs are constructed for the design tool validation and the design process rationalization. They are used to compare the output parameters from the *Volvane G3D Euler* solver with a RANS-solver. The FCCD model is applied. Five different DoEs were created. Three of them were simulated in *Volvane 2.5.0 beta* and in *Volsol ++*, using the wall functions mesh. The two remaining DoEs were simulated in *Volvane 2.6.3 alpha*. In the first DoE-A, the lean and sweep angle of the vane were changed. Eight different design cases were created and investigated. In the second DoE-B, robustness regarding inlet conditions are analyzed. Six different cases were investigated. The mass-flow and the swirl angle are boundary condition parameters. In DoE-C, the leading edge angle and the derivatives as well as the trailing edge angle of the changed parameters were investigated. This DoE consist of 16 different cases. DoE-D and DoE-E were created in *Volvane 2.6.3 alpha* and used for the design process rationalization. They consist of 80 different cases. In DoE-D, the thickness distribution was modified in order to change and solve for new parameters. DoE-E is similar to the previous one but some parameter bounds have been doubled. Shown in Table 8.1, the DoEs are compiled.

DoE	Description	Number of Cases
A	Lean and Sweep	8
B	Mass-flow and Swirl	6
C	Camber line modifications	16
D	Thickness distribution modifications	80
E	Thickness distribution modifications with parameter bounds duplicated	80

Table 8.1: Table of contents of the DoEs used in the design tool validation and the design process rationalization.

9 Part 1. Design tool validation

In the design tool validation, DoE-A, DoE-B and DoE-C are analyzed and the following parameters are evaluated: Loss coefficient, XVmax position, diffusion factor and the outlet swirl angle. The XVmax position corresponds to the axial location of the suction peak, (minimum Cp value).

Figure 9.1 shows the minimum Cp values for the static pressure curves from *Volsol ++* and *Volvane*. The differences in absolute x-positions (XVmax) are evaluated.

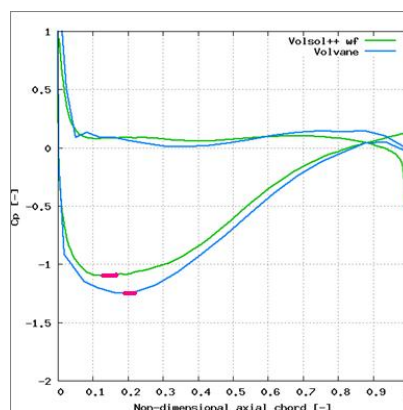


Figure 9.1: An example of XVmax positions of the two different suction peaks. The minimum Cp values are marked.

Initially, the value of the diffusion factor in the *Volvane G3D Euler* solver was too poor, compared with the *Volsol ++* RANS-solver. The problem was solved by changing the way the exit velocity was calculated in the *Volvane G3D Euler* solver. Figure 9.2 shows the diffusion factor differences between the following solvers:

- *Volvane G3D Euler* solver versus *Volvane 2D panel* solver
- *Volsol ++*, $wf r\kappa - \epsilon$ solver versus *Volvane 2D panel* solver
- *Volsol ++*, $wf r\kappa - \epsilon$ solver versus *Volvane G3D Euler* solver

Additionally, the diffusion factor before the alteration of the definition of the C_p value is shown at the left of Figure 9.2. At the right of Figure 9.2, the diffusion factor after the modification is shown. One can clearly notify how the differences in the diffusion factors have decreased.

In this project, the *Volvane 2D panel* solver was initially analyzed, but not presented in this thesis since the main task was to investigate the performance of the *G3D Euler* solver. The prediction of flow results from the *2D panel* solver are analogous to the results from the *G3D Euler* solver.

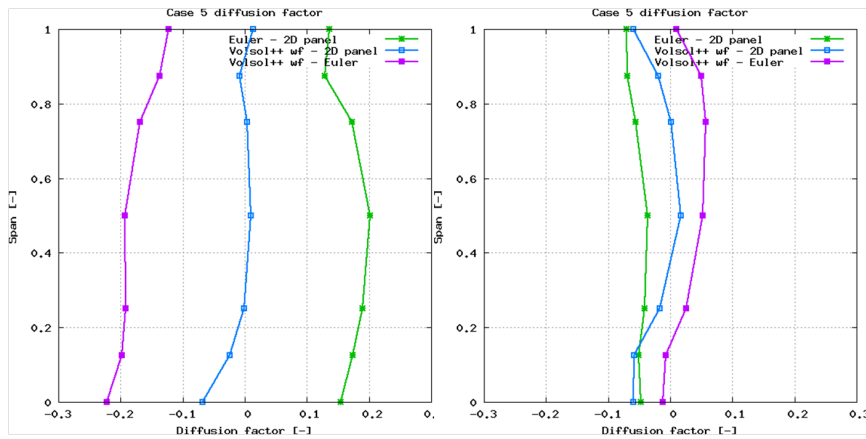


Figure 9.2: An example of the difference in diffusion factor between the *Volvane G3D Euler* solvers, before and after the modification of the definition of the C_p value.

In the DoEs, the ratio of the loss coefficient were analyzed, but not presented in the thesis. The average value of the loss coefficient on mid-span from all the DoEs is about 35%. Here, the loss coefficient is presented in terms of absolute variables.

9.1 DoE-A, lean and sweep

The first DoE was created in the *Volvane 2.5.0 beta* version and simulated with the *Volvane G3D Euler* solver and with *Volsol ++* using the *wf r κ - ϵ* model. Lean and sweep are important parameters, commonly used in blade design to optimize the flow properties of the vane and can be seen in Figure 9.3. Lean is a radial change of the vane location in the turbine rear frame. The lean angle could be located in a positive or a negative direction. Sweep is the axial change of vane position in the turbine rear frame, and can be located in a positive or a negative direction.

DoE-A with the specific cases are shown in Table 9.1. The sweep angle is set to $\pm 10^\circ$ and the changes in lean angle are set to $\pm 30^\circ$. If the lean angle is located between 0° and 30° , there will be too heavy mechanical load on the vane. A lean angle above 40° is structurally inefficient and results in decreased aerodynamic properties. To maintain the mechanical efficiency of the vane, the lean angle should be located between 30° and 40° . In the reference design, there were no lean or sweep angles present.

Case	Lean ($^\circ$)	Sweep ($^\circ$)
0	0	0
1	+30	0
2	-30	0
3	0	+10
4	0	-10
5	+30	+10
6	-30	+10
7	+30	-10
8	-30	-10

Table 9.1: The design cases of DoE-A. Case 0 is the reference design.

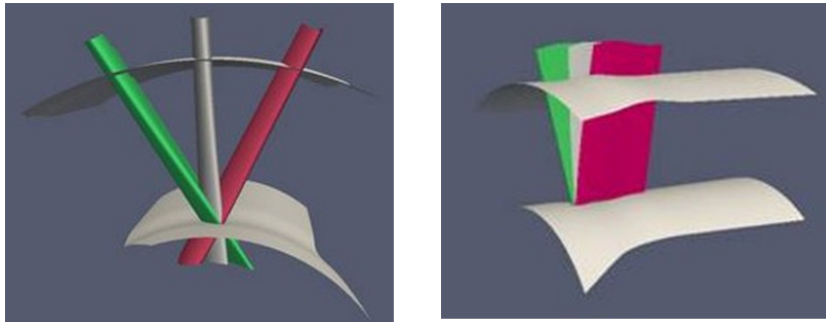


Figure 9.3: Positive and negative lean angles of the outlet guide vane located in the turbine rear frame are shown at the left. The positive and negative sweep angles are shown at the right. The gray outlet guide vane corresponds to the original position while the colored vanes corresponds to positive and negative positions, respectively.

The relative difference of the XVmax position between *Volsol ++* using the *wf r κ - ϵ* model and the *Volvane G3D Euler* solver is shown in Figure 9.4. The different cases are evaluated at mid-span. Cases 2 and 8 have negative lean angles and the largest difference from the reference design, (Case 0) of about 1.25%. Cases 4 and 7 have decreased sweep angles and differs from the reference design with about 0.45%. Cases 1, 5 and 6 have a difference of about 0.1%. Cases 1 and 5 possess an increased lean angle while Case 6 have decreased lean together with an increased sweep.

Case 3 has positive sweep and similarity to the reference design. The *Volvane G3D Euler* solver have difficulties to predict a decreased lean angle followed by a negative sweep angle. The solver has a better ability to predict a change of the lean in a positive direction than in a negative direction. The *Volvane G3D Euler* solver is acceptable in predicting a change of sweep in a positive direction.

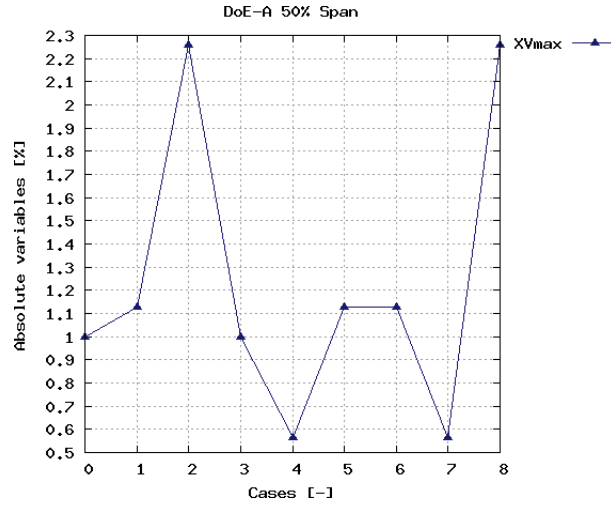


Figure 9.4: *DoE-A*, absolute variables of the *XVmax* position for the *Volvane G3D Euler* and *Volsol ++*, using the *wf rκ - ε* model. The cases are evaluated at mid-span.

Figure 9.5 shows the loss coefficient difference between the solvers at mid-span, evaluated in absolute variables. Case 6 with decreased lean together with an increased sweep has the largest difference from the reference design of about 0.58%. This trend follows by the other cases with decreased lean, Cases 2 and 8. Case 3 has similarity to the reference design, while the remaining cases have a difference of less than 0.05%. The analysis shows that the *Volvane G3D Euler* solver have difficulties to predict a decreased lean angle.

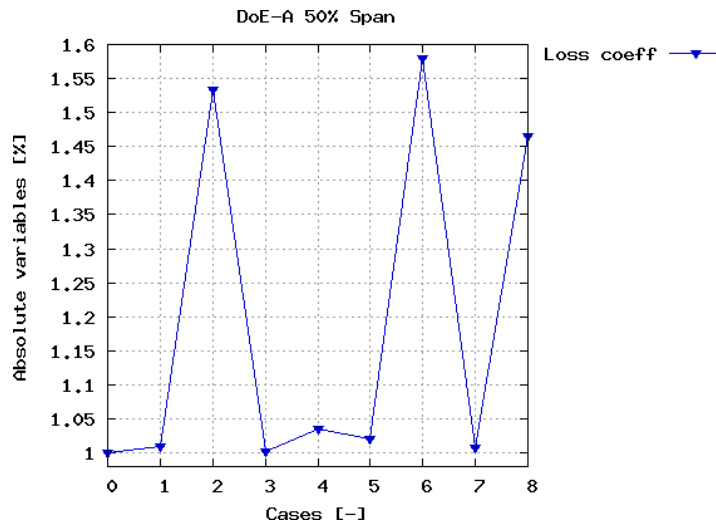


Figure 9.5: *DoE-A*, absolute variables of the loss coefficient for the *Volvane G3D Euler* and *Volsol ++*, using the *wf rκ - ε* model. The cases are evaluated at mid-span.

Figure 9.6 shows the diffusion factor difference for the reference design together with 8 new cases. For the cases with the decreased lean angle (Cases 2, 6 and 8), the largest diffusion factor difference is located at the hub. At 25%-span and at the shroud, the diffusion factor difference for Cases 2, 6 and 8 are close to zero. Case 4 has decreased sweep with no influences of lean. At the hub, the diffusion factor difference for Case 4 is almost zero. The analysis shows that the *Volvane G3D Euler* solver performs a more accurate prediction of the diffusion factor if the sweep is decreased than increased. A negative lean results in difficulties for the solver in predicting an accurate flow result, especially in the region between the hub until 12.5%-span. The average

difference on 50%-span is about 7%. Generally, all the cases follow a similar trend line.

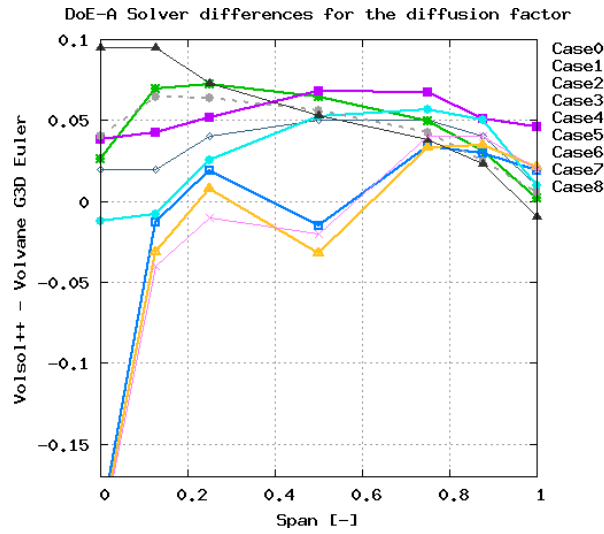


Figure 9.6: The diffusion factor difference on the cases from DoE-A, evaluated at mid-span.

The solver differences of the outlet swirl angle are shown in Figure 9.7. Again the cases with the decreased lean angle have a larger swirl difference, especially at the hub, but the distinctions are almost zero at the shroud. At the hub, Cases 2, 6 and 8 (those with decreased lean), have a swirl angle difference of between -19° to -23° . At 75%-span, the difference is similar to the other cases, about -2° only. The cases with increased lean (Cases 1, 5 and 7), have less swirl angle difference at the shroud compared with the other cases. If the lean angle is negative, the *Volvane G3D Euler* solver seems to have difficulties in predicting accurate flow results in the region between the hub until 75%-span. Case 4 has negative sweep with no changes in lean. At the hub, the difference is about -7° while at 25%-span, the difference is about -3° only. At 25%-span, this is the same difference as for Case 3. The average variance for 50%-span is about -2.4° . Analysis of the outlet swirl angle verifies the previous statements, the *Volvane G3D Euler* solver seems to better predict changes of increased sweep than decreased sweep.

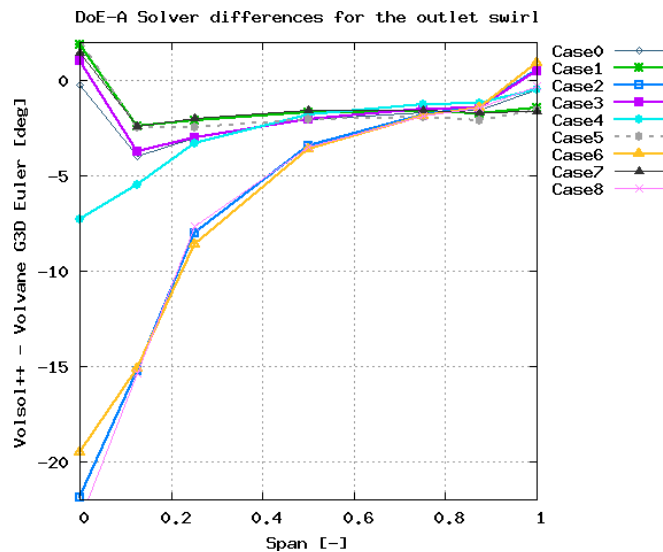


Figure 9.7: The outlet swirl angle difference in the cases from DoE-A, evaluated at mid-span.

9.2 DoE-B, robustness regarding inlet conditions

DoE-B was set up in *Volvane 2.5.0 beta* version and analyzed with the *G3D Euler* solver in *Volvane 2.5.0 beta* and with the *wf rk - ϵ* model in *Volsol ++*. The boundary conditions were changed in order to investigate how the *Volvane G3D Euler* solver behaves for changed boundary conditions. In DoE-B, the mass-flow was changed $\pm 10\%$ and the swirl-angle was changed $\pm 10^\circ$. The different cases are shown in Table 9.2.

Case	Mass-flow (%)	Swirl($^\circ$)
0	0	0
1	+10	0
2	-10	0
3	0	+10
4	0	-10
5	+10	+10
6	+10	-10

Table 9.2: DoE-B design cases.

Cases 5 and 6 are considered extremely off-design cases. On-design is the definition of the "normal" workload of the jet engine, for example the workload of jet engines at cruise level. Off-design is the definition of "extreme" workload of jet engines, for example the workload during take-off.

The differences in the XV_{max} positions between *Volsol ++* using the *wf rk - ϵ* model and the *Volvane G3D Euler* solver, in absolute variables are shown in Figure 9.8. The different cases are evaluated at mid-span and the absolute variables are displayed in %. Cases 3 and 6 have the largest difference from the reference design of about 0.45%. Case 3 has increased swirl angle while Case 6 has decreased swirl angle together with increased mass-flow. The differences between Cases 2 and 5 are about 0.125%. Case 2 has decreased mass-flow while Case 5 has both parameters increased. Case 1 and 4 are similar to the reference design. Case 1 has increased mass-flow while Case 4 has decreased swirl.

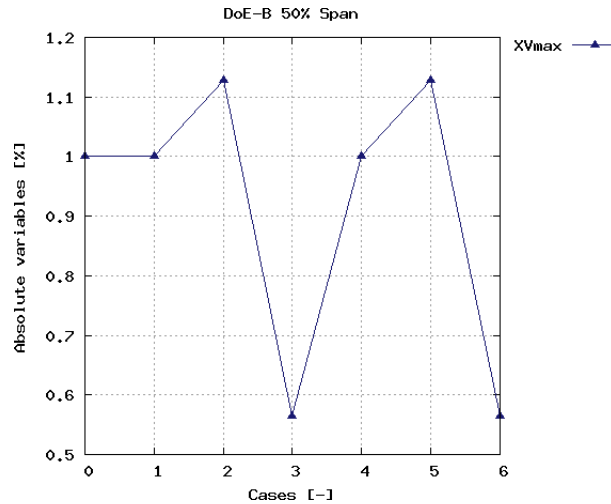


Figure 9.8: DoE-B, absolute variables of the XV_{max} position for the *Volvane G3D Euler* and *Volsol ++*, using the *wf rk - ϵ* model. The cases are evaluated at mid-span.

Figure 9.9 shows the absolute variables of the loss coefficient for the solvers. The cases are evaluated in %, at mid-span. Cases 3, 5 and 6 have the largest differences from the reference design, of about $> 0.3\%$. Cases 1, 2 and 4 have a difference of about 0.05%. Cases 1 and 2 have changed mass-flow while Case 4 has decreased swirl angle. As a conclusion of the analysis, the *Volvane G3D Euler* solver has difficulties in predicting accurate flow results if the boundary condition is changed by an increased swirl angle, or a decreased swirl angle together with increased mass-flow. These conditions cause separations in the RANS-solver and therefore the *G3D Euler*

solver will experience the same difficulties in the prediction. A decreased swirl angle or increased mass-flow only, does affect the flow results but not the solver differences between *Volvane G3D Euler* and *Volsol ++*. The *Volvane G3D Euler* is considered to be robust.

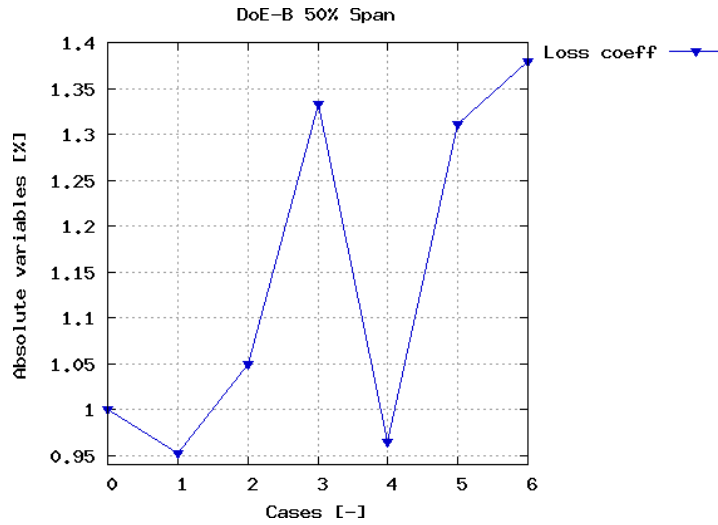


Figure 9.9: *DoE-B*, absolute variables of the loss coefficient for the *Volvane G3D Euler* and *Volsol ++*, using the *wf rκ - ε* model. The cases are evaluated at mid-span.

The diffusion factor differences between the cases are shown in Figure 9.10. All the cases follow the same trend. On 50%-span, the average value of the the difference is about 3%. The solver variances are spread out in the range between $+0.05^\circ$ to -0.08° , which is a total amount of about 1.5° . Case 3 with the increased swirl but with no changes in mass-flow has the largest diffusion factor difference, compared with the other cases. Case 4 has decreased swirl and a large diffusion factor difference, but not as major as for Cases 3 and 5, the ones with increased swirl angle. If the swirl angle is changed together with increased mass-flow (Cases 5 and 6), there is a solver difference. Case 3 has increased swirl only and differs remarkably from the other cases. Changes in mass-flow will always affect the diffusion factor. The *Volvane G3D Euler* solver has difficulties in predicting an accurate diffusion factor if the swirl is increased without any influences in changes of mass-flow.

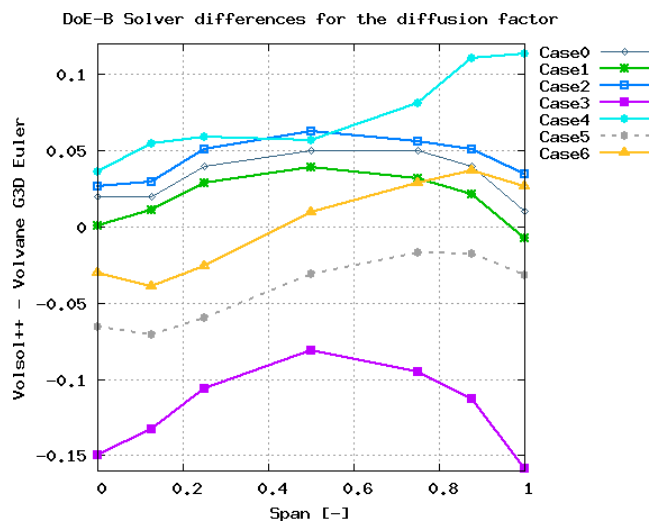


Figure 9.10: The diffusion factor difference in the cases from *DoE-B*, evaluated at mid-span.

Figure 9.11 shows the flow results of outlet swirl angle. All the cases follow a general trend. On 50%-span, -2° is the average difference between the cases. Cases 3 and 5 (the ones with increased swirl), have the largest distinctness, especially near 10%-span. At 12.5%-span, the difference is located between -2.5° to -5.7° . Case 5 (the one with increased swirl and increased mass-flow), contribute to the larger distinctness. The largest

differences are located in the region of 12.5%-span, that is the vane location where the highest load is placed. In most cases, the location of the smallest swirl angle difference is in the region of the shroud. Cases 3 and 5 (with the increased swirl), have the largest difference of about 2° . As a conclusion, all cases follow the same flow pattern. As previously shown, the outlet swirl angle error is about 2.5° for *Volsol++* using wall functions. Thus the *Volvane G3D Euler* solver predicts the swirl angle satisfactorily.

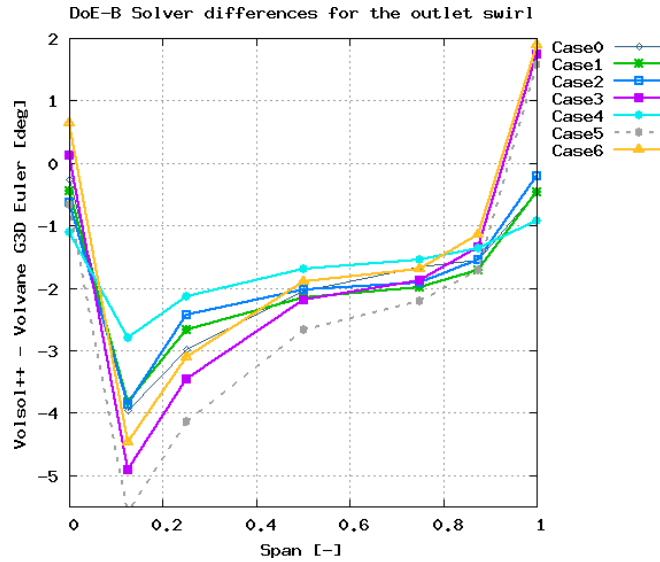


Figure 9.11: The outlet swirl angle difference in the cases from DoE-B, evaluated at mid-span.

9.3 DoE-C, camber line modifications

DoE-C was set up in the *Volvane 2.5.0 beta* version and analyzed with the *G3D Euler* solver in *Volvane 2.5.0 beta* and in *Volsol++* with the *wf r κ - ϵ* model. The following parameters are changed: LE and TE camber line angle, d/ds and d^2/ds^2 of the LE camber line angle. The LE camber line angle is changed $\pm 3^\circ$ and the TE camber line angle $\pm 2^\circ$. To modify the design, the blade load has been traded through the camber line. Sixteen different cases have been created and analyzed using the 2nd order polynomial FCCD model. All face points are excluded. The cases are shown in Table 9.3.

Case	LE($^{\circ}$)	TE($^{\circ}$)	LE d/ds	LE d2/ds2
0	0	0	0	0
1	-3	-2	-0.15	-2
2	-3	-2	-0.15	+2
3	-3	-2	+0.15	-2
4	-3	-2	+0.15	+2
5	-3	+2	-0.15	-2
6	-3	+2	-0.15	+2
7	-3	+2	+0.15	-2
8	-3	+2	+0.15	+2
9	+3	-2	-0.15	-2
10	+3	-2	-0.15	+2
11	+3	-2	+0.15	-2
12	+3	-2	+0.15	+2
13	+3	+2	-0.15	-2
14	+3	+2	-0.15	+2
15	+3	+2	+0.15	-2
16	+3	+2	+0.15	+2

Table 9.3: DoE-C design cases.

The differences in the XVmax positions between *Volsol ++* using the *wf r κ - ϵ* model and the *Volvane G3D Euler* solver, in absolute variables are shown in Figure 9.12. The different cases are evaluated at mid-span. From the reference design, Cases 1 and 2 have the largest difference of about 5%. All the parameters are decreased, apart from the second derivative of Case 2. Cases 3 and 4 have differences of 0.7% approximately. Analogous with Cases 1 and 2, the LE and TE have decreased parameters but the first derivatives of LE are increased. Cases 5, 6 and 7 have differences of 3% approximately. The cases have decreased LE and increased TE. Cases 9 to 12 have increased LE and decreased TE. Cases 10, 11 and 12 are located closest to the reference design, with variances < 0.2%. In the latter case, the first and second derivatives of LE change in positive directions. Case 12 is in good agreement with the reference design. Case 9 has a difference of 2.4% and the derivatives of LE change in negative directions. The distinctions between Cases 9 and 12 indicates that the *Volvane G3D Euler* solver has a minor difficulty to predict the XVmax position when the LE derivatives are changed in negative directions, simultaneously. Cases 13 to 16 have differences between 0.7% and 1.8% approximately.

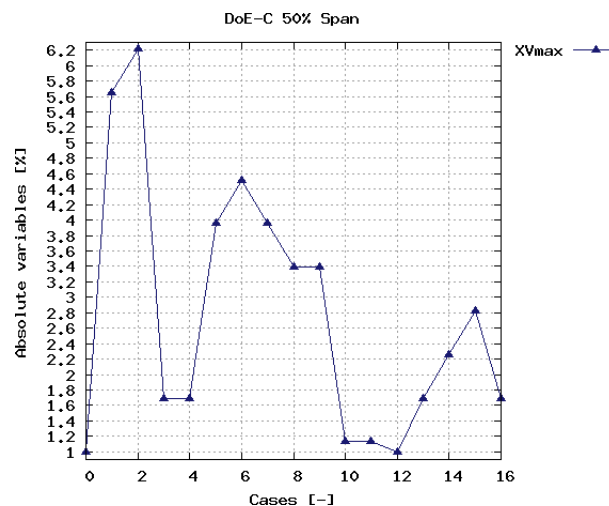


Figure 9.12: *DoE-C*, absolute variables of the XVmax position for the *Volvane G3D Euler* and *Volsol ++*, using the *wf r κ - ϵ* model. The cases are evaluated at mid-span.

Figure 9.13 shows the absolute variables of the loss coefficient between the solvers. The cases are evaluated in % at mid-span. Cases 1 and 4 have decreased LE and TE edges in common. Case 1 is located furthest

away from the reference design, 0.65% approximately while Case 4 is identical with the reference design. The distinctions between those cases are the derivatives of the LE. In Case 1 the derivatives change in negative directions while in Case 4, they change in positive directions. In accordance with the analysis of the XVmas position, the *Volvane G3D Euler* solver has a minor difficulty to predict the loss coefficient when the LE derivatives change in negative directions, simultaneously. This thesis is exclusively an indicator, since it is not valid for all the cases in DoE-C.

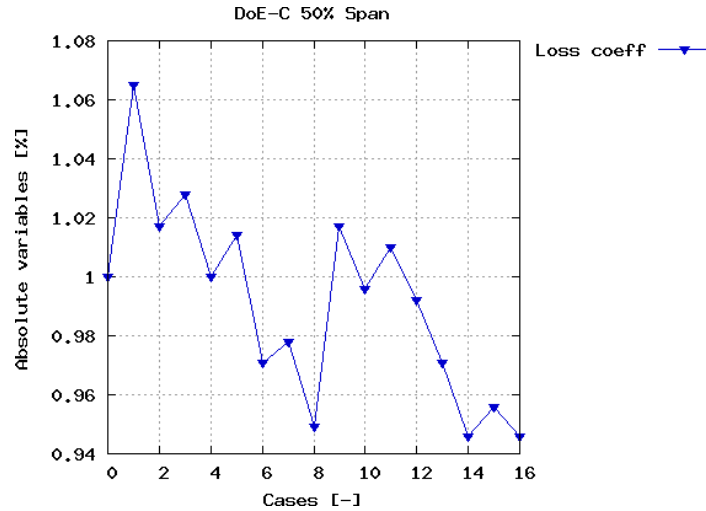


Figure 9.13: DoE-C, absolute variables of the loss coefficient for the *Volvane G3D Euler* and *Volsol ++*, using the $wf r\kappa - \epsilon$ model. The cases are evaluated at mid-span.

The analysis of the diffusion factor is shown in Figure 9.14. All the cases follow the same trend. At the hub and at the shroud, the diffusion factor differences between the solvers for the cases are close to zero. At mid-span, the distinctions are about 0.05 and the average value of all the cases is 13%. Case 16 has the peak while the reference design has the smallest value. The *Volvane G3D Euler* solver predicts the diffusion factor in a satisfactory way.

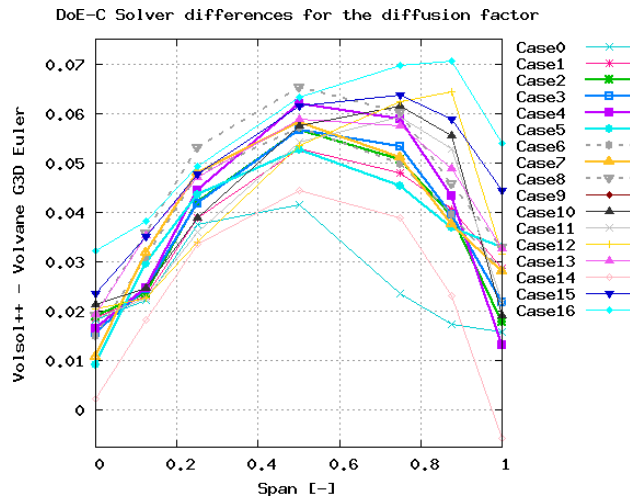


Figure 9.14: The diffusion factor difference in the cases from DoE-C, evaluated at mid-span.

The results of the solver differences for the outlet swirl angle is shown in Figure 9.15. Again, all the cases follow the same trend. At the mid-span, the distinctions are located between -4° and 0° . The average value is about -1.8° , but keep in mind the 2.5° outlet swirl angle difference by wall functions. This phenomenon does not exist in the *Volvane G3D Euler* solver, which in this case is considered to be accurate. At 12.5%-span,

the largest outlet swirl angle distinctions are located with values between -2° to -6° . For most of the cases, the minimum is located at the shroud with a swirl angle variance between -2° to $+2^\circ$. When no separation is present, the *Volvane G3D Euler* solver predicts the swirl sufficiently.

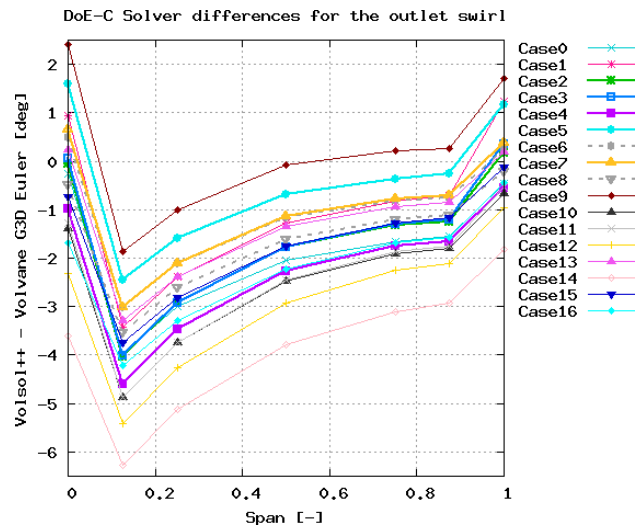


Figure 9.15: The outlet swirl angle difference in the cases from DoE-C, evaluated at mid-span.

9.4 Part 1. Summary & Conclusions

The following results and conclusions were found from the investigation and analysis in the first part of this thesis:

- Suggestions for new features in *Volvane* resulted in updates of new versions of *Volvane 2.5.0 beta* and *Volvane 2.6.3 alpha*. *Volvane 2.5.0 beta* has the ability to add boundary condition profiles into the solver. The diffusion factor was modified by changing the way the exit velocity was calculated. *Volvane 2.6.3 alpha* is provided with a new DoE-section.
- Wall functions analysis in *Volsol ++* showed a 2.5° outlet swirl angle difference from low Reynolds flows, which should be taken into account when analyzing simulations.
- The diffusion factor differences in the *Volvane G3D Euler* solver are between 3% to 13% relative *Volsol ++* using the wall functions mesh. This fact is based on an average value from all DoEs evaluated at the mid-span.
- The loss estimations from the *Volvane G3D Euler* solver are about 35% of the loss estimations from the RANS-solver. This fact should be taken into account when using the *Volvane G3D Euler* solver.
- For all the DoEs, on mid-span the average value of the outlet swirl angle difference is about 2° , which implies an acceptable swirl prediction.
- The *Volvane G3D Euler* solver has more difficulties in predicting changes in lean compared with changes in sweep. The solver is more able to predict a positive sweep than negative sweep.
- If the inlet swirl angle is increased, the *Volvane G3D Euler* solver has difficulties in predicting the diffusion factor.
- If both the boundary conditions in terms of swirl and mass flow are changed, the *Volvane G3D Euler* solver will have difficulties in predicting the outlet swirl angle.
- Overall, the *Volvane G3D Euler* solver and the RANS-solver are in good agreement.

10 Part 2. Design process rationalization

The aim of the design process rationalization is to find correlations between different design and output parameters. The correlations can be used to try to reduce the initial number of design parameters used in the *Volvane* design tool.

modeFRONTIER is a statistical analysis tool used for this investigation. The DoEs from section 9 are applied to create response surfaces. For all the output parameters, second order polynomial response surfaces are used. A Monte Carlo-like simulation approach is used for the statistical analysis. From *modeFRONTIER*, CDF charts and parameter correlations for the selected parameters are obtained. The correlations can be used as measures of how different parameters are related, and to estimate the power of the relations between the design and evaluation parameters. In the following correlation charts, the value 1 on the y-axis corresponds to a correlation of 100%. Values under 0.2 or 20% are neglected. In Part 2, all design parameter changes are applied to each vane section.

DoE-D and DoE-E are the two new DoEs, set up and analyzed in *Volvane* 2.6.3 *alpha*. The latter is similar to former, but the parameter bounds are increased. The results of the analysis in Part 1 showed acceptable agreement between the *Volvane G3D Euler* solver and *Volsol ++*. Therefore, only *Volvane* is used to create DoE-D and DoE-E. According to the previous results, RANS-solver simulations are not required in this part of the design process rationalization.

10.1 DoE-A

In DoE-A the lean and sweep parameters are changed.

Figure 10.1 shows how strongly correlated the outlet swirl is with different parameters from *Volsol ++* and simulating with the *wf r κ - ϵ* solver and from *Volvane* 2.5.0 *beta* using the *G3D Euler* solver. From both the solvers are lean and sweep the strongest correlated parameters. In *Volsol ++*, there is a larger correlation variance between lean and sweep than in *Volvane G3D Euler* solver. One of these reasons may be explained by the existence of boundary layer development in *Volsol ++* which does not exist in the *Volvane G3D Euler* solver. In *Volsol ++*, the correlation factor between outlet swirl and lean is about 80%, compared to outlet swirl and sweep with a factor of about 20%. In *Volvane*, the correlation between outlet swirl and lean is approximately 55%, while the correlation between sweep and swirl is about 45%.

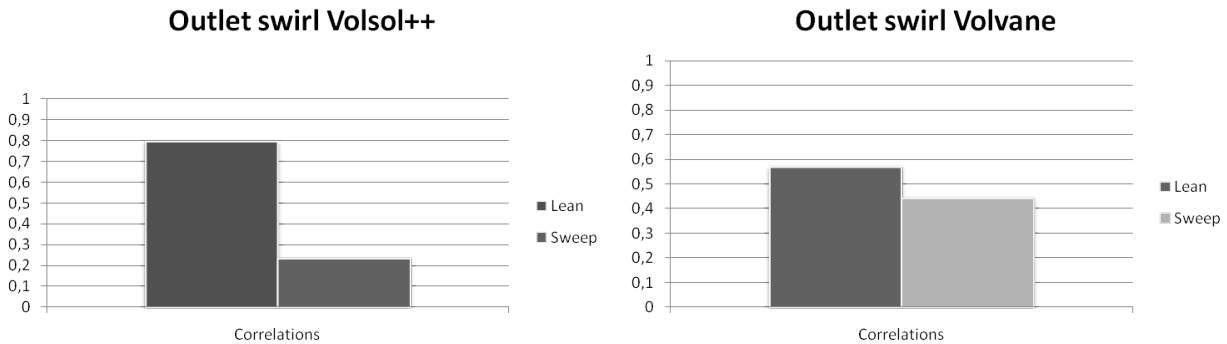


Figure 10.1: Correlation parameters for outlet swirl in *Volsol ++*, using the *wf r κ - ϵ* solver and with *Volvane* using the *G3D Euler* solver.

Shown in Figure 10.2, the strongest correlated parameter with the loss estimation from the solvers are in acceptable agreement. For both the solvers, lean is the strongest correlated parameter of about 85%.

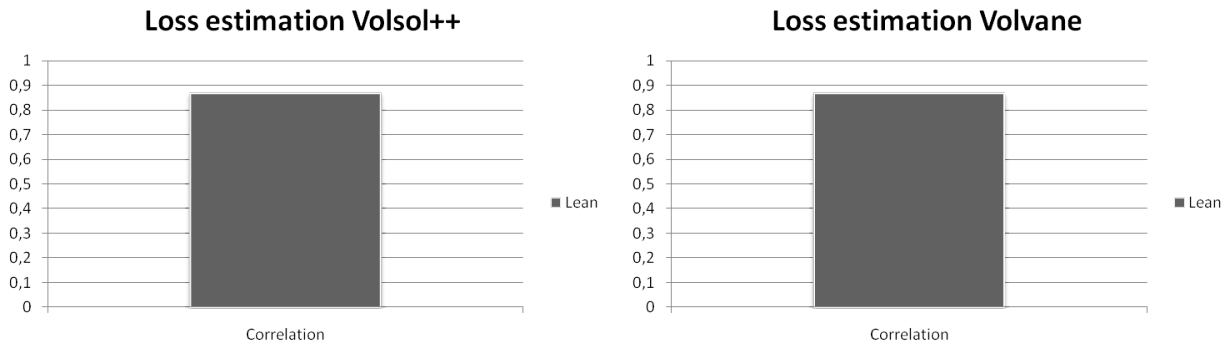


Figure 10.2: Correlation parameters for the loss coefficient estimation in *Volsol++*, using the *wf rκ - ε* solver and with *Volvane* using the *G3D Euler* solver.

The correlation with the diffusion factor from *Volsol++* is shown in Figure 10.3. Lean is the strongest correlated parameter. The strength of the correlation is approximately 85%.

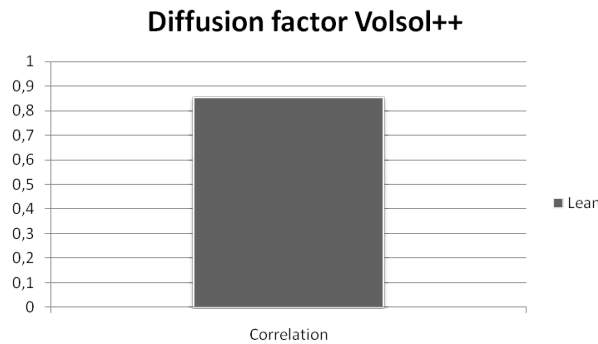


Figure 10.3: The correlation between the diffusion factor and the lean simulated in *Volsol++* with the *wf rκ - ε* solver.

10.2 DoE-C

In DoE-C, the following parameters are changed: LE camber angle, TE camber angle and the first and second derivatives of the LE camber angle. This is the full set of camber line parameters commonly used in the turbine rear frame and outlet guide vane design.

Figure 10.4 shows the strongest correlated parameters of the outlet the swirl from *Volsol++* using the *wf rκ - ε* model and the *Volvane G3D Euler* solver. For the solvers there are good correlations between the outlet swirl and the TE camber angle. *Volsol++* has influences from other parameters (LE camber angle and the first and second derivatives of the LE camber angle).

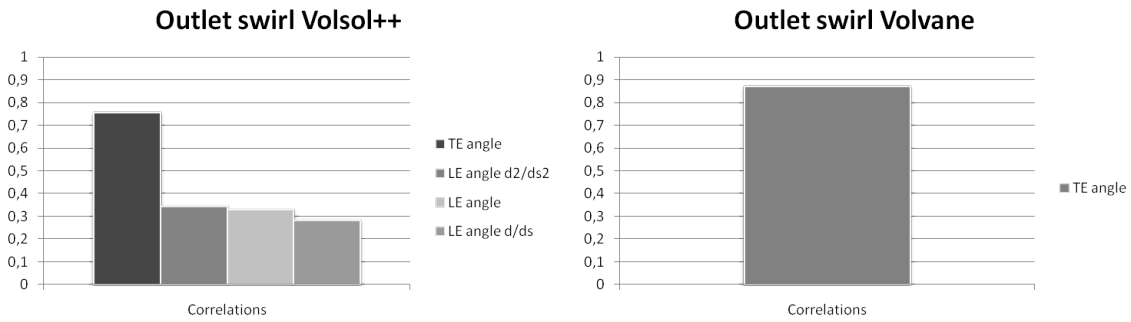


Figure 10.4: Correlation parameters for outlet swirl in *Volsol++*, using the *wf r κ - ϵ* solver and with *Volvane* using the *G3D Euler* solver.

The strongest correlated parameters with the loss coefficient are shown in Figure 10.5. The TE camber angle has the largest influence on the loss estimation in *Volsol++*, with a correlation of about 85%. The loss estimation in *Volsol++* is a result of boundary layer development, secondary flow loss and wake mixing loss. The LE first and second derivatives have only minor influences on the loss coefficient with a strength of 40% and 20%, respectively. In *Volsol++*, there is no correlation between the loss coefficient and the LE camber angle. In the *Volvane G3D Euler* solver, the LE camber angle is the strongest correlated parameter, of about 80%. This fact can be compared with *Volsol++* where the TE is the strongest correlated parameter. Since the loss estimation in the *Volvane G3D Euler* solver is about 35% of the total amount of losses in *Volsol++*, large differences are expected. In the *Volvane G3D Euler* solver, the correlation with the TE camber angle is about 40% which is half the size of the correlation of the LE camber angle. Again, the reason is explained by the lack of secondary flow in the *Volvane G3D Euler* solver. The first derivative of the LE camber angle has only a weak correlation with the loss estimation.

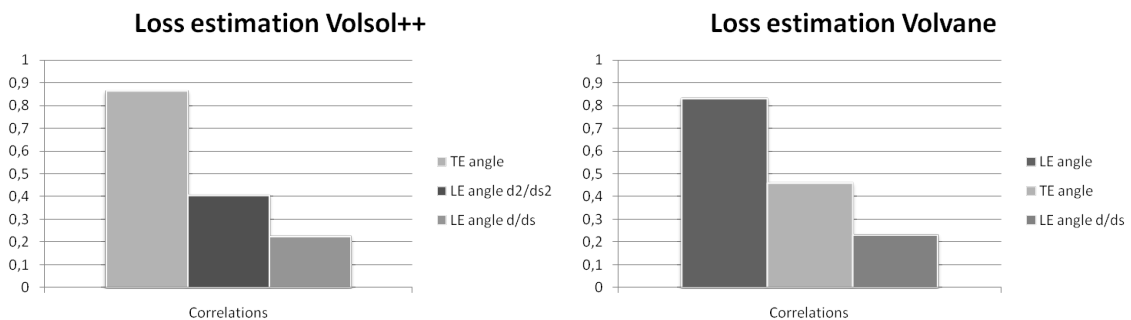


Figure 10.5: Correlation parameters for the loss coefficient estimation in *Volsol++*, using the *wf r κ - ϵ* solver and with *Volvane* using the *G3D Euler* solver.

The strongest correlated parameters with the diffusion factor are shown in Figure 10.6. Both the solvers are in good agreement with the second derivative of the LE camber angle as the strongest correlated parameter.

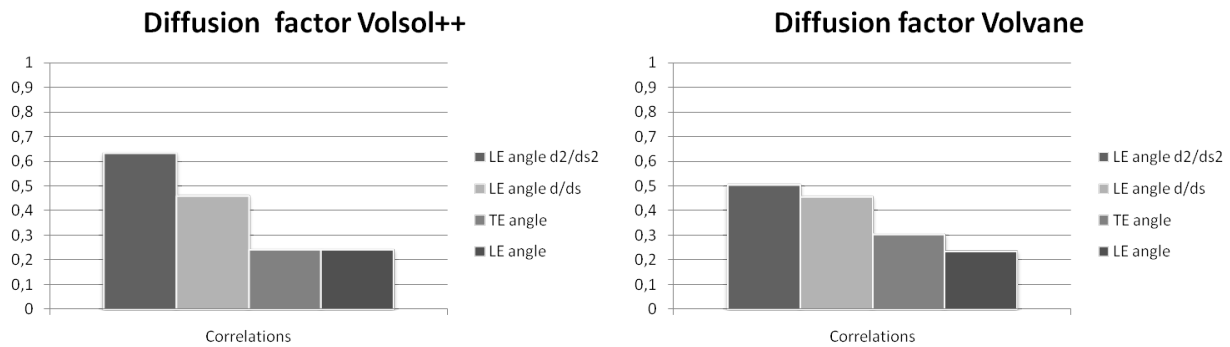


Figure 10.6: Correlation parameters for the diffusion factor in Volsol ++, using the $wf r\kappa - \epsilon$ solver and with Volvane using the G3D Euler solver.

The analysis of DoE-C indicates how the parameters are correlated in the solvers and the differences between them. During vane design, for both the solvers, the correlation with the diffusion factor are in good agreement.

10.3 DoE-D

This DoE-D was created and computed in Volvane 2.6.3 *alpha*, since the previous step in the investigation implied Volvane G3D Euler solver to be sufficiently accurate in terms of vane design. No RANS-solver simulations were performed. In this DoE, the strongest correlated and interesting parameters from DoE-C were kept and additionally the thickness distribution was investigated. A total number of 80 cases were created and the modified parameters are shown in Table 10.1.

Parameter	Variations (\pm)
LE camber angle	4°
TE camber angle	2°
LE camber angle d/ds	0.2°
LE camber angle d^2/ds^2	2°
Max thickness	2.5mm
Max thickness location	5%
Front thickness modification	3%
Rear thickness modification	5%
Rear thickness modification locality	0.2
TE wedge angle modification	3°

Table 10.1: DoE-D design parameters.

In DoE-D, the following correlations were found: The TE wedge angle modification was not correlated to any evaluated output parameter. The front thickness modification was only slightly correlated with the mass-flow. The max thickness location was only correlated to Vmax and the diffusion factor.

From Volvane, the correlated parameters with the outlet swirl and the mass-flow are shown in Figure 10.7. As expected, the TE camber angle has the largest correlation with the outlet swirl angle, (see the previous DoE-C). The mass-flow has a correlation with the maximum thickness location of about 60%, followed by the LE camber angle and the front thickness modification, with correlation values of about 40%. These values are considered weak correlations.

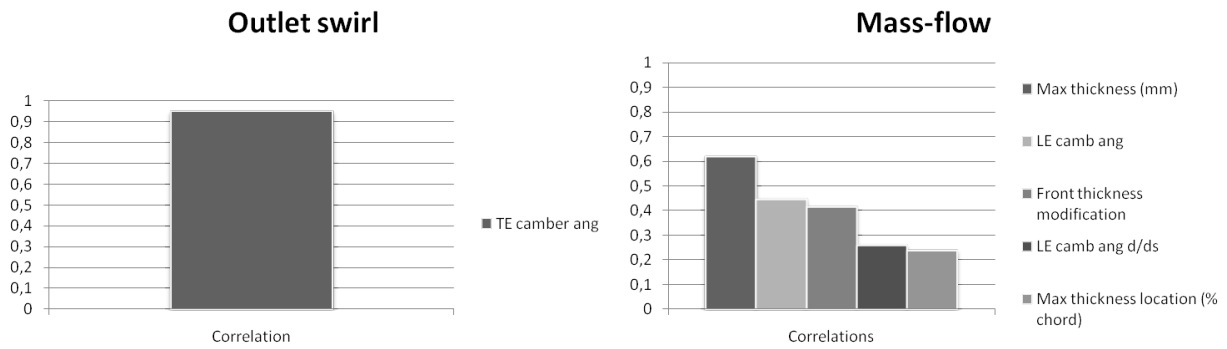


Figure 10.7: Correlation parameters for outlet and mass-flow from the Volvane G3D Euler solver.

Correlations with the loss estimation and the diffusion factor is shown in Figure 10.8. The loss coefficient has a strong correlation with the maximum thickness of the chord (70%), followed by the leading edge camber angle of 55%. There is a large uncertainty of the loss estimation in *Volvane*, see Part 1. The diffusion factor is mostly influenced by the maximum thickness location, (% of chord), with a correlation value of almost 60%. This is not considered a strong correlation. A strong correlation should be located above 70%. The second derivative of the leading edge camber angle has a weak correlation with a diffusion factor of about 40%.

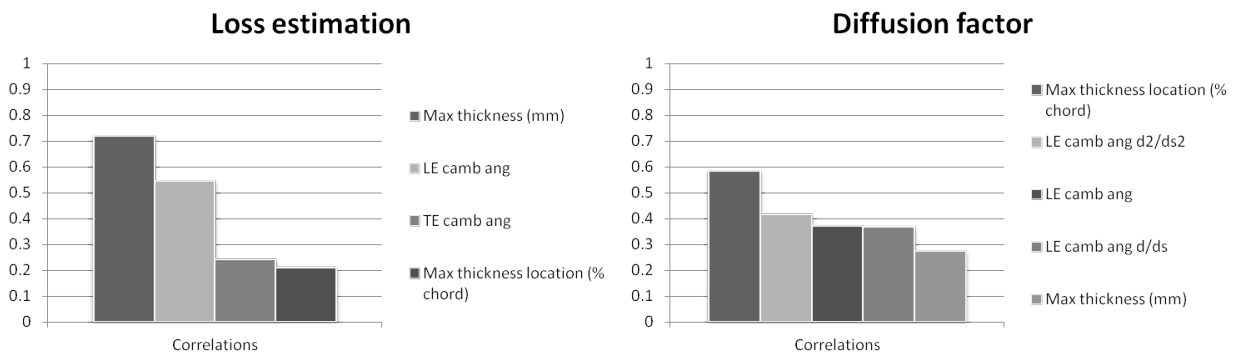


Figure 10.8: Correlation parameters for the loss coefficient and the diffusion factor in Volvane.

Correlations from *Volvane* with V_{max} and XV_{max} are shown in Figure 10.9. Analogous with the diffusion factor, the correlation between V_{max} and the maximum thickness location is around 60%. The second largest correlation is the derivative of the LE camber angle of about 40%. The V_{max} axial position has a correlation with the leading edge camber angle of 60%.

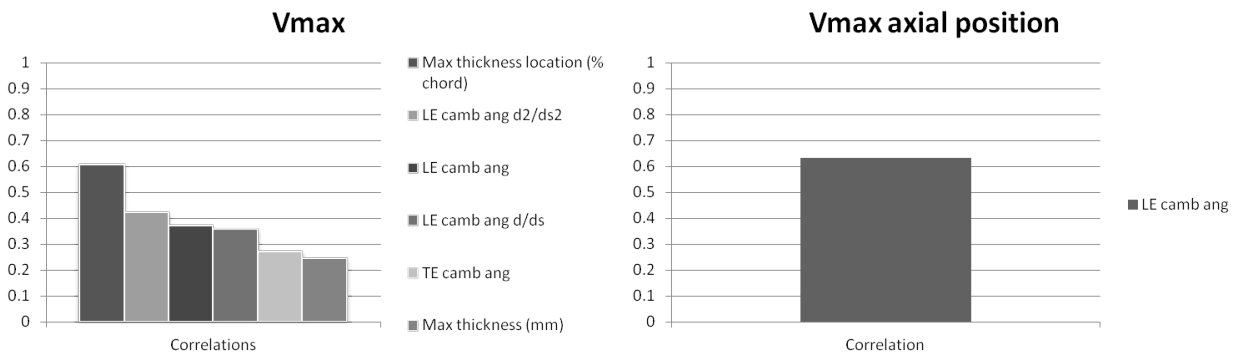


Figure 10.9: Correlation parameters for V_{max} and V_{max} axial position in the Volvane G3D Euler solver.

Shown in Figure 10.10, there is only a weak correlation between the deviation angle and the trailing edge

camber angle (about 55%). The leading edge camber angle and the leading edge camber derivatives have a weak correlation in a range between 40%-48%.

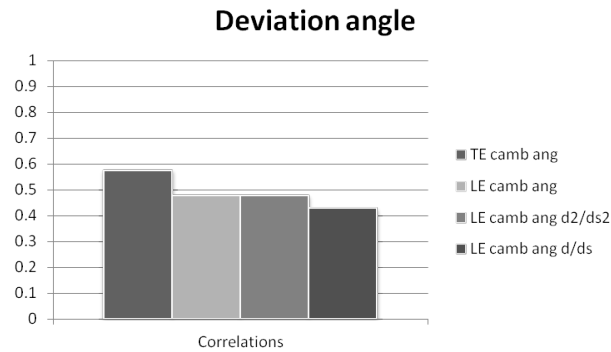


Figure 10.10: Correlation parameters for the deviation angle in *Volvane G3D Euler solver*.

A conclusion of DoE-D, the most important parameter for the outlet swirl angle is the TE camber angle. The loss coefficient has the maximum thickness and the mass-flow as the strongest correlated parameters. The diffusion factor and the Vmax have a strong connection with the max thickness location (% of chord). For the Vmax axial position, the LE camber angle is the most important parameter.

10.4 DoE-E

In order to accomplish further investigations, DoE-E is similar to DoE-D but for some parameters, the limits of the bounds have been duplicated. The DoE was created and simulated in *Volvane2.6.3alpha*. A total number of 80 cases were created. The modified parameters are shown in Table 10.2:

Parameter	Variations (\pm)
LE camber angle	8°
TE camber angle	4°
LE camber angle d/ds	0.05°
Max thickness	5mm
Max thickness location	10%
Rear thickness modification locality	0.3
TE wedge angle modification	5°

Table 10.2: DoE-E design parameters.

In the DoE-E, the LE and TE camber angles and the maximum thicknesses of the vane have duplicated limits compared with the previous DoE-D. From DoE-D the following parameter boundaries remains unchanged: The second derivative of the LE camber angle (d^2/ds^2), front and rear thickness modification. Compared to DoE-D, the TE wedge angle is increased with 2° and the locally rear thickness modification with 0.1°. The first derivative of the LE camber angle is decreased with 0.15°.

Correlations with the outlet swirl angle and the mass-flow are shown in Figure 10.11. The correlations for the outlet swirl angle are in similarity with the previous DoE-D. The TE camber angle is the strongest correlated parameter. The mass-flow correlations are similar to DoE-D, with the maximum thickness of the chord of about 60%. The LE camber angle has a correlation strength of 40% only.

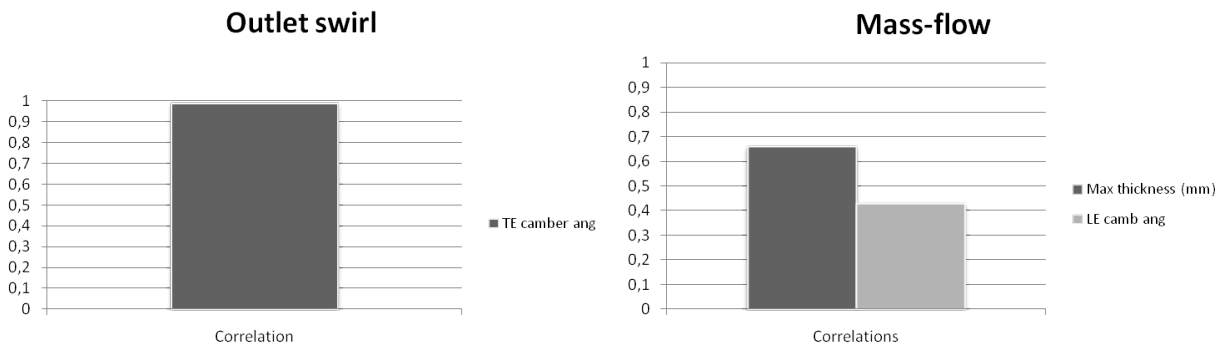


Figure 10.11: Correlation parameters in Volvane G3D Euler solver for outlet swirl and mass-flow.

Results for the loss estimation and the diffusion factor are shown in Figure 10.12. The correlations for the loss coefficient are similar with DoE-D. The maximum location of the chord is the strongest correlated parameter, followed by the LE camber angle. Keep in mind, the poor prediction of the loss estimation by the *Volvane G3D Euler* solver compared with RANS-solvers produces inaccurate correlations. The diffusion factor has a correlation with the max thickness location of chord with a strength of around 50%, compared with the correlation from DoE-D, (nearly 60%). From DoE-D and DoE-E, the correlations of the diffusion factor are considered weak.

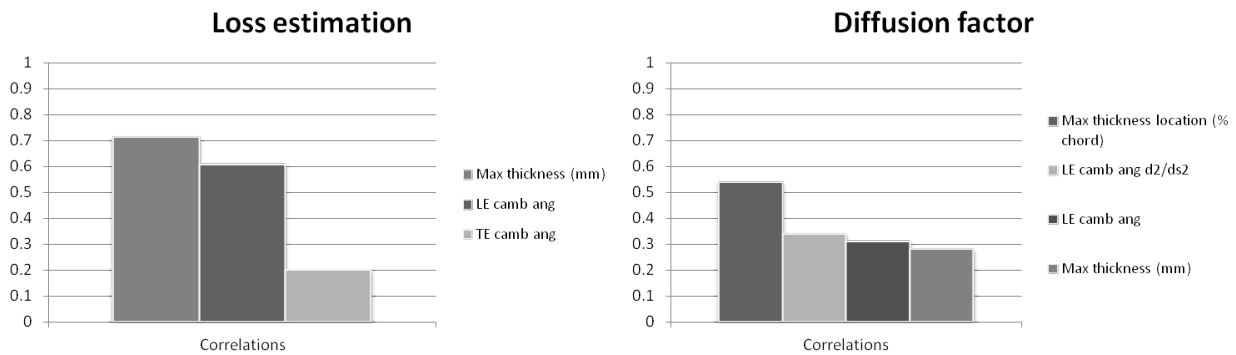


Figure 10.12: Correlation parameters for the loss estimation and the diffusion in Volvane G3D Euler solver.

Figure 10.13 shows the correlations for V_{max} and XV_{max} . The correlations between V_{max} and the maximum thickness location, (% of chord) are about 58%. This is slightly less than DoE-D. The V_{max} axial position is strongest correlated with LE camber angle, with a value of above 70%. This is nearly 10% stronger than for the correlation in DoE-D.

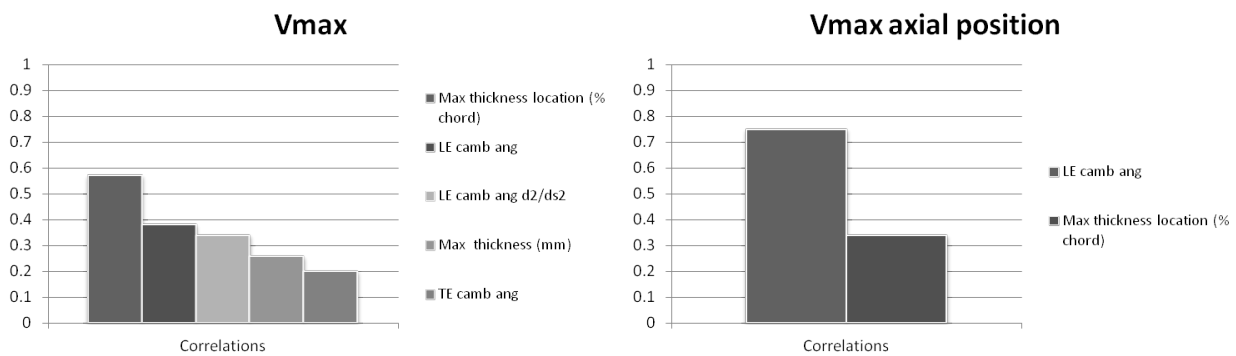


Figure 10.13: Correlation parameters for V_{max} and V_{max} axial position in Volvane G3D Euler solver.

The deviation angle is shown in Figure 10.14. There is a strong correlation with the TE camber angle, of about 80%. Compared with DoE-D, this value is about 22% higher.

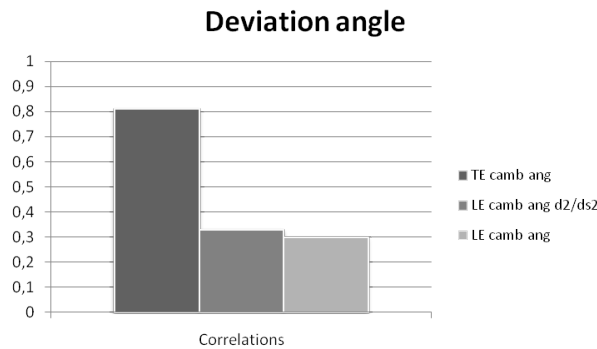


Figure 10.14: Correlation parameters for deviation angle in *Volvane G3D Euler solver*.

The results of DoE-E are similar to DoE-D. As a conclusion, when the limits of the boundaries are duplicated, the parameters are generally not stronger correlated, which is good since one intention of the DoE-E study was to check the robustness of the method.

10.5 Part 2. Summary & Conclusions

Table 10.3 summarizes the strongest correlations from all the DoEs of the *Volvane G3D Euler solver*. If the design parameters in the table are changed, the corresponding output parameters will be affected. When reading the table, the inaccurate prediction of the loss coefficient by the *Volvane G3D Euler solver* should be taken into account. When the parameter bounds are increased, the correlations are unchanged. For vane design in *Volvane*, the results can be used to reduce the initial number of design parameters. An approach to this issue could be to optimize a design based on the most influenced parameters. The maximum thickness location of the vane can be shifted without affecting the axial position of maximum velocity.

Design parameter	Output parameter
TE camber angle ($^{\circ}$)	Outlet swirl angle & Deviation angle
LE camber angle ($^{\circ}$)	Xvmax & Loss coefficient
Max thickness (mm)	Mass flow & Loss coefficient
Max thickness location (%)	Diffusion factor & Vmax
LE camber angle (d/ds)	Diffusion factor
LE camber angle (d^2/ds^2)	Diffusion factor
Lean	Loss coefficient

Table 10.3: Table of the most important design parameters accomplishes most influences on the output parameters in the *Volvane G3D Euler solver*.

Table 10.4 summarizes DoE-A and DoE-C of *Volsol ++* using the *wf rκ - ε* solver. Only the strongest correlated parameters are taken into account. As shown in the table, a change in design parameter will affect the corresponding output parameter.

Design parameter	Output parameter
TE camber angle ($^{\circ}$)	Outlet swirl angle & Loss coefficient
LE camber angle (d/ds)	Diffusion factor
LE camber angle (d^2/ds^2)	Diffusion factor
Lean	Diffusion factor & Loss coefficient

Table 10.4: Table of the most important design parameters accomplishes influences on the output parameters in *Volsol ++* using the *wf rκ - ε* solver.

11 Future work

Further investigations of design parameters in order to perform parameter reductions are recommended. A RANS analysis of DoE-E could be accomplished. It should be interesting to design a vane using the most important design parameters only. Another future issue is to use the existing response surface methodologies for investigations and improvements of non-conformal handling. The reference design has a fixed gas channel, a suggestion is to allow this gas channel to vary. Some correlations found were weaker or stronger than expected. For instance in DoE-D, the Tmax location for the Vmax axial position and the Tmax for the diffusion factor were surprisingly weak. Further studies of the method for finding correlations are required. Another future proposal is to perform optimization including the most correlated parameters only.

12 Appendix A

12.1 Variance and standard deviation

The following equations are described and discussed by [Geo08]. The ensemble average has roots in independent statistical events and are defined:

$$X = \langle x \rangle \equiv \frac{1}{N} \lim \sum_{n=1}^N x_n \quad (12.1)$$

x_n denotes realizations of a random variable and X is the ensemble average or expected value. Fluctuations about the mean are defined:

$$x' = x - X \quad (12.2)$$

In statistics, is it sometimes interesting to find out how a random variable is distributed about the mean. The average of the fluctuations cannot be a zero variable.

$$\langle x' \rangle = 0 \quad (12.3)$$

but the ensemble average of the square of the fluctuations is a non zero variable and defined as the variance

$$var[x] \equiv \langle (x')^2 \rangle = \langle [x - X]^2 \rangle \quad (12.4)$$

$$= \lim_{N \rightarrow \infty} \frac{1}{N} \sum_{n=1}^N [x_n - X]^2 \quad (12.5)$$

The variance or the ensemble average can never be exactly measured since a measurement requires infinite numbers of ensembles.

The standard deviation is defined:

$$\sigma_s = (var[x])^{1/2} \quad (12.6)$$

and shows how much variation there is from the mean. The standard deviation is low when the variation is close to the mean and gets higher further away from the mean.

Statistical analysis including variance and standard deviation are not used in this thesis, but for every investigated design parameter, their values are set as preparation for possible future issues.

12.2 Probability Density and Cumulative Distribution Functions

Probability density function (PDF)

A probability density function of a random variable describes the relative chance for the random variable to exist at a given point. A histogram is a collection of a number of random variables, divided into a number of windows. The numbers of windows are the range of possible values of the random variables. For each realization, a count is placed in the appropriate window. The number of counts in each window is divided in the total number of realizations. The total sum of the values including all the windows is one. With other words a histogram shows the relative frequency of occurrence of a given value range in a given ensemble. [Geo08]

The following equations and discussion according to [Geo08] reads:

The histogram can be defined as:

$$H_x(c, \Delta c, N) \quad (12.7)$$

where

$$c \leq x \leq c + \Delta c. \quad (12.8)$$

The width of the window is

$$\Delta c \quad (12.9)$$

and N gives the total number of realizations. If N increases as the window-size vanish, the histogram reaches a limiting curve named the Probability Density Function,(PDF).

The PDF may be written:

$$B_x(c) = \lim_{N \rightarrow \infty} H(c, \Delta c, N) / \Delta c \quad (12.10)$$

$$N \rightarrow \infty \quad (12.11)$$

$$\Delta c \rightarrow 0 \quad (12.12)$$

The following properties belong to the probability density function:

The first property reads no negative probabilities and is valid constantly:

$$B_x(c) > 0 \quad (12.13)$$

The second property reads the probability to find realization in an interval around a specific value:

$$Prob\ c < x < c + dc = B_x(c)dc \quad (12.14)$$

The third property states the probability that the realization is less than a certain value:

$$Prob\ c < x = \int_{-\infty}^x B_x(c)dc \quad (12.15)$$

The last property states a realization takes a certain value and that the probability in unity:

$$\int_{-\infty}^{\infty} B_x(x)dx = 1 \quad (12.16)$$

The n th moment reads:

$$\langle x^n \rangle = \int_{-\infty}^{\infty} c^n B_x(c)dc \quad (12.17)$$

and origins from the fact that since

$$B_x(c)dc \quad (12.18)$$

gives the probability of finding a random variable x distributed between the limits of c and $c+dc$. They are the distributional moments computed as an integral including the appropriate power of x over all the possible values [Geo08].

Cumulative distribution function (CDF)

The cumulative distribution function, (CDF) can be defined as [Wei]:

$$F(x) = \text{Prob } X < x = \int_{-\infty}^x B_x(c)dc \quad (12.19)$$

Where X is a random observed variable and x is an arbitrary value. The CDF can be explained as, for a given value x , $F(x)$ is the probability of how the observed value X will not exceed the value of x . The observed value will be located anywhere randomly between 0 and x . For a random variable, the PDF together with the CDF results in a fulfilled description of the probability of the distribution [Wei].

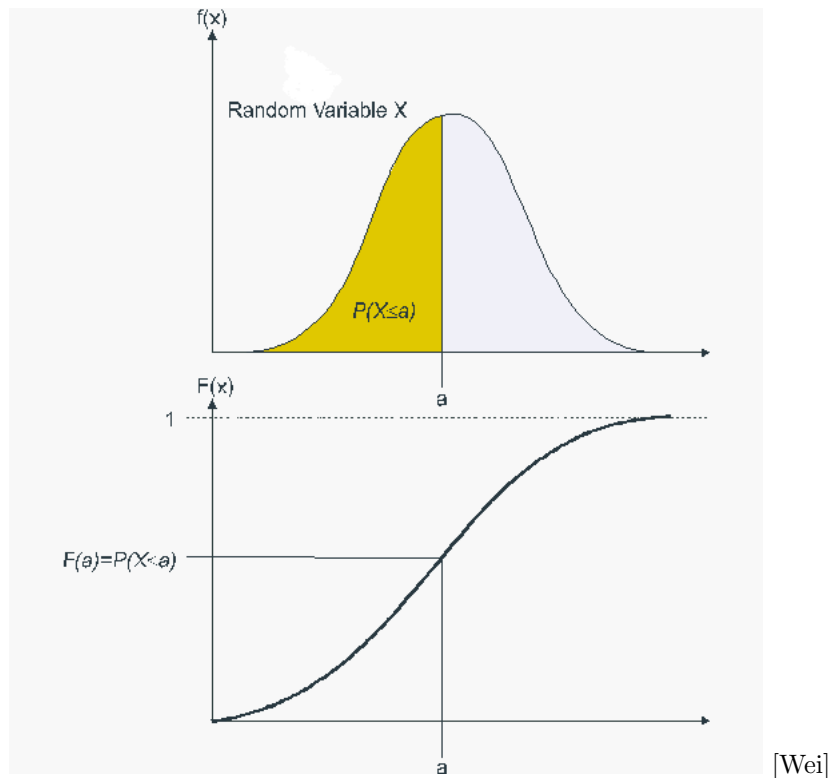


Figure 12.1: The relationship between a PDF and a CDF is shown in the figure. In the upper figure a PDF is shown. X is a random variable and P is the probability that X will reach a as the maximum value. The lower figure shows a CDF, where $F(a)$ is the probability that the maximum value of X is a .

13 Appendix B, CDF charts DoE-A

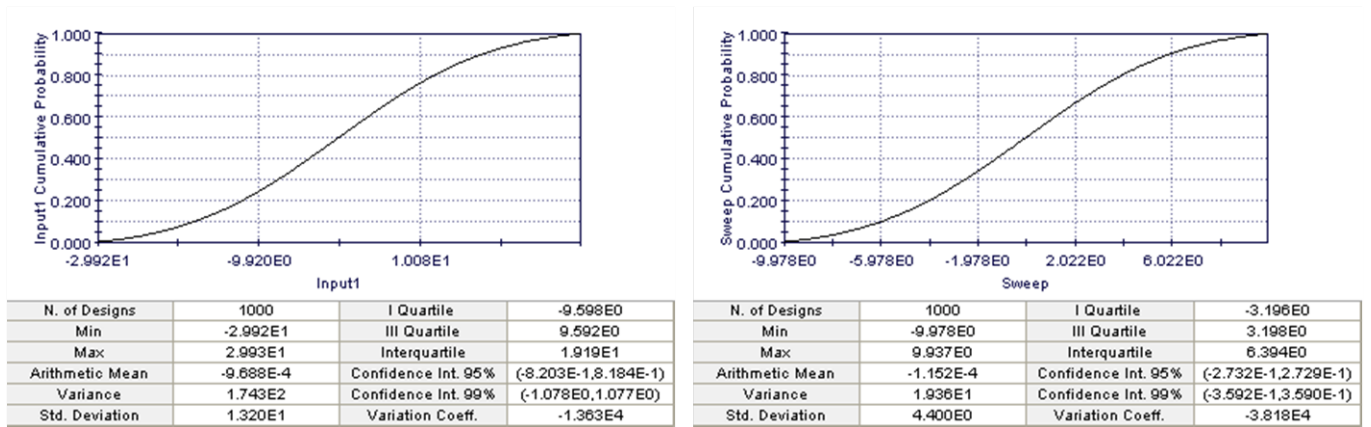


Figure 13.1

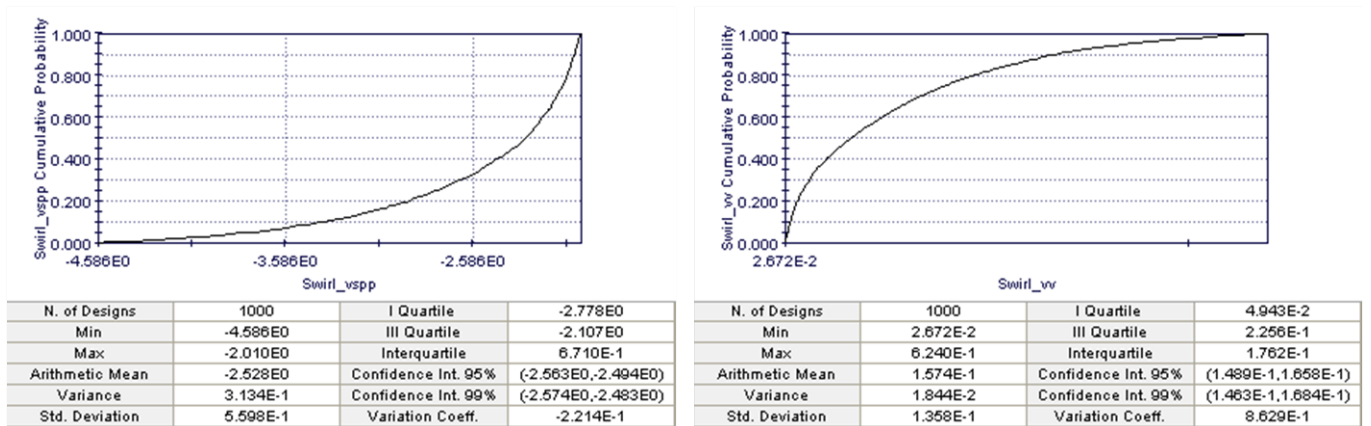


Figure 13.2

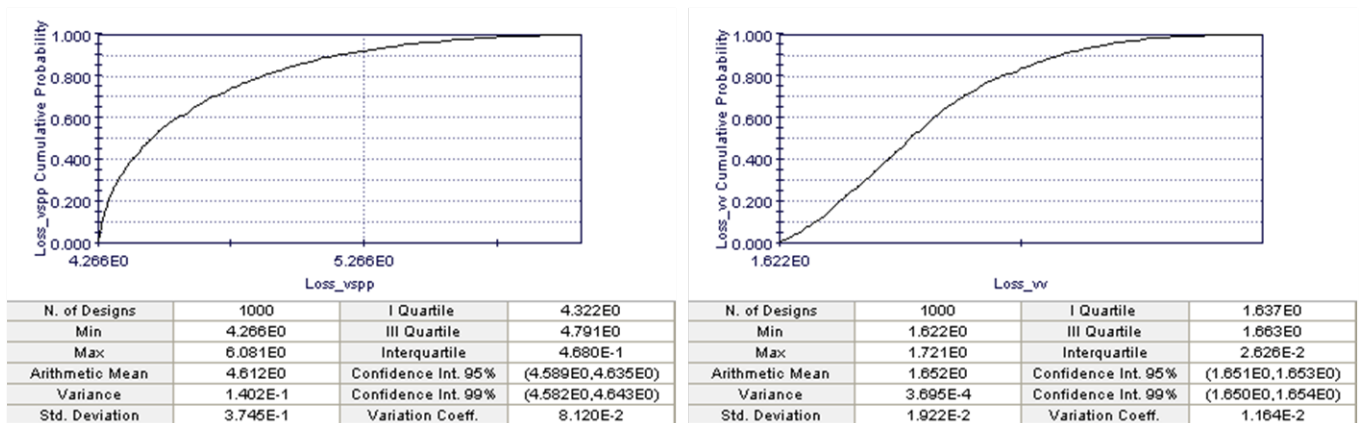


Figure 13.3

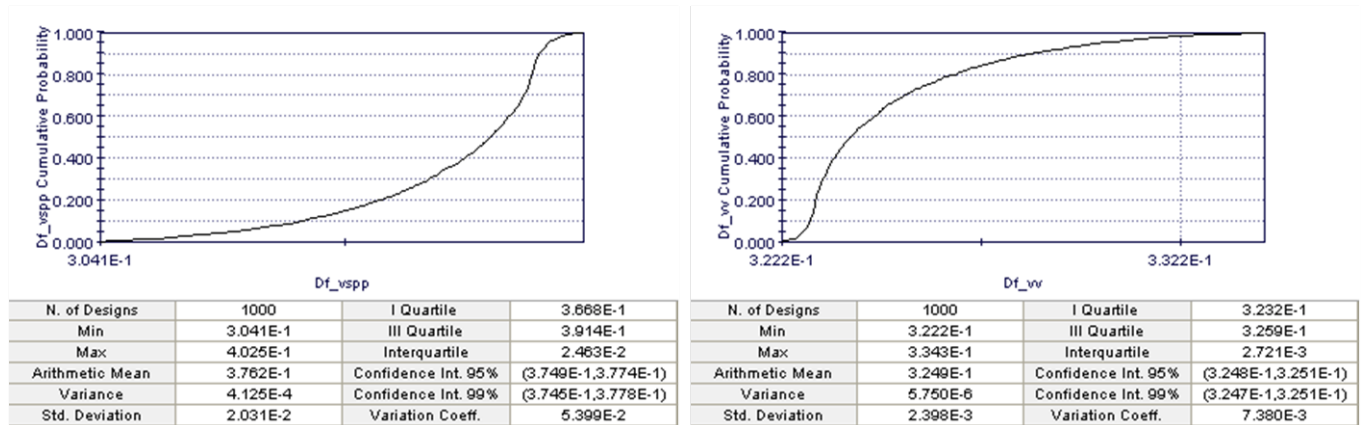


Figure 13.4

14 Appendix C, CDF charts DoE-C

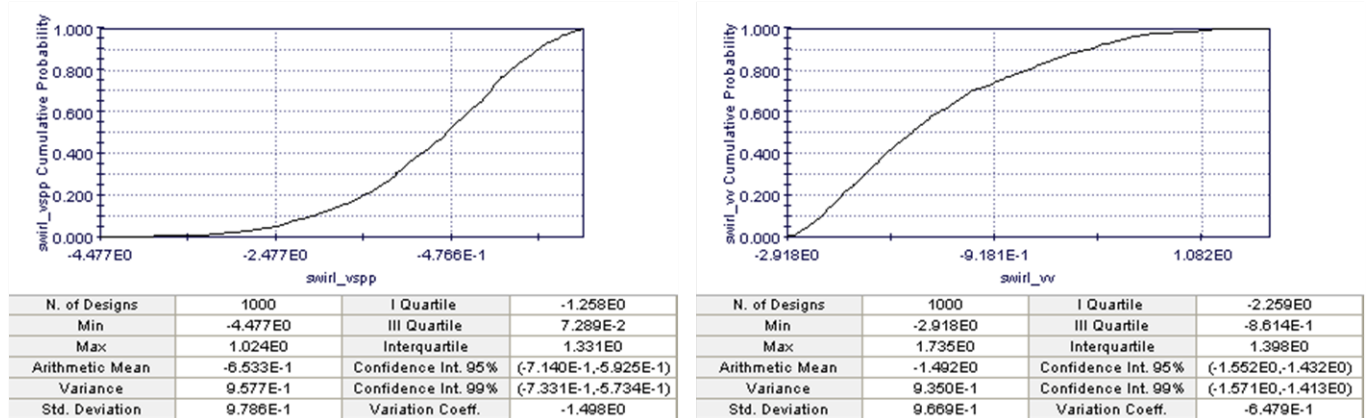


Figure 14.1

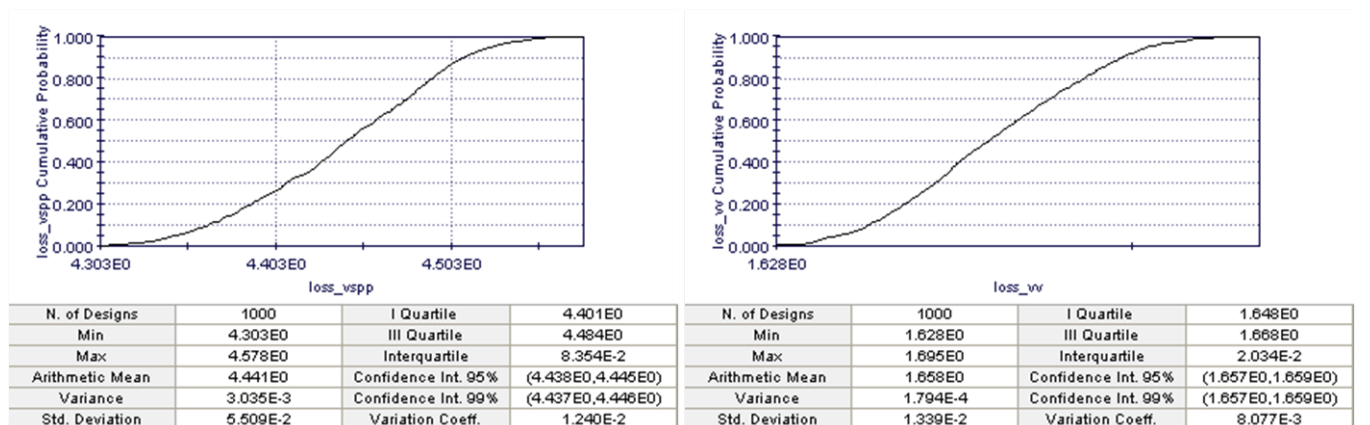


Figure 14.2

15 Appendix D, CDF charts DoE-D

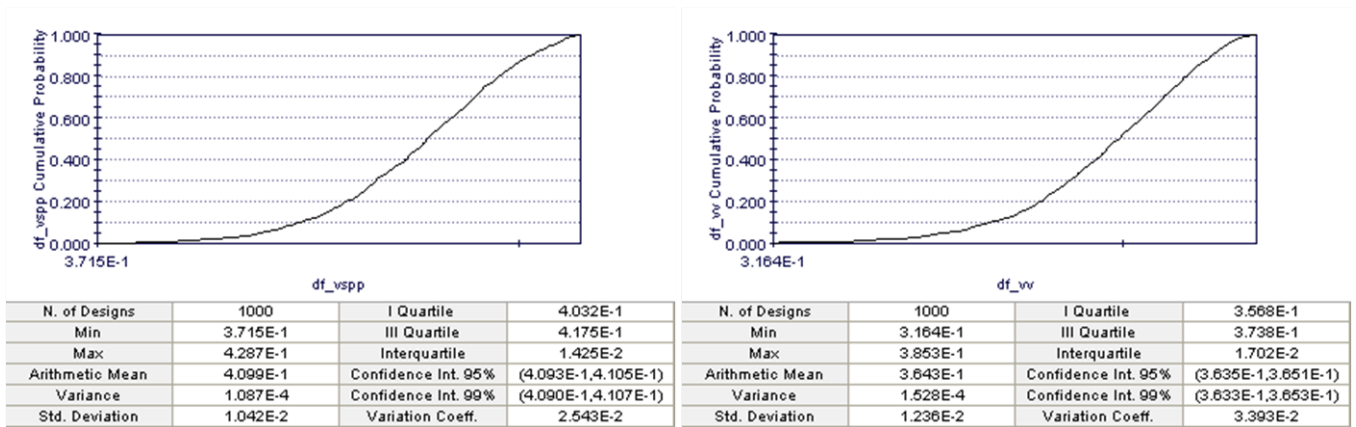


Figure 14.3

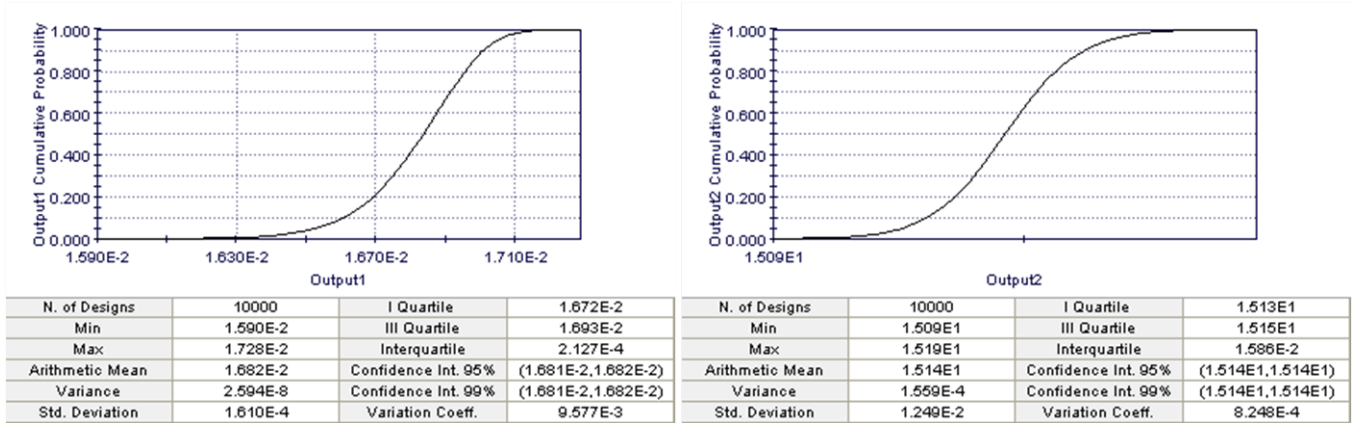


Figure 15.1: At the left side in figure the pcf for the loss estimation is shown and at the right is the pcf over the mass-flow shown.

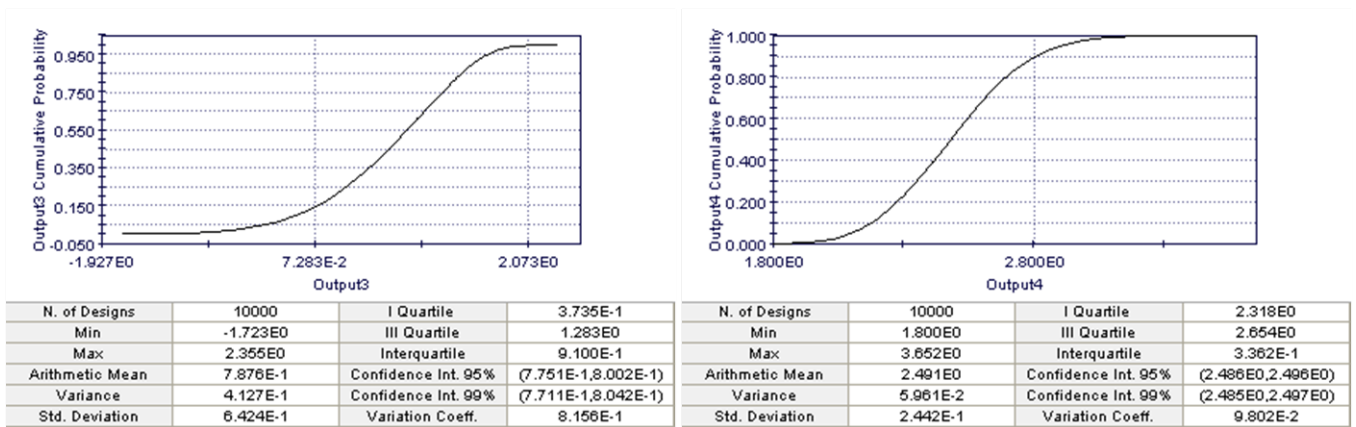


Figure 15.2: At the left in the figure is the pcf for the outlet swirl angle shown and at the right is the pcf over the deviation angle shown.

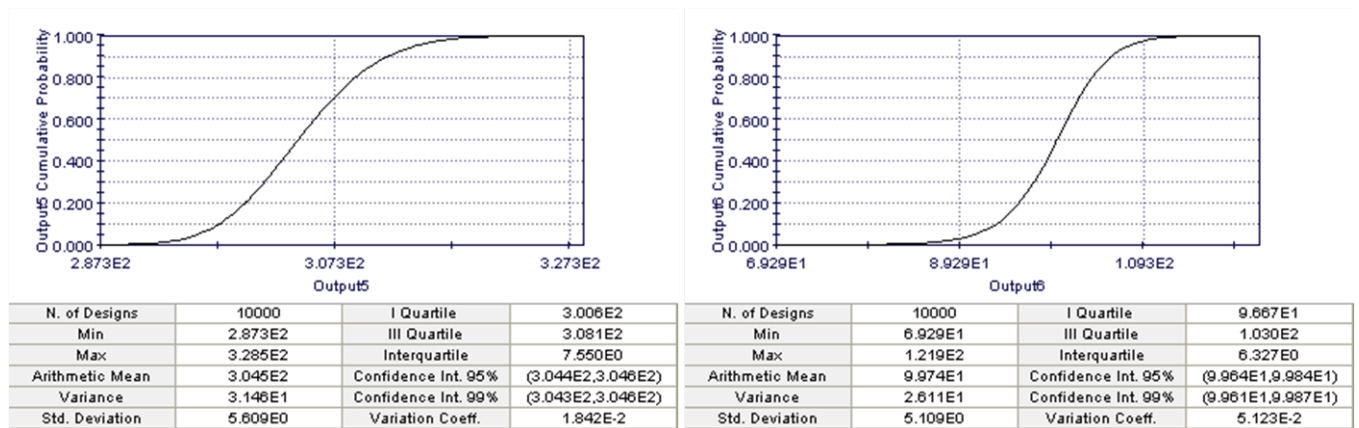


Figure 15.3: At the left in the figure is the pdf for the Vmax shown and at the right is the pdf over the Vmax axial position shown.

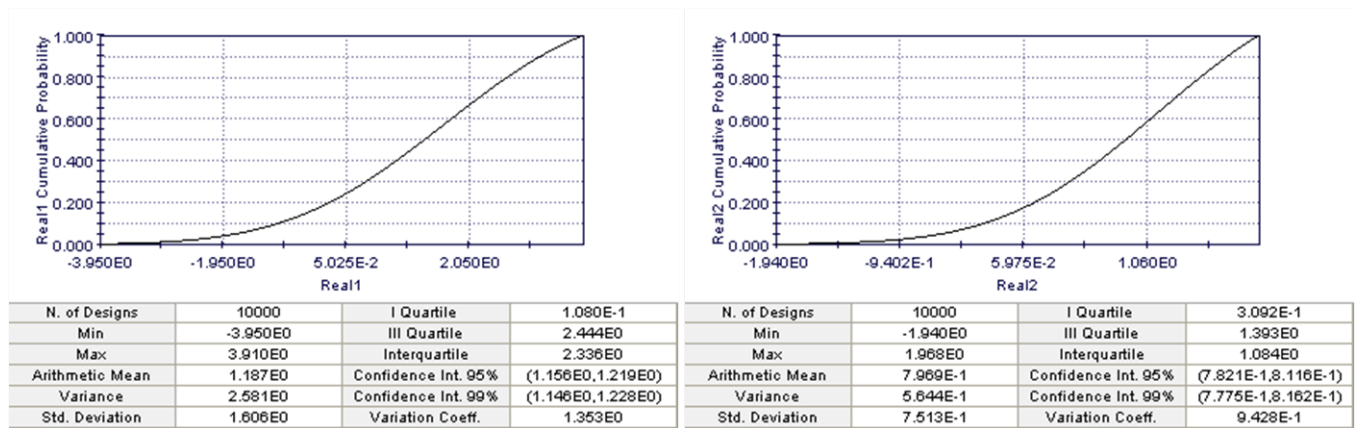


Figure 15.4: At the left in the figure is the pdf for the diffusion factor shown and at the right is the pdf over LE camber angle shown

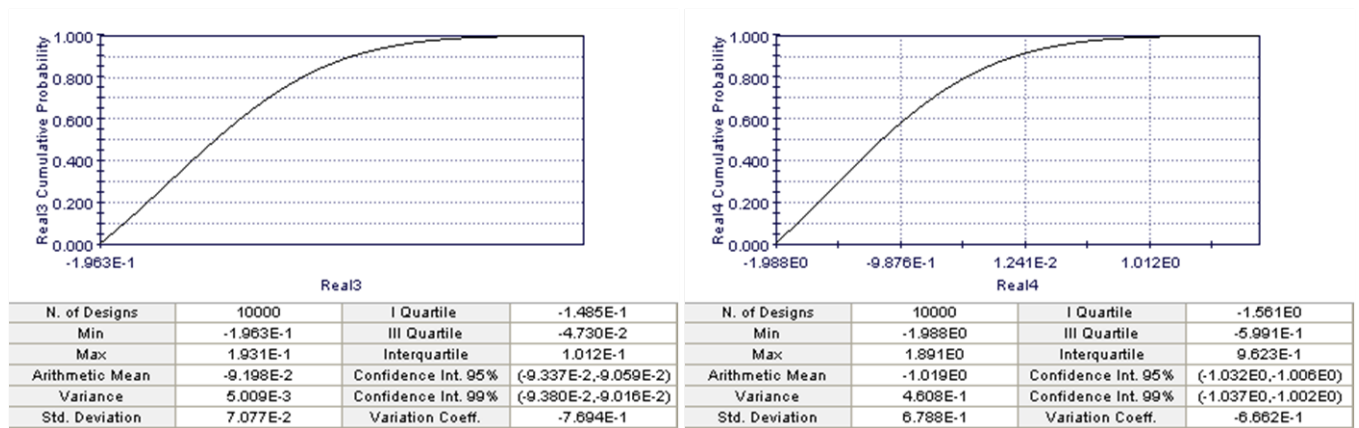


Figure 15.5: At the left in the figure is the pdf for the TE camber angle shown and at the right is the pdf over the derivative of the LE camber angle shown.

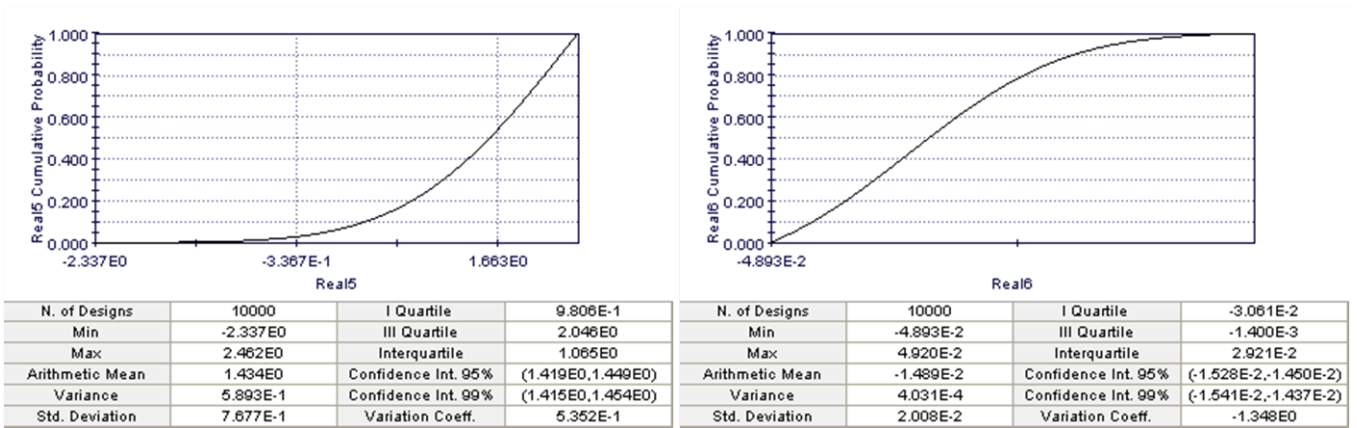


Figure 15.6: At the left in the figure is the pcf for the second derivative of the LE camber angle shown and at the right is the pcf over the max thickness shown.

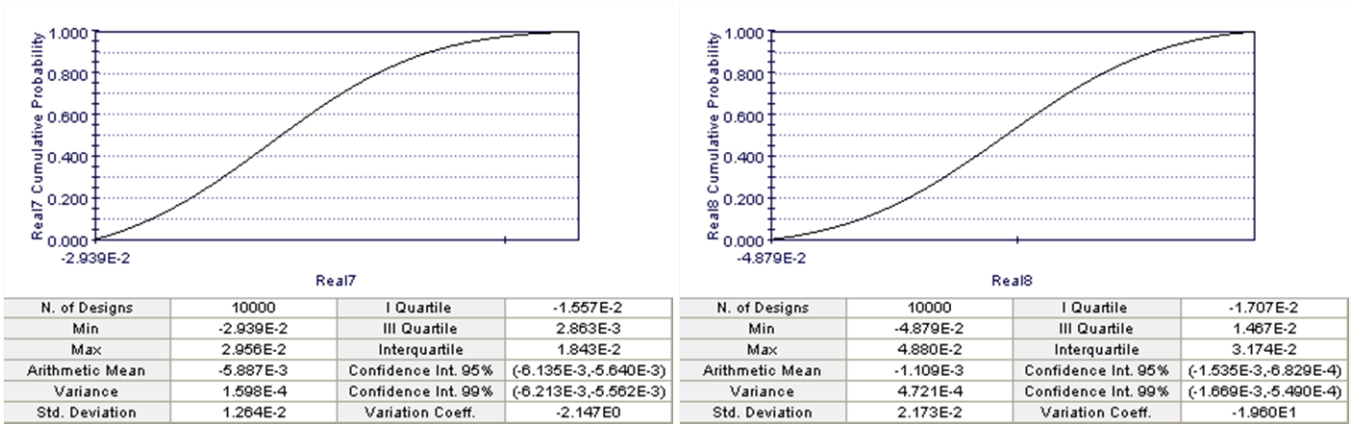


Figure 15.7: At the left in the figure is the pcf for the max thickness location (% of chord) shown and at the right is the pcf over the front thickness location shown.

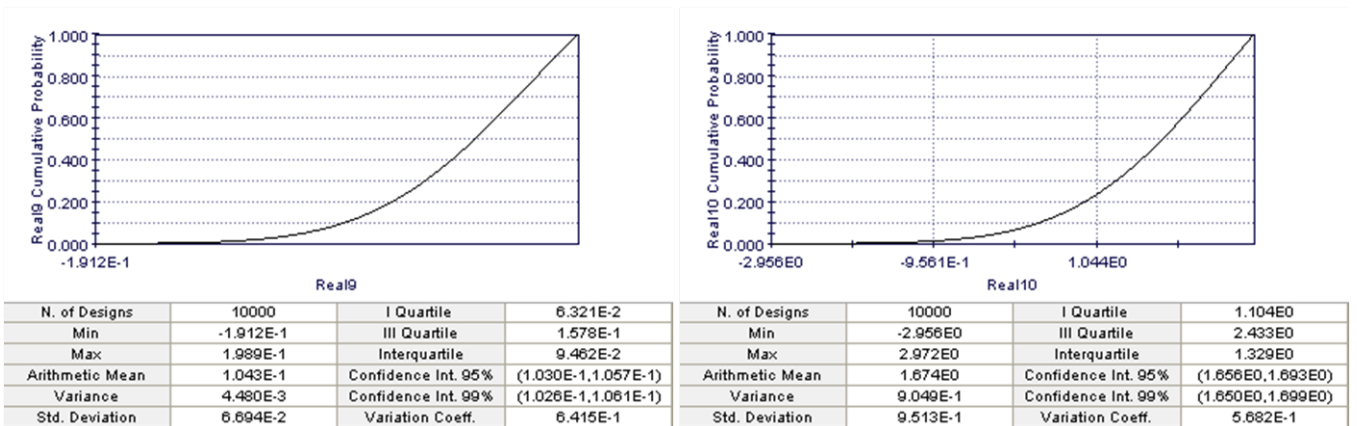


Figure 15.8: At the left is the pcf for the rear thickness modification shown and at the right is the pcf over the TE wedge angle modification shown.

16 Appendix E, CDF charts DoE-E

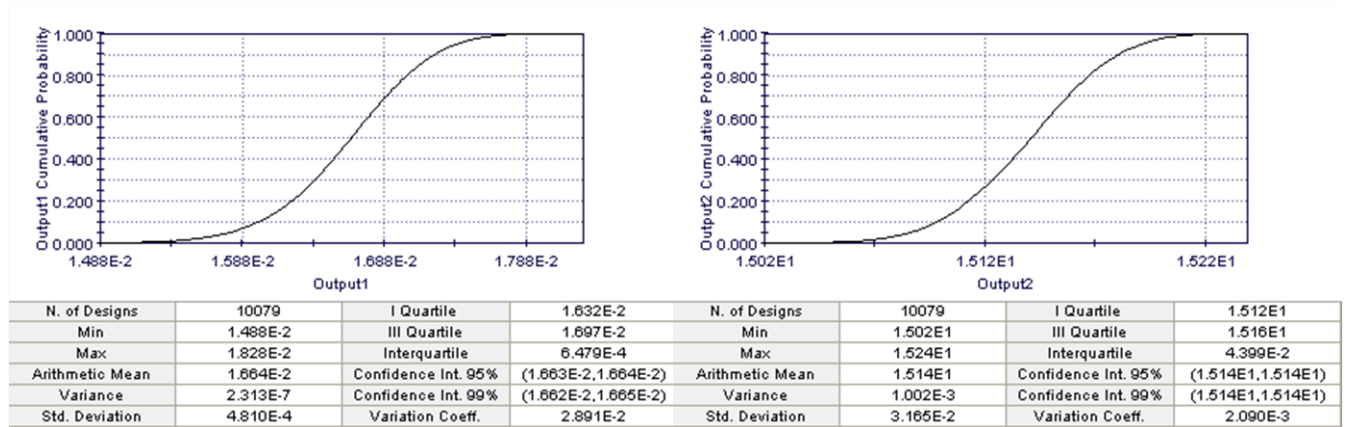


Figure 16.1: At the left side in figure the pcf for the loss estimation is shown and at the right is the pcf over the mass-flow shown.

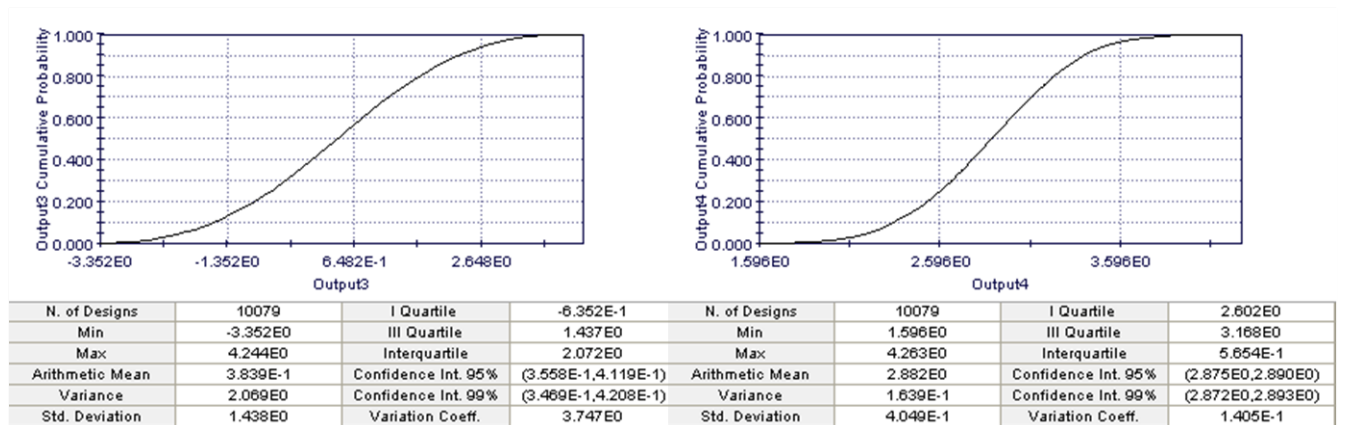


Figure 16.2: At the left in the figure is the pcf for the outlet swirl angle shown and at the right is the pcf over the deviation angle shown.

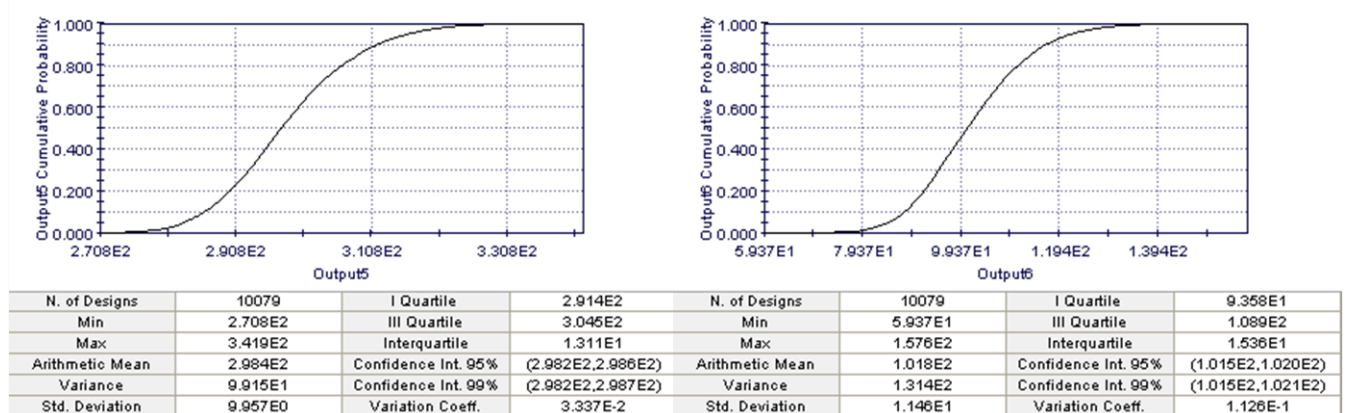


Figure 16.3: At the left in the figure is the pcf for the Vmax shown and at the right is the pcf over the Vmax axial position shown.

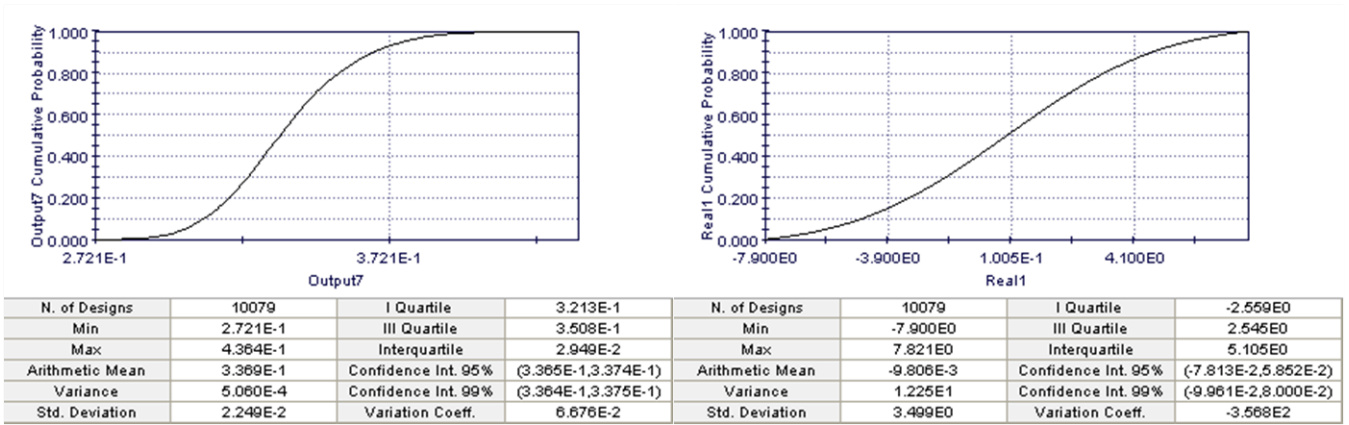


Figure 16.4: At the left in the figure is the pcf for the diffusion factor shown and at the right is the pcf over LE camber angle shown.

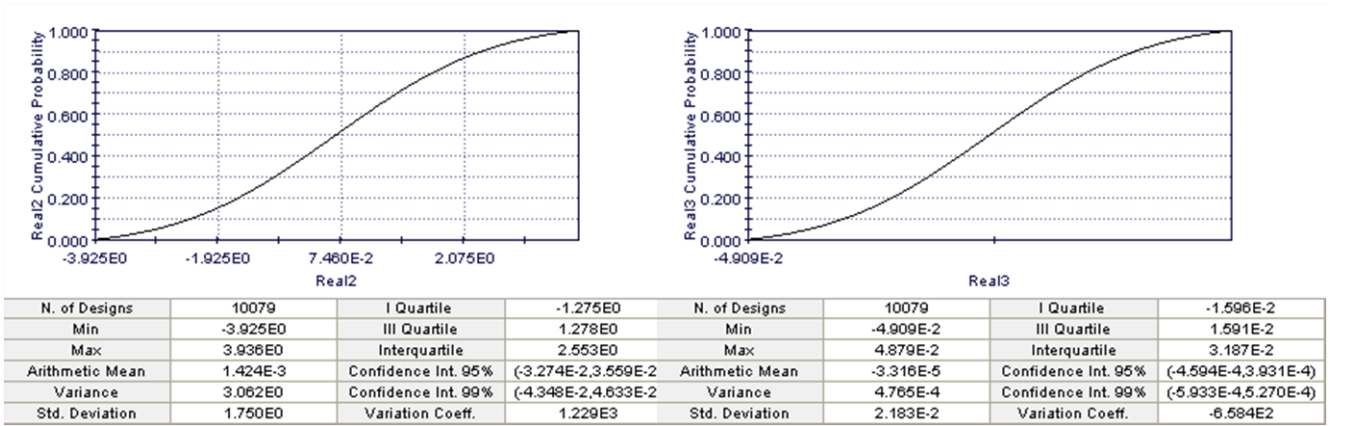


Figure 16.5: At the left in the figure is the pcf for the TE camber angle shown and at the right is the pcf over the derivative of the LE camber angle shown.

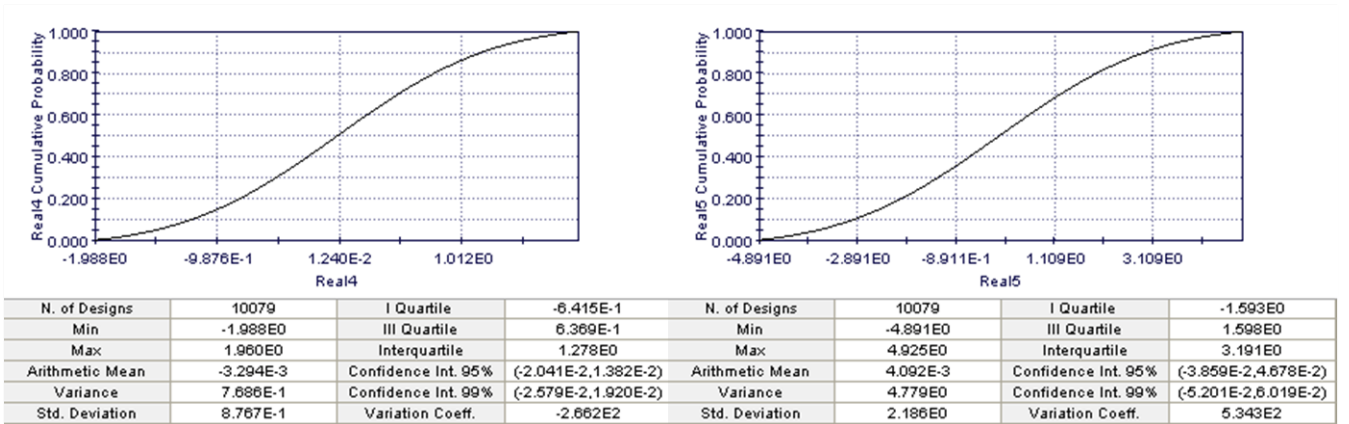


Figure 16.6: At the left in the figure is the pcf for the second derivative of the LE camber angle shown and at the right is the pcf over the max thickness shown.

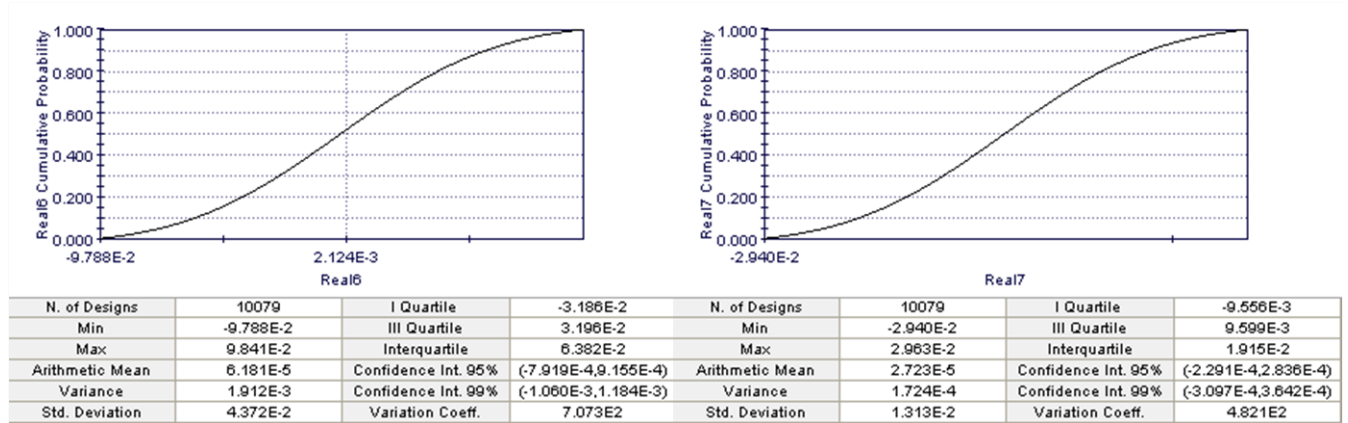


Figure 16.7: At the left in the figure is the pcf for the max thickness location (% of chord) shown and at the right is the pcf over the front thickness location shown.

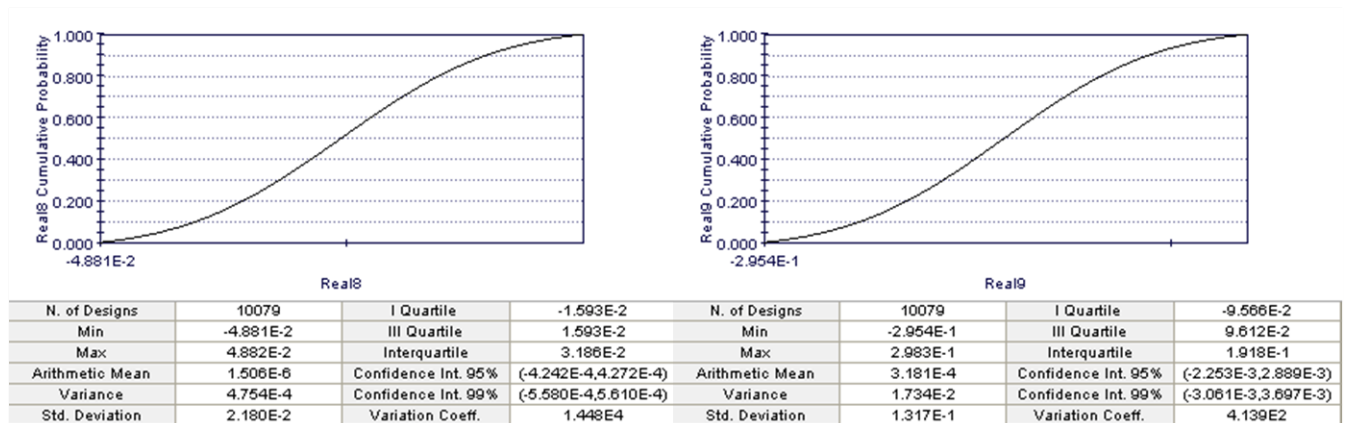


Figure 16.8: At the left is the pcf for the rear thickness modification shown and at the right is the pcf over the TE wedge angle modification shown.

References

- [Ans10] Ansys. In: (2010). URL: <http://www.ansys.com/Products/Simulation+Technology/Fluid+Dynamics/ANSYS+Fluent/>.
- [Bl] In: (2010). URL: <http://commons.wikimedia.org>.
- [Car03] E. H. P. Carpenter. "Aerodynamics for engineering students". In: *ISBN: 9780080493855* 5 (2003).
- [CFD10] CFD. In: (2010). URL: <http://www.cfd-online.com/>.
- [Cor10] V. A. Corporation. In: (2010). URL: http://www.volvoaero.com/volvoaero/global/en-gb/Pages/volvo_aero.aspx.
- [Dav03] L. Davidsson. "An introduction to turbulence models". In: *Chalmers University of Technology Sweden Publication 97/2* (2003).
- [Dav08a] L. Davidsson. "Numerical methods for turbulent flows". In: *Lecture notes at Chalmers University of Technology, Sweden* (2008).
- [Dav08b] L. Davidsson. "Turbulence modelling". In: *Lecture notes in MTF270 at Chalmers University of Technology, Sweden* (2008).
- [Eri10] L.-E. Eriksson. "Combustions in gas turbines". In: *Lecture notes in Applied mechanics/ Fluid dynamics at Chalmers University of Technology, Sweden* (2010).
- [Eri95] L.-E. Eriksson. "Development and Validation of Highly Modular Flow Solver Versions in G2DFLOW and G3DFLOW". In: *Internal report 9970-1162. Volvo Aero Corporation, Sweden*. (1995).
- [Geo08] W. K. George. "Lecture notes in Turbulence for the 21st century". In: *Chalmers University of Technology Sweden* (2008).
- [Ips10] R. B. N. Ipsen. "A Computational Approach to Include the Effects of Elevated Temperatures in Finite Element Simulations". In: *Master's thesis report at Volvo Aero Corporation, Sweden* (2010).
- [Lew96] I. R. Lewis. "Turbomachinery Performance Analysis". In: *ISBN: 9780080543321* (1996).
- [Ore06] S. Ore. "Optimization of a low-observable exhaust nozzle using response surface methodology". In: *Master's Thesis report at Volvo Aero Corporation, Sweden* (2006).
- [Rob10] T. Robertsson. "Compressor Transition Duct Aerodynamics". In: *Master's Thesis report at Volvo Aero Corporation, Sweden* (2010).
- [Rsm] In: (2010). URL: http://www.weibull.com/DOEWeb/rsm_designs.htm.
- [The] In: (2010). URL: http://thequalityportal.com/q_know02.html.
- [Tho09] F. J. L. Thomas. "Local and Global Deviations on Outlet Guide Vanes in Turbine Rear Frame". In: *Master's Thesis report at Volvo Aero Corporation, Sweden* (2009).
- [Vol] "Volvane, in-house programme". In: (2010).
- [Wal08] F. Wallin. "Flow Control and Shape Optimization of Intermediate Turbine Ducts for Turbofan Engines". In: *Department of Applied Mechanics* (2008).
- [Wei] In: (2010). URL: http://www.weibull.com/LifeDataWeb/the_probability_density_and_cumulative_distribution_functions.
- [Wik] In: (2010). URL: <http://schools-wikipedia.org>.
- [Wil93] D. C. Wilcox. "Turbulence Modeling for CFD". In: *ISBN: 0963605100* (1993).